Friction Surface Tailoring through Laser Micro-Texturing

A thesis submitted in fulfilment of the requirements

for the degree of Doctor of Philosophy

by

Gagandeep Singh Joshi

Department of Physics

(PhD Cycle XXXI)

University of Bari

January 2019

Funded by the European Union
Marie Sklodowska-Curie actions

Certificate

It is certified that the work contained in this thesis entitled "Friction Surface Tailoring through Laser Micro-Texturing" by "Gagandeep Singh Joshi" has been carried out under my supervision and that it has not been submitted elsewhere for a degree.

Thesis Supervisor

January 2019

Professor

Department of Physics

University of Bari

Supervisors

- Dr. Antonio Ancona
- Prof. Giuseppe Carbone

Coordinator

- Prof. Giuseppe Iaselli

External Reviewers

- Dr. Suwas Nikumb, Senior Research Officer and Scientific Advisor, Specialty Coatings and Microfabrication, National Research Council Canada.
- Prof. Daniele Dini, Head of the Tribology Group, Imperial college London, UK.

Abstract

Over the past decades, surface texturing has shown to be an emerging technique to control the friction and wear. It consists of fabricating a pattern of small dimples or grooves on the surface of the materials in a very controllable way, which causes the change in the surface topography. Lasers with their excellent beam quality promised noticeable advantages and improvements in high precision and material processing at the microscale. In order to control the friction, it is important to understand the mechanisms which occur during the conformal or non-conformal contact in dry and lubricated conditions.

In the present thesis, I am dealing with laser surface texturing to improve the tribological properties of the technological steels. I have fabricated the pad based on a design developed previously to my thesis, it consists of an anisotropic and non-uniform texture to maximize the thrust load of a square pad prototype. The experimental results, showed that the non-uniform micro-texture largely affects the friction characteristics of the contact. In particular, in agreement with the BTH predictions, the tribo-system shows friction properties that are strongly sensitive to the direction of the sliding speed, as a consequence of the micro-fluid dynamics which are designed to occur only in a specific sliding direction. Results suggest that the joint action of virtual prototyping (BTH lubrication theory) and ultrafast laser micro-prototyping can lead to unconventional and impressive results in terms of enhanced or tailored contact mechanics properties of the generic lubricated tribopair.

I have also investigated the effects of the micro surface texturing in the lubricated non-conformal point contacts. In this investigation, I have focused on a regime poorly investigated in literature, where the contact area and the micro-holes have

a comparable size. In particular, I found that, depending on the void ratio, a significant friction reduction or, on the contrary, a deterioration of the frictional performances can affect the boundary and mixed lubrication regimes. This was due to the simultaneous occurrence of two competing effects. One was related to the stress intensification, due to the presence of the micro-hole edges on the contact topography, which leads to a consequent increase in wear and friction. On the other hand, micro-texture may play a positive role in the friction optimization given the possibility, offered by the micro-holes, to entrap wear debris and, then, to preserve a smoother interface between the contacting pairs.

Investigation of the wettability and spreading behavior of the lubricant on laser textured surfaces helps to understand more about its tribological performance. The tribological behavior of different textured surfaces have been studied using mineral oil as lubricant. Results show that textured surfaces have friction reduction under different lubrication regimes as compared to un-textured surfaces. Furthermore, static contact angle and spreading were evaluated with water, mineral oil and pure glycerol. Every considered texture showed a slight reduction of contact angle for the three liquids, compared with the polished surface. Mineral oil exhibited a more persistent spreading over the un-textured and textured surfaces, and more consistency in friction reduction. Mineral oil shows compatibility for low and high dynamic velocities in the case of textured and un-textured samples, whereas, glycerol is beneficial at specific velocities.

Acknowledgements

I would like to begin by thanking my Ph.D. supervisors, there insistence on expressing problems in the most simplistic terms and enthusiastic scientific attitude, helped me to guide towards the core and fundamental issues of Laser Micromachining and Tribology. Inspite of their heavy responsibilities of teaching and experimental research work, they really spared time for academic interaction with me. I could not have completed my doctoral studies without the support of a great number of amazing mentors, family, friends and relatives to which I dedicate my thesis.

I would like to thank Prof. Giuseppe Carbone, Dr. Antonio Ancona, Dr. Caterina Gaudiuso, Dr. Carmine Putignano for all the fruitful discussions that took place over the past years, which helped me to have an in-depth understanding of the various issue, which could be beneficial for future projects. I would like to thank my supervisors for believing in me and giving me the opportunity to carry out this research, which I most certainly could not have done alone. It has been a long and hard road and in the end, we ended up with something exciting.

My sincere thanks are due to Dr. Thomas Kiedrowski (Senior Tribology Expert) and Tobias Stark for the assistance during the experiments and Sarona Frank for the technical support at the Corporate Research and Development Department of the Robert Bosch GmbH in Renningen (Stuttgart), Germany. My specials thanks go to Prof. Dimov, Prof. Dong, Jean Michel Romano , Antonio Garcia-Giron and Benham Dashtbozorog for the assistance during experiments at the Department of Mechanical Engineering and Department of Metallurgy and Materials at University of Birmingham.

I am sincerely thankful to Prof. Giuseppe Iaselli (Coordinator-PhD School), and Prof. Gaetano Scamarcio (Director of CNR-IFN, Bari). I thank Angela Loiudice for her cooperation and always being available. I also wish to thank to Cinzia Balsamo and all members of administrative staff of CNR-IFN and Physics department.

A massive shout-out goes to all my friends in and out of the Laser4Fun group that have truly made my experience over the years great. I will never forget all the fun and drama we've had and I almost wish I could do it all again. A special mention goes out to my dear Narinder and Juls, who has been there for me through the highs and lows of my doctoral years. I wouldn't have been able to do it without you. Finally, I thank to all of my fellow students, postdocs and all colleagues from Bari and Laser4Fun for all of their support through the years.

I owe the great gratitude to my parents for giving me life and guiding me to where I am today. I thank them and my sisters for their unconditional love and support. Finally, yet importantly I am grateful to the supreme power, The God, who has bestowed upon me the blessings of hard work, dedication and commitment to reach the present position.

I thank to the European Commission for providing the financial support for carrying this research activity within the project "Laser4Fun", which is funded under the European Union's Horizon 2020 research and innovation programme under the Marie Sklodowska-Curie grant agreement No. 675063.

Gagandeep Singh Joshi

LIST OF PUBLICATIONS

JOURNAL PUBLICATIONS

- Non-Uniform Laser Surface Texturing of an Un-Tapered Square Pad for Tribological Applications, Antonio Ancona, G. S. Joshi, Annalisa Volpe, Michele Scaraggi, Pietro Mario Lugara and Giuseppe Carbone, Lubricants 2017, 5, 41; doi:10.3390/lubricants5040041.

- Effects of the micro surface texturing in lubricated non-conformal point contacts, G.S. Joshi, C. Putignano, C. Gaudiuso, T. Stark, T. Kiedrowski, A. Ancona, G. Carbone, Tribology International 2018, 127, 296-301.

CONFERENCE PROCEEDINGS

- Experimental Investigation of the Tribological and wettability Properties of the Laser-Textured Martensitic Steel Surfaces G.S. Joshi, B. Dashtbozorg, J.-M. Romano, A. Garcia-Giron, H. Dong, S.S. Dimov, A. Ancona, G. Carbone@19th International Symposium on Laser Precision Microfabrication, Edinburgh, United Kingom, 25-28 June 2018,

- Modifying steel surface tribology by ultrafast laser micro-texturing, by A.Ancona, G.S. Joshi, C. Gaudiuso, C. Putignano, M. Scaraggi, P.M. Lugara, G. Carbone @19th International Symposium on Laser Precision Microfabrication, Edinburgh, United Kingom, 25-28 June 2018,

- Friction behaviour of the micro-textured surfaces in lubricated non-conformal contacts, by G.S. Joshi, C. Putignano, C. Gaudiuso, A. Ancona, G. Carbone @ AIMETA 2017 XX111, Salerno, Italy, 4-7 September 2017, http://www.aimeta2017.unisa.it/node/53

- Tribological effects due to different geometries of surface texturing on lubricated non- conformal contacts, by G.S. Joshi, C. Gaudiuso, C. Putignano, A. Ancona, G. Carbone @ 6th European Tribology Conference ECOTRIB 2017, Ljubljana, Slovenia, 7-9 June 2017.

Contents

Certificate ii

Abstract iv

Acknowledgements vi

Contents ix

List of Figures xv

List of Tables xix

Abbreviations xxi

Symbols xxiii

1 Introduction 1

2 LASER MICROMACHINING 5

2.1 Laser Material Processing 8

2.1.1 Light Matter Interaction (fs-ps & ns pulses) 8

2.1.2 Laser Surface Texturing 10

2.2 Mechanism of laser ablation of metals 11

2.2.1 Processing technologies 16

2.3 Optimization: Surface texturing parameters 17

2.3.1 Analytical Studies: 17

2.3.2 Experimental Studies: 20

2.4 Summary 22

3 TRIBOLOGY 23

3.1 Friction . . . 25
3.1.1 Static & Kinetic Frictions: . . . 27
3.2 TOMLINSON's Theory of Molecular attraction, 1929: . . . 30
3.2.1 Scientific Explanation of Dry Friction: . . . 31
3.3 Wear . . . 33
3.3.1 Wear Mechanisms: . . . 35
3.4 Lubrication . . . 38
3.4.1 Lubrication mechanisms: . . . 40
3.4.2 Stribeck Curve: . . . 41
3.5 Fluid Film Lubrication: . . . 43
3.6 Derivation of Reynold's equation . . . 49
3.6.1 Effect of Cavitation on Friction during lubricated contact . . . 52

4 MATERIALS AND EQUIPMENT 55
4.1 Introduction . . . 55
4.2 Materials- Stainless steel . . . 55
4.2.1 Used Materials . . . 57
4.2.2 Sample Preparation . . . 60
4.3 Equipment . . . 61
4.3.1 Laser Equipment . . . 61
4.3.1.1 Femtosecond laser: Active Fiber System Ultrafast laser 61
4.3.1.2 Femtosecond laser: Set-up for pulse selection . . . 62
4.4 Surface Characterization Equipment . . . 64
4.4.1 Scanning Electron Microscope . . . 64
4.4.2 Optical Microscope . . . 64
4.4.3 Microscopy technique (confocal): . . . 67
4.4.3.1 CSM- Confocal Microscope . . . 68
4.4.3.2 Olympus LEXT OLS 4000 Confocal Laser Microscope: 70
4.5 Tribometry or Tribological Equipment . . . 71
4.5.1 High Temperature Tribometer - CSM Instruments . . . 71
4.5.2 Rheometer . . . 72
4.5.3 TE79 Tribometer: . . . 75
4.6 Pressure measurement system: Pressure Distribution Mapping System FPD-8010E . . . 76
4.7 Contact Angle Measurement System . . . 76
4.7.1 Attension theta optical tensiometer . . . 77

5 Results and Discussion 79
5.1 Non-Uniform Laser Surface Texturing of an Un-Tapered Square Pad for Tribological Applications . . . 79
5.1.1 Fabrication of Samples . . . 81
5.1.2 Morphological Characterization . . . 84

5.1.3 Tribological Characterization 85
5.1.4 Results and Discussion 87
5.1.5 Conclusions 90
5.2 Effects of the micro surface texturing in lubricated non-conformal point contacts 92
5.2.0.1 Surface texture manufacturing by Femtosecond laser ablation process (fsLA) 93
5.2.0.2 Characterization 94
5.2.0.3 Results and Discussion 96
5.2.0.4 Conclusions 100
5.3 Experimental investigation of the tribological and wettability properties of laser-textured martensitic steel surfaces 100
5.3.1 Characterization 102
5.3.1.1 Contact Angle Measurement 102
5.3.2 Results and discussion 103
5.4 Conclusions 108

6 Conclusion **111**

Bibliography **113**

List of Figures

2.1 Piston Texture [1] . . . 6
2.2 Partial surface texturing of a stator (a) in contact with plain rotor (b) [2] . . . 7
2.3 Examples of material removing using a laser . . . 14
2.4 Example process for an ultrashort laser pulse . . . 15
2.5 Modalities for the LST: a) Single pulse drilling; b) Percussion drilling; c) Trepanning . . . 17
2.6 Circumferential gas seal Schematic [3]. . . . 19
2.7 Textured squares and grooves by Pettersson and Jacobson [4] . . . 21

3.1 The first recorded tribologist, pouring lubricant (probably water) in front of the sledge in the transport of a statue in Egypt (2400 B.C.) . . . 24
3.2 Coefficient of friction for various metals [5, 6] . . . 26
3.3 Adhesive Friction among various materials [7, 6] . . . 27
3.4 Difference between the static and kinetic friction may initiate 'stick-slip'[8] . . . 28
3.5 Amonton's work[9] . . . 28
3.6 Coulomb friction model [7, 6] . . . 30
3.7 Adhesion [10] . . . 30
3.8 Abrasion(Deformation) [67] . . . 31
3.9 Zero wear of helical gear[5] . . . 33
3.10 Measurable wear of helical gear [5] . . . 34
3.11 Formation of pit . . . 35
3.12 Schematic representation of the major wear modes: a) adhesive; b) abrasive; c) fatigue; d) corrosive [11]. . . . 35
3.13 Abrasive wear of gear [12] . . . 37
3.14 Newtonian and non-Newtonian fluid . . . 39
3.15 Fluid film lubrication . . . 39
3.16 Comparison between average and root mean square roughness [12, 13] 41
3.17 Foreign particles/wear debris shift hydrodynamic/elastohydrodynamic lubrication in boundary/mixed lubrication [13] . . . 41
3.18 Stribeck curve and lubrication regions [14, 15] . . . 42
3.19 Various concepts to separate two solid surfaces [15] . . . 45

3.20 Converging wedge shape geometry . . . 45
3.21 Squeeze lubrication . . . 45
3.22 Hydrodynamic lubrication . . . 46
3.23 Shearing of lubricant . . . 46
3.24 Boundary lubrication . . . 47
3.25 Mixed lubrication . . . 47
3.26 Fluid film lubrication between two plates [82,83,61] . . . 48
3.27 Lubrication . . . 48
3.28 Fluid element subjected to pressure & viscous forces [14] . . . 49
3.29 Development of fluid pressure in relatively moving inclined plates [14] 50
3.30 Velocities of plates . . . 51
3.31 Inclined plates with fluid element and coordinate system [15] . . . 52

4.1 Schematic of the evolution of stainless steels starting from plain carbon steels: the stainless-steel tree structure [16, 17] . . . 57
4.2 Characteristics of the 100 Cr6 steel balls used [18] . . . 58
4.3 Characteristics of the stainless steel (1.4112)[18] . . . 59
4.4 Sample Preparation . . . 60
4.5 Sketch of the Active Fiber System GmbH [19] . . . 61
4.6 Experimental set-up for the selection of a precise number of pulses. Two pulse duration were used: 650fs and 10ps. The laser wavelength is 1030nm [20] . . . 63
4.7 Schematic diagram of SEM setup [21] . . . 65
4.8 Optical Microscopes- Nikon Eclipse ME6000, Leica DM4000M(www.bosch.com) 66
4.9 Schematic diagram of Microscopic setup [22, 23] . . . 67
4.10 CSM Platform (Open Platform) [www.csm.com] . . . 68
4.11 Chromatic coding principle[www.csm.com] . . . 69
4.12 Image acquisition principles of the ConScan objective[www.csm.com] 69
4.13 Features of the Confocal 3D Microscope [24] . . . 70
4.14 CSM High Temperature Tribometer[csm.com] . . . 71
4.15 Schematic representation of the ball on three-plates-device in side and top view. The torque and the normal force applied by the rheometer are indicated by arrows . . . 73
4.16 Schematic representation of the ball in contact with the textured surface 74
4.17 FTE79 Tribometer . . . 74
4.18 FPD-8010 E [Fujifilm.com] . . . 77
4.19 Theta Optical Tensiometer [google image] . . . 78

5.1 Schematic representation of an optimized micro-grooved partial textured squared pad. The red circles indicate the untextured areas, while the red strips show the local angular alignment of the grooves. The gray scale indicates the dimple depths, where hh is the dimple depth and hf is the nominal separation between the two sliding surfaces. Adapted from [25] with the permission of the author 81
5.2 Schematic representation of the truncated bearing. The grey area was removed by laser milling up to 100-μm-depth 82
5.3 (a) Schematic of the texture pattern; (b) dimple size; (c) ablation strategy to realize each dimple 83
5.4 Optical microscope images of the overall textured area, and high magnification SEM images of some micro-grooved dimples of sample with rectangular (a,b) and elliptical (c,d) shape texture pattern 84
5.5 Confocal profiles along the major axis of an ablated rectangular dimple after (a) 9 loops; (b) 14 loops; and (c) 19 loops 85
5.6 Comparison between the Stribeck curves measured for the two textured pads with rectangular (sample L) and elliptical (sample E) micro-grooved dimples, respectively. The temperature was set at $20 \pm 2\,\mathrm{deg}\,C$ and a normal load of 1 N was applied during the measurements 88
5.7 The mean coefficient of friction as a function of for the textured sample at three different normal load values as a function of the sliding speed. The temperature was set at $20 \pm 2\,\mathrm{deg}\,C$ 89
5.8 Friction coefficient behavior calculated as the tangential force T to the normal force N ratio, measured in the case of the untextured sample. The tribometer operates in the reciprocating mode with isothermal conditions of the oil bath ($24 \pm 2\,\mathrm{deg}\,C$), linear translation speed of 136 mm/s reversed with a frequency of 1 Hz, and a normal load of 0.25 N 90
5.9 Friction coefficient behavior calculated as the tangential force T to the normal force N ratio, measured in the case of the textured sample. The tribometer operates in the reciprocating mode with isothermal conditions of the oil bath ($24 \pm 2\,\mathrm{deg}\,C$), linear translation speed of 136 mm/s reversed with a frequency of 1 Hz, and a normal load of 0.25 N 91
5.10 LST samples with different texture geometries (Triangular geometry: dimples with diameters d=183 μm, depth h6.7 μm, areal density A [%] =0.29; Hexagonal geometry: dimples d=183 μm, h6.6m, A [%] =0.27; Rectangular geometry: dimples: major axis L=200 μm, minor axis W=100 μm depth h7.3 μm, areal density A [%] =0.53, compared to the stainless steel polished surface. 93
5.11 Contact pressure distribution maps (FPD-8010E) based on the analysis of the acquired microscope images of the Fujifilm measurement foils shown in the insets 98

5.12 Industrial Laser Confocal Microscope 3D Images (50X) for the rectangular geometry texture (on the top) and CSM Confocal Microscope Images for the hexagonal texturing (on the bottom). In both cases, the worn zone is clear 99
5.13 Friction coefficient, μ, vs. sliding velocity, u. Figure 5.13(a) and 5.13(b) refer respectively to the low viscosity (Type 1) and the high viscosity lubricant (Type 3). For each measure, we report the scatter as an errorbar. 101
5.14 Image of Phoenix TE79 tribometer 103
5.15 Friction coefficient vs Hersey number under dry and lubricated conditions on lubricated un-textured polished steel 104
5.16 Friction coefficient vs Hersey number for un-textured and different textured surfaces, using mineral oil as a lubricant 105
5.17 Image and measurement of static contact angles of the polished (P), triangular (T), hexagonal (H), and rectangular (R) textured surfaces, using comparatively water, glycerol and mineral oil as probe liquid . . 106
5.18 Oxygen content measured by EDS (wt%) on untextured surfaces and inside/outside the different laser-textured dimples 107
5.19 Spreading of lubricants on rectangular textured surface ($6\mu l$, 20deg C) with respect to the contact angle and area 108
5.20 Evolution of spreading of lubricants (glycerol and mineral oil) on rectangular textured surface with the increase of temperature 109

List of Tables

3.1 Coefficient of friction for various metals sliding on themselves [6] . . . 26

5.1 Number of loops for each dimple depth and shape. 83
5.2 Process parameters defined for each texture geometry[circular dimples textured in hexagonal and triangular lattice, quasi rectangles textured in rectangular lattice] 94
5.3 Viscometric Characteristics 96
5.4 Viscometric characteristics for the considered fluids. 103

Abbreviations

LST	**L**aser **S**urface **T**exturing
HD	**H**ydrodynamic
B	**B**oundary
M	**M**ixed
PAO	**P**oly **A**lpha **O**lefin
CA	**C**ontact **A**ngle
PG	**P**olished **G**eometry
TG	**T**riangular **G**eometry
HG	**H**exagonal **G**eometry
RG	**R**ectangular **G**eometry

Symbols

I_A	Absorbed Intensity
I_0	Incident Intensity
$\|\beta\|$	Attenuation Coefficient
$\|\alpha\|$	Thermal Diffusivity
k	Thermal Conductivity
ρ	Density
C_p	Specific Heat
$\|\alpha\|$	Thermal Diffusivity
τ_i	Pulse Duration
$\|\alpha\|$	Thermal Diffusivity
D	Thermal Penetration Depth
F^{th}	Threshold Fluence
μ	Coefficient of Friction
F_f	Friction Force
N	Applied Load
E	Young Modulus
F_a	Adhesion Force
F_d	Deformation
A_R	Contact Area
$\|\tau\|$	Shear Modulus
H	Hardness of Soft Material
η	Dynamic Viscosity

Λ	Specific Film Thickness
%	Void Ratio
$R_{rms,a}$	root mean square (rms) surface roughness of surface a
$R_{rms,b}$	root mean square (rms) surface roughness of surface b

Dedicated to My Loving Family

Chapter 1

Introduction

Friction has a key role in several applications in our daily lives. In some applications, high friction is desirable, as in tires, brakes, clutches, and frictional power transmission systems. In other applications, the friction is required to be minimized, in order to improve energy efficiency, component durability, and overall system reliability. In all the above-mentioned cases, understanding the complex mechanisms involved in friction, and the means to control/regulate it, is necessary. Various approaches have been classically employed in order to control friction, some of which are the adoption of a lubrication technique, or the surface functionalization (e.g., through coating) of the tribo-pair.

Surface texturing has shown significant promise over the past decade as one of the surface engineering methods to modify friction performance. There are different techniques to texture the surface but Laser Surface texturing (LST) is probably the most advanced so far. In particular, LST provides an excellent control of the micro-structures by simply controlling the laser parameters, together with the short processing times due to the availability of high speed scanning systems and high frequency lasers. Topography of the surfaces plays important role in influencing the tribological properties of the materials and, in particular, the friction behavior of the two-rubbing surfaces during conformal and non-conformal contacts. It has long been known that micrometer-scale surface irregularities affect the load capacity of

parallel sliding surfaces [26], however only recently have such textures been engineered to improve friction performance of mechanical parts [27, 28]. The coefficient of friction can be controlled but it depends upon the microgeometry of the textured surface.

In this research work, I have focused on laser micro surface texturing of technological steels, with an objective to design and fabricate the geometrical patterns for improving the tribological properties of the mechanical components for e.g. life time, friction reduction, etc. Uniform and Non-uniform geometrical patterns are fabricated by using Ultra-Short Pulsed Direct Laser Writing, and later characterized for conformal and non-conformal contacts under dry and lubricated conditions. In chapter I, I have presented the details about the light- matter interaction with different laser sources, and it also explains the mechanism behind the laser ablation of metals. Further, analytical and experimental studies allowed to optimize the laser surface texturing parameters. In chapter II, I have investigated the tribological methods to improve service life, safety and reliability of interacting machine components. The advent of new techniques to measure topography, adhesion, friction, wear, lubricant film thickness, and mechanical properties, all micro- to nanometer scales, lead to the development of the respective sub-fields of the tribology, separated by different approaches and laws that govern and explain the interfacial phenomena.

In chapter III, I have introduced the materials that were investigated, the laser equipment and surface analysis instruments used. The femtosecond laser machining is described in terms of its setup and operational parameters. The modes of operation of the laser and of obtaining the laser pulses are described. Description of the setups and procedures used to carry out the various fabrications and characterization studies is presented in this chapter. In chapter IV, the tribological results from the textured surfaces due to different geometrical patterns were investigated. In this context, I have investigated different geometrical patterns for conformal and non-conformal contacts. Different experimental techniques were used to study the tribological effects on the laser textured surfaces on technological steel. In particular, the Bruggeman Texture Hydrodynamics theory (BTH) was employed for the design of the anisotropic and non-uniform texture maximizing the thrust load of

the pad prototype or micro surface texturing in the lubricated non-conformal point contacts by designing different geometrical patterns.

Chapter 2

LASER MICROMACHINING

Over the recent years, the laser technology and its potential have been exciting laser manufacturers as well as researchers and industrial users. Lasers with their excellent beam quality promised noticeable advantages and improvements in high precision and material processing at the microscale. The world of laser machining production is divided into micro- and macro- machining. This classification is not based on the size of the work piece but rather the fineness of the impact caused by the laser tool. The lasers system used for micromachining employ normally pulsed beams with an average power below $1kW$, while those used for macro machining use generally continuous-wave (CW) laser beams ranging up to several kW. The field of micro-machining includes manufacturing methods like drilling, cutting, welding as well as ablation and material surface texturing, whereby it is possible to achieve very fine surface structures ranging in the micrometer domain. Surface texturing has shown significant promise over the past decades as one of the surface engineering methods to modify tribological behavior or friction performance.

Various machining methods have been employed to create micro-texturing on the surface of different materials. In 1966, Hamilton *et al.* [26] proposed the idea of having micro asperities acting as hydrodynamic bearings in parallel sliding applications such as rotary shaft face seals. Anno et al. [29] verified that higher load carrying capacities were achieved when only one of the parallel surfaces of the rotary shaft face seals had micro-asperities in the form of cylinders. Willis [30] used surface texturing

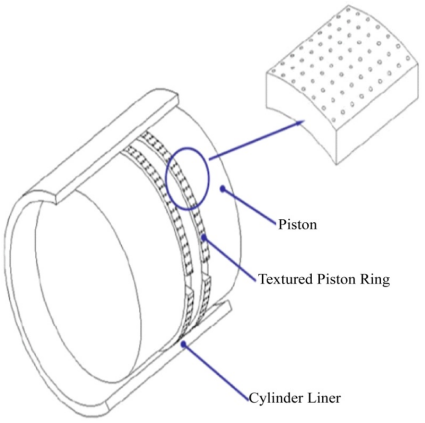

FIGURE 2.1: Piston Texture [1]

in cylinder bores of a combustion engine. Schneider [31] developed the vibro-rolling method to create shallow channels using a hard indenter that vibrates as it translates across the workpiece. Suh et al.[32] used chemical etching and abrasive machining to create modulated or undulated patterns that act as traps for oxide wear debris, and Willis [30] used honing to generate micro-grooves for the cylinder bores of internal combustion engines. The micro-grooves improve the lubrication between the cylinder walls and the piston ring. Reactive ion etching (RIE) was used by Wang et al.[33, 34, 35] to explore the influence of micro dimples on the silicon carbide surface sliding in water. Large circular dimples and small square depressions were fabricated using Reactive Ion Etching, where high energy chemical plasma was directed at the part causing surface material removal. Peterson and Jacobson [36] used a standard photolithographic technique, with Potassium Hydroxide as anisotropic etchant, to create runners and square depressions of $5\mu m$ in depth on silicon wafers. Wukada et. al. [37] employed abrasive jet machining (AJM), where the surface was bombarded with high velocity fine abrasive particles that cause the physical removal of material. Excimer laser beam machining (LBM) was also used by the same group. These two fabrication methods result in different profile shapes, circular and angular from AJM and LBM respectively, though the effect of the texture shape is found to be insignificant. The vibro-mechanical texturing (VMT) technique was developed by Greco et al. [38], and this technique is based on the conventional turning operation with a fast tool servo that is used to oscillate the cutting tool. This oscillating motion creates holes when the cutting tool contacts the work piece.

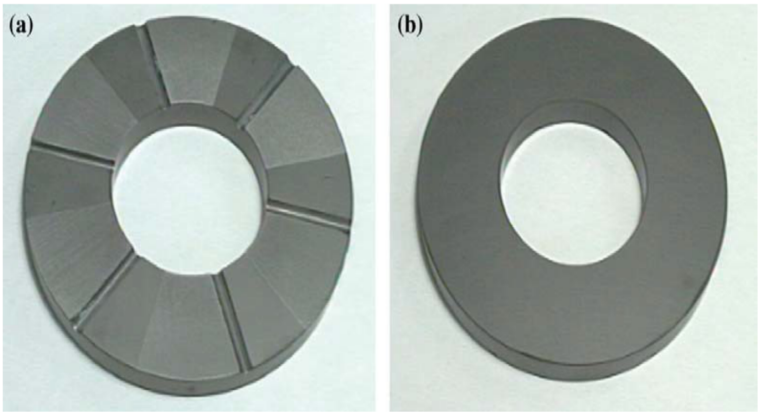

FIGURE 2.2: Partial surface texturing of a stator (a) in contact with plain rotor (b) [2]

Etsion *et al.*[2, 27, 28, 39, 40] and Yu *et al.* [41] used laser surface texturing on mechanical face seal rings. The results showed significant reduction in frictional losses. The effect of the surface texturing on the friction losses by the cylinder liner-piston ring system, which was estimated at 30% of the total engine friction [1], was addressed in [42, 43, 44, 45]. Baumgart *et. al.*[46] used a laser surface texturing technique to create discrete round dome-like protrusions on the inner diameter of the hard disk to reduce the stiction at the start up. Laser surface texturing (LST) has been widely used for over 20 years in different applications [47]. Laser surface texturing has many advantages over the previously mentioned texturing fabrication methods since it is very fast, environmentally clean, precise, and maskless. In addition, a variety of sizes can be created, and it can be used with most material types. Surface structural modification can be achieved through the application of different techniques, including vibro-rolling, reactive ion etching, and laser surface texturing. However, the laser surface texturing seems to offer most promising concepts so far. This chapter reviews about the light-matter interaction with different laser sources, and it also explains the mechanism behind the laser ablation of metals. Further, analytical and experimental studies allowed to optimize the laser surface texturing parameters.

2.1 Laser Material Processing

2.1.1 Light Matter Interaction (fs-ps & ns pulses)

When the laser radiation is incident on a material most of the photons get absorbed by the electrons present in the outermost shell of the atoms in the upper layers of the material (called the skin layer). The thickness of the skin layer, also called the optical penetration depth (δ), is $2/\alpha$, where α is the absorption coefficient of the material for the particular wavelength. Higher absorption coefficient implies smaller skin depth, which means that the incident radiation is absorbed in a thinner region under the surface being irradiated, leading to higher surface temperatures [48]. The optical penetration depth for a metal is of the order of $10nm$. When photons are incident on the surface of a material, they couple with electrons, specially in the valence band of the molecule. The electrons, as a result, get excited from their ground state to the excited state. The time it takes for the photons to get absorbed is called the photon absorption (T_a) is of the order of $1fs$. It should be noted that not all electrons transition to the same excited state. The electron transition happens to both the electronic and vibrational excited states, depending on the Boltzmann distribution of the electrons in the ground state.

In general, for laser material processing, two different laser pulse duration regimes are used: long pulse duration, such as nanosecond pulse duration, which generates quite a significant heat-affected zone in the material because "the pulse duration is longer than the thermalisation time of most metals" [4]. Long pulses applied with sufficient intensities ($I > 10^{10} W cm^{-2}$) lead to the formation of laser-induced plasma, significantly reducing the amount of radiation that contributes to interaction with the solid-state material. In contrast, ultrashort laser pulses are not shielded by the plasma, and interact directly with the material surface, due to the negligible spatial expansion of the plasma during the extremely short time interval. Short pulse duration (picosecond laser) and ultra-short pulse duration (femtosecond laser) yield better results, suited to the production of high-precision micro- and nanomachining. The high potential for ultrashort pulse laser micromachining arises from the fact

that heat diffusion can be minimized and the interaction process is mainly determined by the optical penetration depth. In the regime of low laser fluence, high precision processing is thus possible with negligible heat affected zones and practically no burr formation. Moreover, the laser fluence threshold is much lower than for longer pulses due to the reduced thermal losses. Therefore, lower pulse energies can be used for processing, resulting in significantly reduced mechanical damage around the processed area.

Laser micromachining using ultrashort pulses is often called "cold ablation". It expresses that the area surrounding the ablation crater largely remains cold during the ablation process. The descriptive explanation is that the light is absorbed by the electrons and the energy is slowly transferred to the lattice. If the pulse duration is much shorter than the transfer process, no heat conduction in the lattice can occur within the time scale of the laser pulse and the surrounding area remains "cold". It is worth mentioning that during the interaction of an ultra-short laser pulse with materials, heat conduction is limited [49]. As a result of this, the material will be ablated within a spatial or well-defined area with minimised mechanical and thermal damage of the ablated area on the target. In contrast, longer (nanosecond) pulse duration irradiation on the materials leads to continuously heating the target material. The laser pulse energy will then be spread by heat conduction to an area outside the laser spot size, causing the irradiated target to boil and evaporate. Boiling and evaporation of the target material leads to the production of an uncontrollable melt layer [50]. In the case of nanosecond laser pulse duration, this problem may cause imprecise machining.

After laser-material interaction with short pulses and low intensity, due to the inverse Bremsstrahlung, the laser beam energy will be absorbed by free electrons from the material followed by thermalisation within the electrons, and energy transfer to the lattice. Finally, energy will be lost due to electron heat transfer to the target material. The energy transfer from the laser beam to the target material can be described using 1D and 2D diffusion models when this is considered rapid thermalisation in the electron subsystem and if both lattice and electron subsystems are

characterised by their temperatures (Ti lattice temperature and Te electron temperature) [50]. In nanosecond laser, it was shown that the laser pulse duration has an effect on both the material ablation thresholds and penetration depths. Long pulse duration or increasing laser pulse duration increases the threshold fluence and decreases the effective energy penetration depth [51]. Low-intensity long laser pulse interaction with a target material firstly heats the surface of the target due to the absorbed energy, which leads to melting and vaporisation. It should be noted that vaporisation of the target requires much more energy than melting.

2.1.2 Laser Surface Texturing

Laser Surface Texturing consists of creating an array of high-density micro-dimples on a metal surface by laser ablation. If properly designed, the macroscopic effect of such a micro structure is an enhancement of the load capacity, wear resistance, and friction properties of the laser-treated surface. The study of mechanisms leading to femtosecond laser ablation of materials has long been a subject of interest for researchers. The need for such studies arises for contact-less and accurate machining control and less undesirable effects generated from the heat based material removal processes. Laser machining has gained popularity because of its applicability with all kinds of materials with little constraint on material properties. Machining depth control at the lengths scale of ten nanometers is possible with ultraviolet and ultrafast lasers. Many of the parameters of laser surface texturing must be optimized in order to get high quality, precise micro-craters. The resolution, for instance, depends on the wavelength of the laser source, whereas the ablation rate is based on energy density, and the depth of the craters is controlled by the number and duration of the pulses [52].

It is well known that metals are very problematic materials for micro-structuring with lasers owing to their high thermal conductivities and low melting temperatures. With conventional laser systems delivering pulses longer than 1 ns, the ablation of metals is always accompanied by the formation of large heat-affected zones and a throw out of the molten material. This limits the achievable precision and the quality of the produced structures. A significant improvement in this field has become

possible owing to ultrashort-pulse lasers. The main features of femtosecond-pulse laser ablation are (i) very rapid energy deposition and creation of vapor and plasma phases, (ii) absence of the molten material, and (iii) negligible heat-affected zones.

As a result, high-aspect-ratio/high-density structures of micro-holes can be successfully fabricated over steel and copper, where fast energy deposition and negligible heated zones are guaranteed at such laser material interaction timescales. Therefore, no burrs create on the edges of the micro-dimples, which could be detrimental to the desired tribological behavior, and no further polishing of the surfaces is required after LST. Furthermore, femtosecond laser ablation allows finely control the depth and the geometry of the dimples with micrometer precision. It has long been known that micrometer-scale surface irregularities affect the load capacity of parallel sliding surfaces [26], however only recently have such textures been engineered to improve friction performance of mechanical parts [27, 28]. We have found that depending on the microgeometry of the surface texture, the coefficient of friction under lubrication regime can be accurately controlled. In particular, when the texture consists of a square lattice of circular micro-dimples, the friction values are strongly reduced [53]. The experiments further revealed that an optimal void density and a depth value (depending on the dimple diameter) exist which minimize friction at the interface. Up to 85% of friction reduction has been demonstrated in a wide range from the boundary to the hydrodynamic regime [54]. It was also found that an elliptical texture allows adjusting the friction coefficient by changing its orientation with respect to the sliding direction [55]. Vladescu and Reddyhoff have gained an insight into the interactions between laser-textured surface pockets and friction and wear behaviour of an automotive piston-liner pairing. They found a significant improvement in the relative performance of the textured specimens, showing reductions in friction of up to 70%, compared with the non-texture case [104].

2.2 Mechanism of laser ablation of metals

Metals differ from dielectrics and semiconductors by a high density of quasi- free electrons (“electron gas”) that causes their comparably high values of electrical and

thermal conductivity and determines their optical properties, i.e. the interaction with light. At the high intensity levels that can be achieved with ultrashort laser pulses multiphoton absorption followed by impact ionization produces such an electron gas even in dielectrics and semiconductors, making them "metallic" [56, 57]. When the incident radiation is below the threshold for dielectric breakdown (and plasma formation, $10^{13} W/cm^2$ [58], the material is pushed into a metastable state due to sudden heating. At low fluences, and for pulses with durations greater than 100 ns, vaporization has been stated to be observed [59]. The recoil pressure due to the expanding vapor is responsible for the melt ejection (material removal) in this case. The action of recoil pressure leaves behind a surface with poor quality. It is important to note that melting, and redistribution of melt towards the boundaries of the irradiated region has been observed even in femtosecond laser irradiation of metals [60]. Ablation of metals with femtosecond lasers characterized by rapid overheating and thermalization of the electrons within the optical penetration depth. Due to the low thermal capacity of electrons in comparison with the lattice, the electrons are rapidly heated beyond the Fermi level to very high, transient temperatures, forcing an extreme non-equilibrium state between the electron and lattice system.

The discussion of laser ablation mechanisms in metals requires an understanding of some thermodynamic concepts and processes, like the binode, thermodynamic critical point, spallation and phase explosion. The binode (or the binodal curve) is the region where two phases coexist in a thermodynamically stable manner. The binode originates from the triple point (for pure materials) and ends at the critical point (T_c). The thermodynamic critical point is the extremum of the binode. It represents the maximum pressure and temperature at which two phases can coexist. A slight decrease in pressure or increase in temperature causes the phases to merge into each other and the phase boundaries to disappear. If the system is allowed to cool (relax) from the critical point, it follows the binode. Spallation is the transition of a material into a solid-gas phase due to strong pressure tensile waves [61]. Sudden heating of a material, by a laser pulse of high fluence and short duration causes stress confinement, leading to generation of compressive stresses. Also, called photomechanical ablation [60], spallation is caused by the release of compressive stresses.

Spallation causes the material to fracture and break into fragments of solids or liquid droplets. For spallation to occur, both the laser pulse duration and the electron cooling time have to be shorter than the characteristic time for thermal expansion. Under such conditions, the material gets heated by the laser pulse almost isochorically, thereby causing stress confinement. Phase explosion, also known as explosive boiling, occurs when the rate of homogeneous nucleation of bubbles is very large due to superheating, and when the surface temperature exceeds 90% of the critical temperature (T_c) [62]. As a consequence, the material is turned from a superheated liquid into a mixture of liquid droplets and vapor, being explosively ejected from the surface. The onset of phase explosion is marked by the observation of liquid droplets in the ejected material, and a sudden increase in ablation rate. Researchers had observed liquid droplets in the plasma plume of some metals [48, 63, 59]. Following the rapid expansion, the material relaxes towards the binode. Lorazo *et al.* (2003) and Miotello and Kelly (1995) performed molecular dynamics studies of systems under irradiation with pulses of durations from femtoseconds to picoseconds [58, 64]. For irradiation with ultrashort pulses (pulse duration $\leq 1ps$), and especially close to the threshold energy, the heating is so rapid that the material gets superheated near-isochorically [58]. It takes about 1 ps for the laser energy to be transferred to the atoms/ions. Thermal expansion cannot take place at this timescale, and hence, a highly pressurized and superheated liquid is formed. Subsequently, the pressure is released through expansion, beginning from the surface(s). At high energies, the release of pressure by expansion causes fragmentation of the liquid [61]. At lower energies, the expanding material reaches a metastable state (spinodal) after the onset of adiabatic cooling and approaches the liquid-gas regime. Homogeneous nucleation of bubbles takes place around this time, and separation of liquid and gas phases begins, also called phase explosion. When phase explosion happens under conditions when compressive stresses have been generated, the material is ejected with higher velocities and is more fragmented [60]. The incident radiation couples with the valence electrons in the metal and excites them. The excited electrons gather large kinetic energy and leave behind the positively charged ions. The closely packed ions repel each other and the metal explodes out, forming a plasma.

The interaction of the laser beam with a material, goes through the process of the reflection, absorption and transmission. But, in the case of metallic materials, the

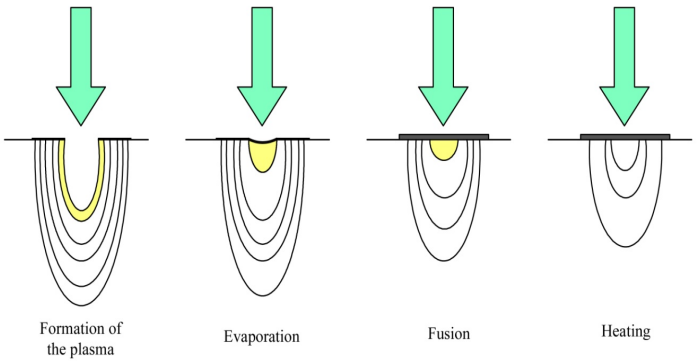

FIGURE 2.3: Examples of material removing using a laser

transmission could be neglected due to the density and reflection depends on the refractive index(n) of the material and surface condition. Considering now the absorption, it is linked to the capacity that have electrons and atoms of the crystal lattice of interacting with the incident photons (laser beam), and get excited, starting to vibrate. This vibration is transmitted into the structure (phonons) and the macroscopic behavior of the material is perceived as heat. The electromagnetic energy absorbed by a material is expressed by the Lambert- Beer law:

$$I_A(z) = I_0 \; e^{-\beta z} \tag{2.1}$$

where I_A and I_0 are, respectively, the absorbed and the incident intensity, z is the direction of propagation of the radiation and $|\beta|$ is the attenuation factor, linked to the material. From Lambert-Beer law is defined, as the optical penetration depth, $(\delta) = \frac{1}{\beta}$, where $|\beta| = 2/\alpha$,i.e. the distance at which $I_A(z) = \frac{I_0}{e}$. Properties such as the Thermal Diffusivity allow the transmission inside the means of the thermal energy absorbed at the surface. If the energy of the radiation is sufficient, it will be possible to separate the bonds, coming to the melting of the material, or by increasing the energies, to its evaporation. It can even switch to the plasma state, i.e. in which some electrons have left the gaseous atoms, fig. 2.3.

One of the most common ways of electron relaxation is through vibrational relaxation. The energy of the excited electron is transferred to a vibrational mode of the molecule, as its kinetic energy. This manifests itself in terms of rise in temperature

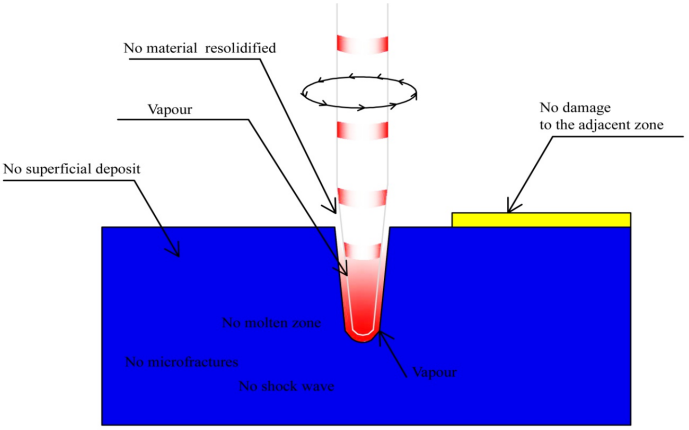

FIGURE 2.4: Example process for an ultrashort laser pulse

of the material. During the relaxation between vibrational levels, the electronic energy levels do not change, unless the vibrational states overlap strongly with the electronic energy states, in which case the process is called internal conversion. The time it takes for the excited electrons to relax is called the electron relaxation time (or electron cooling) and ranges from 10 fs *to* 10 ps. Vibrational relaxation and internal conversion are almost always present as relaxation pathways, but are mostly not the final transitions. After about $1ps$ of irradiation, the electrons relax and pass on the energy to the lattice in the form of heat. This heat diffuses into the material at the rate determined by the thermal diffusivity ($|\alpha|$) and thermal conductivity (k) of the material [65, 66, 67]. The thermal diffusivity $\alpha = \frac{k}{\rho\ c_p}$, with k the thermal conductivity, density ρ and c_p the specific heat, which tells us the energy required to melt the material, and $4\alpha\tau_i$ (τ_i is the pulse duration) that represent the depth at which the temperature is $\frac{1}{e}$ compared to that on the surface. D (Thermal Penetration Depth) = $(\sqrt{4\alpha\tau_i})$.

The pulse duration is a property of the laser radiation. However, the pulses are classified as short or ultrashort based on whether the optical penetration depth is more or less than the thermal diffusion depth. Generally speaking, pulses with duration less than 1 ps are called ultrashort pulses. For longer pulses, it is the thermal conductivity that determines the depth of the laser-induced modification, while for ultrashort pulses it is the optical penetration depth. Also, the order of magnitudes of the two depths and therefore of the modifications are quite different:

micrometers versus tens of nanometers. An often used term in laser machining is 'fluence'. Fluence is defined as the irradiated energy per pulse per unit area of the material, and its units are j/cm^2. Ablation is noticeable only above a certain value of fluence (depending on the material) and this value is called the threshold fluence (Fth). It has been realized that instead of fluence (that makes no reference to the time in which the energy is delivered), intensity better describes the effect of radiation [68, 69]. Intensity, then, is defined as average power per pulse per unit area. The term ablation refers to that particular process of material removal by laser beam, in which there is the direct passage of the solid-vapor phase. The ablation is achieved by using a pulsed laser, with ultrashort pulses, in order to establish a condition, thermal penetration depth(D) > optical penetration depth(δ), required for the process. For pulse widths, so short, heat is not transferred within of the crystalline structure, retaining the solid material. However, energies are so high that there is the breaking of the bonds of the crystal lattice, causing a direct transition from solid to vapour state without creating heat-affected zone, fig. 2.4. Finally, it leads to reduction in the thermal effects on the textured surface or ablated surface and also provides improved quality on geometry and shape of the edges. An important property of light is that it has no volume, photons have no charge, so when concentrated into a very small space, they don't repulse each other like negatively charged electrons do. This is a very important property for ultrashort machining.

2.2.1 Processing technologies

The LST technique can be understood as a particular laser milling technique with source as ultrashort pulses. In fact, every dimple can be considered as a single hole of certain depth. There are three ways to perform superficial laser machining or drilling tests (shown in fig. 2.5):

Single Pulse Drilling: It allows texturing dimples with an aspect ratio less than 15:1, with a high scale production and lesser degree of precision. Percussion Drilling: In this technique, there is a series of successive laser pulses emitted on the same spot of the surface., which leads to reduce the processing time. But, it has some problems,

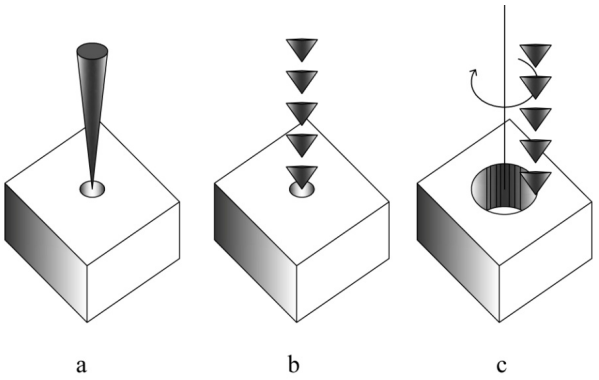

FIGURE 2.5: Modalities for the LST: a) Single pulse drilling; b) Percussion drilling; c) Trepanning

e.g. the formation of the re-solidified material layers along the walls of the hole (recast layer), on the top of the hole(spatter) and tapering off the walls. Trepanning Drilling: It combines the percussion to a rotation around the center of the spot, by operating the laser as a milling tool. It can produce dimples with high precision and minimum tapering effect, but still it has some burrs at the top. The quality of the dimples depends upon the number of cycles and power of the lasers. Nowadays femtosecond lasers made the dimples by using trepanning technique to be fully burr free and highest accuracy.

2.3 Optimization: Surface texturing parameters

Most of the research done on surface texturing is experimental, except for a few analytical studies that try to optimize the surface texture parameters. In the following subsections, analytical studies are reviewed and followed by experimental investigations.

2.3.1 Analytical Studies:

Etsion and Kligerman [3] developed a theoretical model to identify the most significant parameters under hydrodynamic sliding conditions, specifically for mechanical seals. The seal was represented by two non-contacting concentric cylindrical surfaces rotating relative to each other. The micro-pores of spherical segment shape were

distributed uniformly over one of the annular surfaces as shown in fig. 2.6. According to the basic assumptions accepted in this work the seal faces are separated by a uniform gas film thickness. The sealed gas is compressible and viscous (Newtonian) with a constant viscosity. Effects of curvature of the cylindrical surfaces are neglected because of the small value of the seal clearance relative to the seal radius. The hydrodynamic dimensionless pressure distribution in the uniform clearance between the annular surfaces is obtained from a solution of the Reynolds equation for compressible viscous gas in a laminar flow. Results of a parametric study along with a numerical example for a specific circumferential seal demonstrate a substantial hydrodynamic effect that can raise the opening average pressure in the seal clearance above the ambient one by up to 50%.

Based on the findings of an earlier study that promoted evenly distributed microtextured patterns in order to increase the load carrying capacity, hemispherical dimples arranged in a rectangular layout were modeled. This study suggested that an optimal texture size could be found based on lubricant properties, pressure difference across the seal, and the areal density of the texture. A more sophisticated model [28, 44] was developed by the same group, incorporating more accurate cavitation data and using a non-spherical pattern. It was found that the most significant parameter was the diameter to depth ratio. A diameter to depth ratio of 0.05 was identified as the optimal value, versus a ratio of 0.5 which was obtained from the first model of a hemispherical 10 pattern [3]. The improved model showed agreement with the experimental results that involved a simple sliding textured rig. Etsion *et al.* [27, 42] developed another analytical model to simulate the piston ring-cylinder liner system. The ring and liner were modeled as two parallel flat surfaces where only the ring surface was dimpled, and a reduction of 30% in friction was obtained. The optimal diameter to depth ratio was found to be between 0.1 and 0.18, and areal texture densities varied from 5% to 20% which contradicted with the values found by Stephen [70]. This analytical study showed a similar trend to the experimental test, however, the exact values differed due to the adjustment in the lubricant viscosity assumed in the analytical study. The effects of micro-pores as lubricant reservoirs for a highly-loaded, boundary lubrication condition was studied by Zhao *et al.* [71]. This research developed a finite element model of a rigid cylinder in contact with an elastic and elastic-plastic half-space with lubricant filled micro-pockets. The results

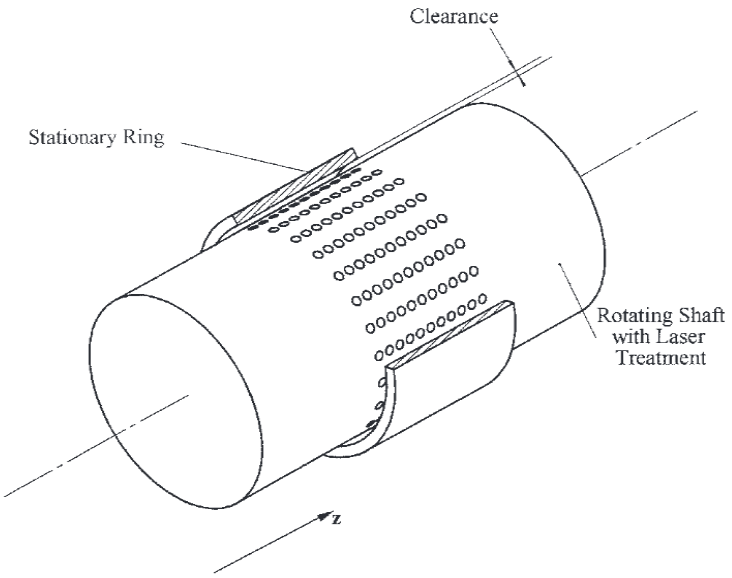

FIGURE 2.6: Circumferential gas seal Schematic [3].

showed a reduction in the volume of these micro pores with loading, therefore if those pockets are filled with lubricant, the squeezed lubricant will partially support the applied load. This reduces the surface-to-surface contact between the rigid cylinder and the textured surface. Comparing the empty micro-pore with the micro-pore filled with lubricant, the pressure spikes and the sub-surface stresses of the filled micro pore are lower than in the empty one. Stephens and Sirpuram [70] addressed the effects of different texture shapes of positive and negative texturing. Square, diamond, circular, triangular and hexagonal shapes were modeled, with different area densities under a hydrodynamic lubrication condition. Two objectives were sought in this study, the effects of the shape and the texture areal density on the coefficient of friction and leakage rate. They found that the shape of the texture has an important effect on the friction coefficient; however, it had a great impact on the leakage rate. The square pattern provided the worst leakage rate, and the triangular pattern gave the best leakage rate. In addition, the texture areal density affects the minimum friction coefficients, which were obtained at 20% and 80% of the areal texture coverage for the friction control. Tnder [72, 73] proved analytically that a micro textured region can replace a macro feature, such as step or inclined plane, in creating hydrodynamic pressure in sliding seals. The role of either the macro feature or the proposed micro textured area is to decrease the friction which

the entering flow to the seal encounters. In this analytical study, grooves oriented perpendicularly to the flow direction were modeled, as well as square and circular discrete dimples. All texturing designs showed improvement in the hydrodynamic pressure and the leakage rate.

2.3.2 Experimental Studies:

In the analytical methods, the mechanisms that control friction must be accurately defined; on the other hand, various tribometers (pin-on-disk, ball slider, or scratch tester) can directly measure the friction coefficient. Many researchers have investigated the effects of surface texturing on the friction experimentally under different sliding conditions. However, most of these studies focus on wet conditions. Varenberg *et al.* [74] investigated the influence that groove depth had on wear and friction. In the cases where friction was concerned, wider grooves lead to greater friction reduction due to the fact that more wear particles could be contained in the grooves. Friction also decreased with the groove depth to a point, after which increasing the depth had no effect. They deduced that wear debris fell into the surface depressions. The particles first gathered around the edge of a dimple and then built inward and downward, not necessarily ever reaching the bottom. Once the depth of the groove was below the lowest particle size that the wear particles could reach, there was no benefit to creating a deeper groove. Another study was carried out by Ryk *et al.* [45] that showed the negative effect of dimples under boundary lubrication conditions, if the depth of the groove is not appropriately chosen, or if the lubricant feed rate is not sufficiently high. This study showed that the deeper the dimples are, the higher the friction is. In addition, at a very low rate of lubricant supply, the friction resulting from the textured surface is higher than that of the flat surface.

Kovalchenko *et al.* [75] looked into the effects of laser surface texture on the lubrication regime transition. Specifically, the effects of the sliding speed, normal pressure, and the lubricant viscosity on the friction were tested. A pin-on-disk apparatus was used in this case, and the laser surface texturing had more impact on friction in cases of higher normal loads, higher sliding speed, and higher viscosity. Pettersson and Jacobson [36], studied the effects of the surface texturing of coated silicon under

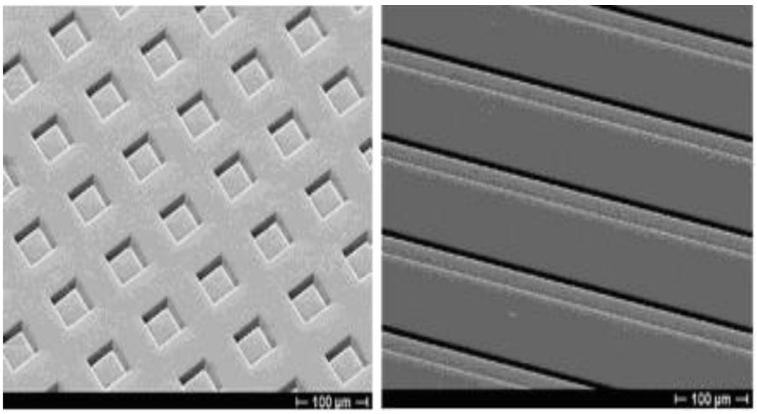

FIGURE 2.7: Textured squares and grooves by Pettersson and Jacobson [4]

boundary and dry sliding conditions. Etched silicon samples were coated with either TiN or DLC. This study showed the critical impact of the material interaction under oscillating sliding by a ball slider. Two texturing designs were investigated, grooves and square dimples as shown in fig. 2.7. The results of this study were compared to un-textured samples. Under boundary lubrication conditions, the DLC coating with square dimples showed stable low friction behavior, while the grooved texture showed high friction. The textured TiN coating behaved differently and showed unstable friction behavior on all texturing patterns. In dry sliding conditions, the DLC coating showed high friction when compared to the untextured surface. DLC has self-lubricating properties where a thin low friction tribofilm was formed on the surface. When the DLC coated sample was textured, the sharp edges of the pores scraped off the thin tribofilm causing the fluctuations in the friction behavior. On the other hand, the TiN textured samples showed low friction with both the square and groove patterns.

Suh and others [76, 28, 77, 32] tested the effect of the width and orientation of undulations with respect to the sliding direction on the friction and wear, under boundary sliding conditions. Pin-on-disk tests were done, with the disks textured by abrasive machining. Grooves which were parallel to the sliding direction showed no improvement in either friction or wear. Yet, grooves perpendicular to the sliding direction decreased both the wear and friction. In addition, attention was drawn to the effect of the lubricant properties on the results.

2.4 Summary

Based on the literature review, micro surface texturing has proven to be an effective means of enhancing tribological performance. Most of the studies investigated the effects of micro surface texturing in wet conditions, with a very limited number of studies tackling the dry sliding condition. Most of the studies showed the potential benefits of adding micro surface texturing to one surface of the contact pair in different conditions (sliding or rotating). Moreover, micro surface texturing effects differently in each lubrication regime and there presence seems to be detrimental in conformal contacts [104, 105, 106]. In full (hydrodynamic) lubrication mode, the dimples develop pressure differences, thus they act as bearings. In the boundary lubrication mode, the texture pores provide a continuous lubricant supply to the contact interface, which decreases surface to surface contact. In the dry condition, they act as traps for wear debris so that plowing decreases.

Chapter 3

TRIBOLOGY

Tribology is derived from the Greek word "Tribos". Meaning of Tribos is Rubbing [8]. Tribology involves the study of lubrication, friction and wear. It is thus an interdisciplinary science, connecting knowledge of physics, chemistry, metallurgy and mechanics. The subject of tribology was first defined in a British Department of Education and Science Report in 1966 as: "The science and technology of interacting surfaces in relative motion and the practices related thereto" [5]. Recently, this discipline had had a huge development, becoming a pivotal frontier to be explored in the context of basic and applied Physics.

However, the history of tribology is ancient, but the science did not get its name until the 20th century. The earliest experiences encountered in this field are placed in prehistoric ages due to the firsts tool manufacturers, sculpting bones and metals. Remarkable pioneering traces could be retrieved even in ancient Egypt. The famous picture reported in fig. 3.1 (datable around 2400 BC) portrays slaves dragging a monolithic statue along a wooden skid. A standing man is recognizable on the plinth: he is pouring a liquid into the path of motion, deserved to be considered a forerunner lubrication engineer [6]. Nevertheless, the wheel invention determined a huge progress, reducing friction (from grazing to volving) occurring in transport mechanisms. Aristoteles (384-322 B.C.) was the first to recognize the force of friction. Leonardo da Vinci (1452-1519) studied and documented friction experiment and he concluded that the friction force is proportional to the normal force. In 1699

FIGURE 3.1: The first recorded tribologist, pouring lubricant (probably water) in front of the sledge in the transport of a statue in Egypt (2400 B.C.) [7]

Amonton established the concept of asperity interaction [9]. Leonhard Euler (1707-1783) was the first to introduce the parameter μ, denoting the coefficient of friction, and he was also the first to make a clear distinction between static and dynamic friction. However, the term "tribology" became widely used only in the last century, in coincidence of the enormous industrial growth. Tribological knowledge helps to improve service life, safety and reliability of interacting machine components; and yields substantial economic benefits.

At present, the state of the art of the knowledge is far to guarantee a definitive and exhaustive comprehension of the mechanisms of friction and wear, but lots of progress have been made due to the several efforts recently spent in research. Thus, nowadays tribology is meant to be crucial for the scientists, especially due to the considerable impact on modern machinery which is based on sliding and rolling contacts. Industry of today needs to be able to reduce or control friction and wear to improve safety and to save money, energy and environment. Economic perspectives and long-term reliabilities gave a fundamental lift towards the wide diffusion of tribology, justifying the origin of several research centers for tribology, and the training

of high-quality tribologists, whose main purpose of research is the minimization and elimination of losses resulting from friction and wear at all levels of technology where mating surfaces are involved. Therefore, the results in this discipline lead to optimize the efficiency of the systems obtaining higher performances, fewer breakdowns, and significant savings. Similar aims have historically been achieved by design changes, selection of improved bulk materials or lubricants. Recently tribologists have become more focused on surface engineering as a tool control friction [78]. Components can be optimized by using a bulk material that is selected for the mechanical strength and toughness combined with correct surface treatments or coatings for the best tribological performance. The surface is the most important part of many engineering components since it both sets the functional properties, such as friction and wear, and determines the lifetime. In the last decades, the development of the microscopic devices forced tribology to move towards the Micro or Nano-scale, and to assume a new importance and interest. The extension of the range of the tribological investigations opens several classes of problems related to the scaling gap. The advent of new techniques to measure topography, adhesion, friction, wear, lubricant film thickness, and mechanical properties, all micro- to nanometer scales, led to the development of the respective sub-fields of the tribology, separated by different approaches and laws that govern and explain the interfacial phenomena. Providing a bridge among them is a tough challenge towards a fundamental and complete understanding.

3.1 Friction

Friction is the tangential resistance to motion. The occurrence of friction is a part of everyday life. It is needed so that we have control on our walking. On the other hand, in most of running machines friction is undesirable (energy loss, leading to wear of vital parts, deteriorating performance due to heat generation) and all sorts of attempts (i.e. using low friction materials, lubricating surfaces with oil or greases, changing design so that sliding can be reduced) have been made to reduce it. Often coefficient of friction(μ) is considered a constant value for a pair of material. In addition, the value of μ is accounted much lesser than 1.0. In practice μ greater than 1.0, as shown in Table 3.1, has been observed. Generally, coefficient of friction depend on parameters such as temperature, surface roughness and hardness. fig. 3.2

Aluminium	1.5
Copper	1.5
Gold	2.5
Iron	1.2
Platinum	3.0
Silver	1.5

TABLE 3.1: Coefficient of friction for various metals sliding on themselves [6]

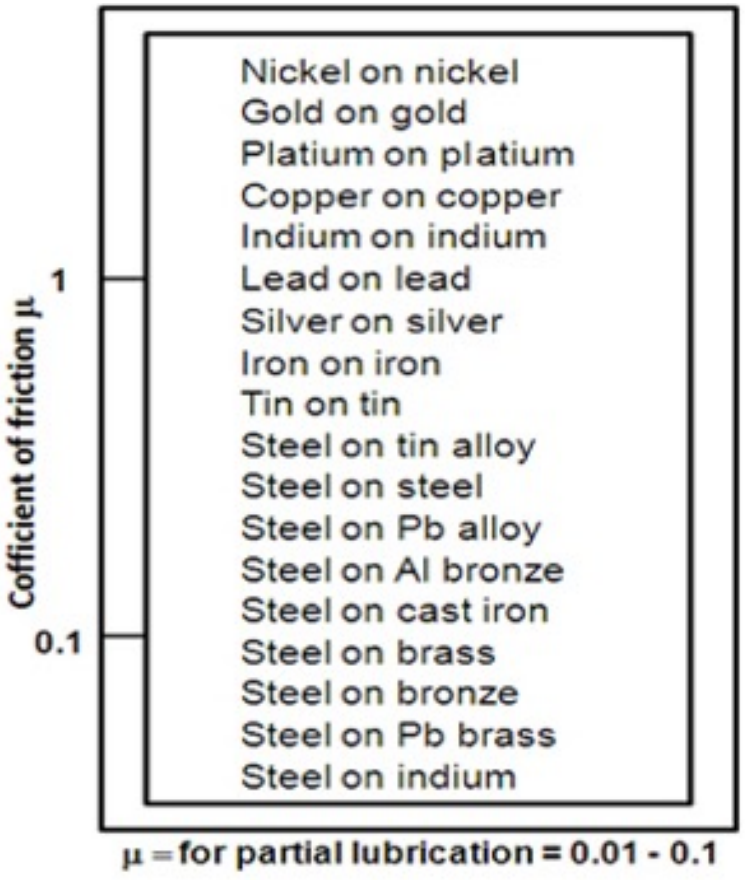

FIGURE 3.2: Coefficient of friction for various metals [5, 6]

indicates that under dry lubricant conditions, μ ranges between 0.1 to 1.0 for most of the materials. Very thin lubrication reduces coefficient by 10 times. Generally, adhesion (fig. 3.3) increases the friction. So, while selecting metal pairs, low adhesion metal pairs must be selected to reduce friction force. Similar material pair must be avoided as similar materials have higher tendency of adhesion.

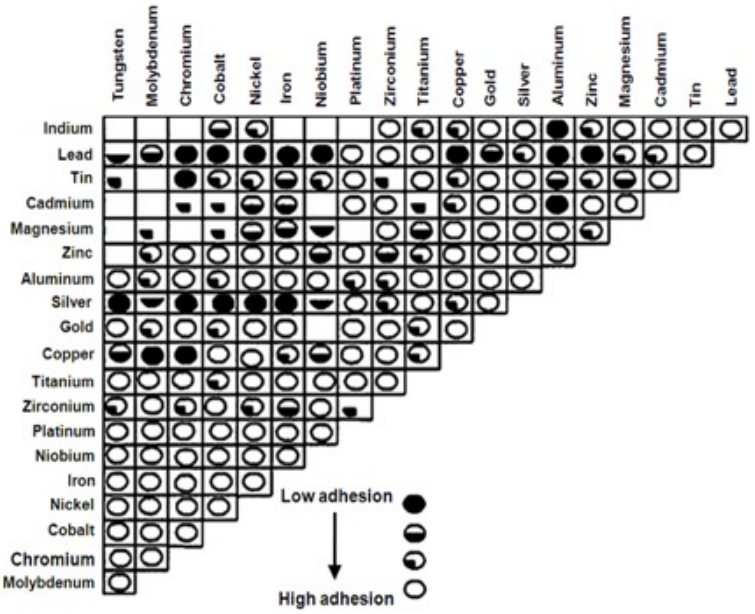

FIGURE 3.3: Adhesive Friction among various materials [7, 6]

3.1.1 Static & Kinetic Frictions:

Before starting friction mechanisms, it is necessary to define static and kinetic friction. Let us consider a block on the surface getting pushed by a tangential force F. On application of 20 N load, block does not move. This second point on the graph (fig. 3.4) shows that on application of 40 N, still block does not move. There is static force equilibrium between application force and friction force. On application of 50 N load, block just start sliding. At this point of load application friction force remains equal to 50 N, but friction resistance decreases subsequently to 40 N. In other words, static friction is higher than kinetic friction. It is difficult to obtain same value of friction coefficient under various laboratory conditions. Further, there is a possibility of substantial decrease in kinetic friction relative to static friction. Stick-slip is a phenomenon where the instantaneous sliding speed of an object does not remain close to the average sliding speed. Stick-slip is a type of friction instability. To understand the effect of material pair, role of lubrication, and environmental factors let us start with dry friction. The dry friction is also known as solid body friction and it means that there is no coherent liquid or gas lubricant film between the two solid body surfaces. Four theories given by Leonardo da Vinci, Amonton, Coulomb and Tomlison for dry lubrication are explained in following paragraph.

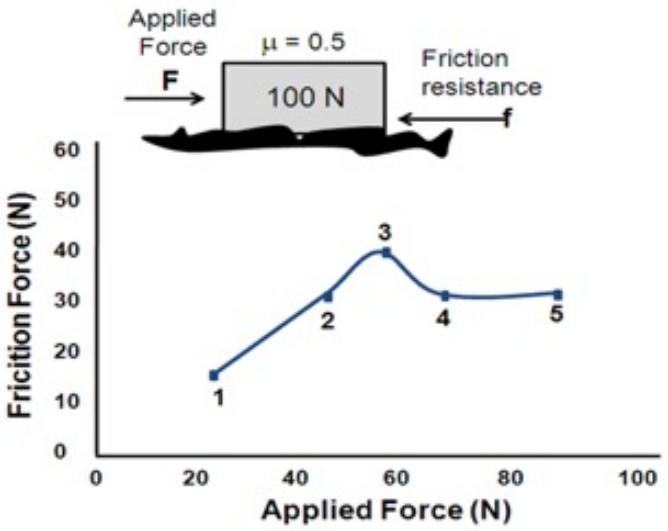

FIGURE 3.4: Difference between the static and kinetic friction may initiate 'stick-slip'[8]

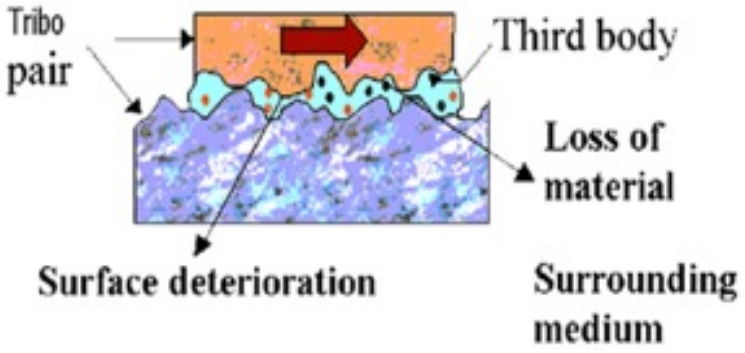

FIGURE 3.5: Amonton's work[9]

- **1. Leonardo da vinci (Earliest experimenter, 1452-1519):**
  Leonardo studied the sliding of blocks on inclined plane, varying blocks masses and angles of inclination. He derived the definition of static friction measuring the load and the inclination necessary to start the block motion, and he observed the independence of friction from the extension of the contact area between the sliding blocks and the inclined surface [79]. As per Leonardo, "Friction made by same weight will be of equal resistance at the beginning of movement, although contact may be of different breadths or length". "Friction produces double the amount of effort if weight be doubled". In other words, Friction(F) $\approx$ Weight(W).

- **G. Amonton's, 1699:**
  In practice, engineering surfaces are not atomically smooth but rough. This means that the real contact area in dry and thin film, lubricated contacts is much less than the geometrical contact area, while the local pressures at the contact points are much higher than the average value. This, in turn, strongly influences the tribological performance of machine components, such as friction, wear and rolling contact fatigue. At first, the well-known Amonton's laws of friction shall be recapitulated. Amontons studied sliding friction in dry systems in 1699 [9], and he considered three cases (fig. 3.5) and showed that friction force will vary as per the angle of application of load and formalized three results:

  1. Friction is proportional to the applied load,

$$F_f = |\mu| N, \tag{3.1}$$

  where F_f is the friction force, N is the applied load and $|\mu|$ is the friction coefficient (Amonton's first law).

  2. The friction force is independent of the nominal area (F $\neq$ A) of contact between two solid surfaces. (Amonton's second law).

  3. Friction depends only very slightly on the sliding speed (Coulomb's first law).

- **3. C. A. Coulomb 1781 (1736-1806):**
  Coulomb made the first clear distinction between static and kinetic friction. Friction due to the interlocking of rough surfaces and published some experimental results about metal and wood [7]. His contribution was completed with the formulation of the well-known Coulomb's law:

  Contact at discrete points μstatic $\geq$ μkinetic.

  - $f \neq func(A)$.
  - $f \neq func(v)$.

  As per Coulomb friction force is independent of sliding speed. But this law applies only approximately to dry surfaces for a reasonable low range of sliding speeds, which depends on heat dissipation capabilities of tribo-pairs.

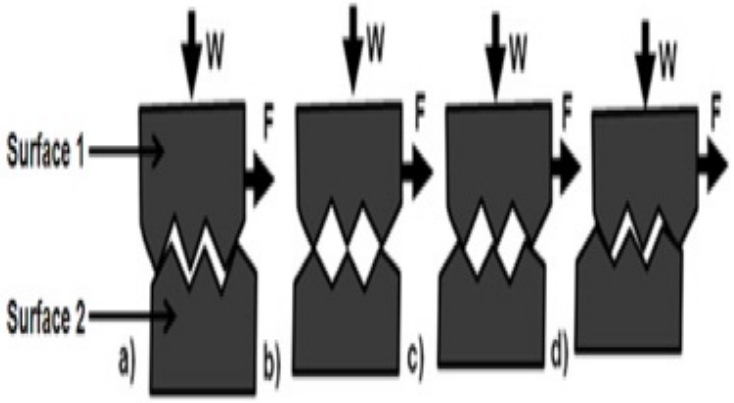

FIGURE 3.6: Coulomb friction model [7, 6]

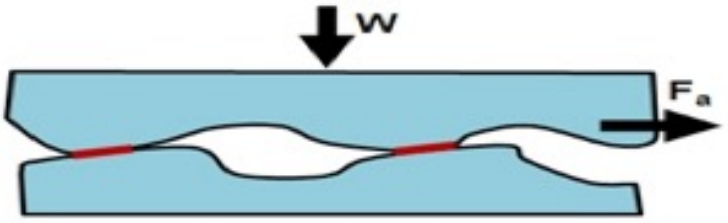

FIGURE 3.7: Adhesion [10]

3.2 TOMLINSON's Theory of Molecular attraction, 1929:

Tomlison based on experimental study provided relation between friction coefficient & elastic properties of material involved. As per Tomlison due to molecular attraction between metal, cold weld junctions are formed. Generally, load on bearing surface is carried on just a few points. These are subjected to heavy unit pressure, and so probably weld together. Adhesion force developed at real area of contact.

$$F_a = 1.73 \times (\theta_I + \theta_{II})^{2/3}, \tag{3.2}$$

and

$$\theta = \frac{3E + 4|\tau|}{\tau(3E + |\tau|)}, \tag{3.3}$$

where E is the Young modulus and $|\tau|$ is the shear modulus.

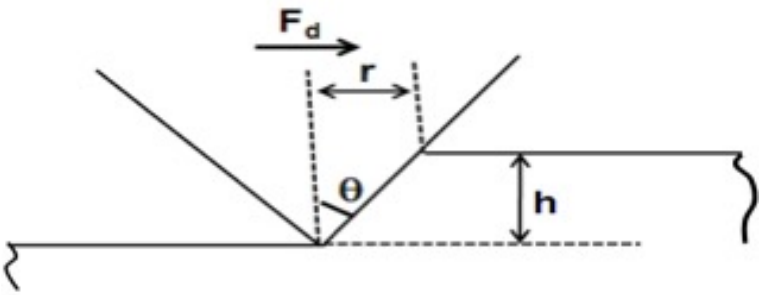

FIGURE 3.8: Abrasion(Deformation) [67]

3.2.1 Scientific Explanation of Dry Friction:

There are two main friction sources: Adhesion and Deformation (Force needed to plough asperities of harder surface through softer). In lubricated tribo-pair case, friction due to adhesion will be negligible, while for smoother surfaces under light load conditions deformation component of friction will be negligible. fig. 3.7 demonstrates the adhesion (cold weld) between two surfaces. Some force, F_a, is required to tear the cold junction. fig. 3.8 demonstrates the deformation process. It shows a conical asperity approaching to a softer surface. To move upper surface relative to lower surface some force is required. The Resulting friction force (F_f) is sum of the two-contributing force, which is Adhesion force (F_a) and Deformation (F_d) terms. In 1950, Bowden and Tabor theorized that the friction dissipation is a consequence of the sum of plastic deformations of the asperities during sliding under high pressure contacts. They definitely opened the debate about the not negligible adhesion between asperities, a topic already introduced by the rough speculations due to J.T. Desaguliers [80]. The main Bowden-Tabor work introduced the argument of the real contact area to explain the independence of friction to the apparent contact area [81] the projection of the surface of one mating body on the other one is several orders of magnitude larger than the sum of the areas of the contacting asperities. Therefore, the eq. (3.1) must be rewritten as:

$$F_f = |\tau| A_R, \tag{3.4}$$

where A_R is the actual contact area, and $|\tau|$ is the shear modulus (i.e. the friction force for area unit). This approach does not explain the linear relationship between friction force and applied load, but could be well adopted for all the macroscopic

systems. In 1966, Greenwood and Williamson [82] reconciled eq.(3.1) and eq.(3.4). Starting from the more simplified theory of Archard [83, 84], they developed a statistic theory of multi-asperity contact regime, based on a model that described the two contact surfaces through three parameters: the asperity density, the standard deviation of asperity height distribution (exponential and gaussian), and the asperity radius (first assumed to be hemispherical, later changed in a gaussian distribution [85]. This theory led to the conclusion that the ratio between contact area and load (and consequently between friction force and load) is linear. Other more complex theories with different distributions of asperity height and density, and with different asperity apex shapes, have been recently developed. None of these denies the linear dependence between contact area and load. The weakness of the Greenwood-Williamson model is in neglecting the adhesion contribute at interface. Thus, several further theories have been developed in order to take into account the roughness-adhesion connection, from Fuller-Tabor theory [86] to Persson-Tosatti approach [87] that works with self-affine surfaces (especially in this case roughness reveals a strong influence on adhesive forces). In a simplified description, the adhesive term could be introduced directly into the Amontons Law (eq. (3.1)):

$$F_f = |\mu|(N + F_0) \approx |\mu|N, \tag{3.5}$$

where k is a constant friction force due to adhesion, and F_0 is a constant adhesion force whose nature is the sum of different components: Van der Waals forces, electrostatic forces, capillary forces (or meniscus effects), chemical bonds, acid-base interactions. As mentioned above, reducing the scale of contact the interface mechanics changes dramatically. Several single asperity theories have been developed, based on different geometrical assumptions, including or neglecting the adhesion contribute and other short-range interface forces. All of them implies a power law relationship between applied loads (N) and contact areas (A_R).

$$\begin{aligned} A_R &= \pi(\frac{\tilde{R}}{K})^{2/3}N^{2/3}, \\ \tilde{R} &= \frac{R_1 R_2}{R_1 + R_2}, \\ \frac{1}{K} &= \frac{3}{4}(\frac{1-v_1^2}{E_1} + \frac{1-v_2^2}{E_2}). \end{aligned} \tag{3.6}$$

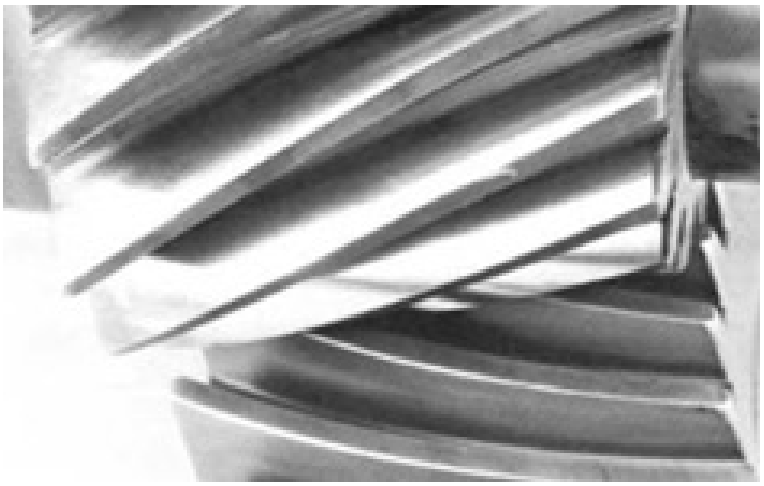

FIGURE 3.9: Zero wear of helical gear[5]

The simplest, and thus most famous and widest used one is Hertz theory (1881) that describes the perfect elastic, non-adhering case of the contact between two spheres of radii R_1 and R_2, Young moduli E_1 and E_2, Poisson's ratios ν_1 and ν_2 [88]. Other common single asperity contact theories are extensions or improvements of the Hertz theory such as Johnson-Kendall-Roberts (JKR) that describes sphere-flat coupling including adhesion forces and Derjaguin-Muller-Toporov (DMT) that includes a Lennard-Jones potential interaction at interface [77].

3.3 Wear

Undesirable removal of material from operating solid surface is known as wear. There are two definitions: (1) Zero wear: Removal of material which causes polishing of material surfaces may be known as "Zero wear". It may increase performance. It is for betterment, so it is not undesirable. Zero wear is basically a polishing process in which the asperities of the contacting surfaces are gradually worn off until a very fine, smooth surface develops. Generally, "polishing-in" wear is desirable for better life of tribo-pair. fig. 3.9 shows polished surface of helical gear which occurs due to slow loss of metal at a rate that will have a little effect on the satisfactory performance within the life of the gears. (2) Measurable wear: Removal of material from surface that increases vibration; noise or surface roughness may be treated as "Measureable wear". Often we measure wear in volume/mass reduction. Undesirable removal of

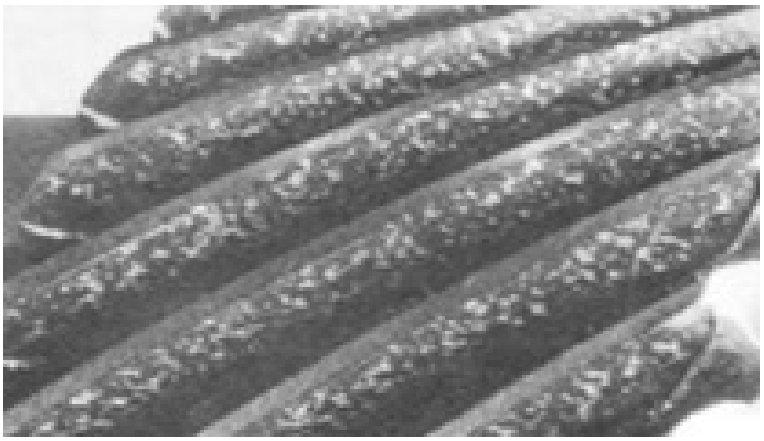

FIGURE 3.10: Measurable wear of helical gear [5]

material occurs in measurable wear. Measurable wear refers to a loss of material which must be counted to estimate the life of tribo-pair. The extent of measurable wear depends on the lubrication regime, the nature of the load, the surface hardness and roughness, and on the contaminants in the lubricating oil. A typical example of measurable wear in helical gear is shown in fig. 3.10 which is typically known as pitting wear. Pitting is a surface fatigue failure which occurs due to repeated loading of tooth surface and the contact stress exceeding the surface fatigue strength of the material. Material in the fatigue region gets removed and a pit is formed. The pit itself will cause stress concentration and soon the pitting spreads to adjacent region till the whole surface is covered with pits. Subsequently, higher impact load resulting from pitting may cause fracture of already weakened tooth. Sometimes impurities in materials provide nucleus for crack generation as shown in fig. 3.11 (c). fig. 3.11 (d) shows merger of generated cracks, which finally detaches from the surface as shown in fig. 3.11 (e). Such formation of pits (removal of material) comes under measurable wear. Many times, the change in surface profile alters the optimum value of clearance and reduces load capacity of machine components. Removal of material from operating solid surfaces by solid particles depends upon Load, Velocity, Environment, and Materials. Removal of material from operating solid surface by Fluid (liquid/gas) depends upon Velocity, pressure, Environment and material. As wear increases power losses increases, oil consumption, and rate of component replacement increase. Ultimately, it reduces efficiency of the system. Therefore, as far as possible wear should be minimized.

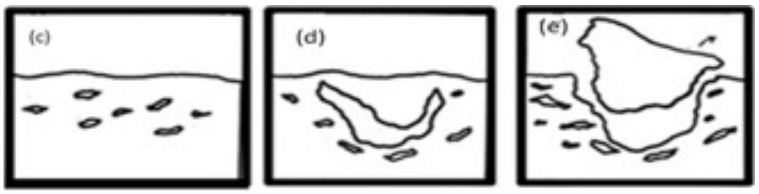

FIGURE 3.11: Formation of pit

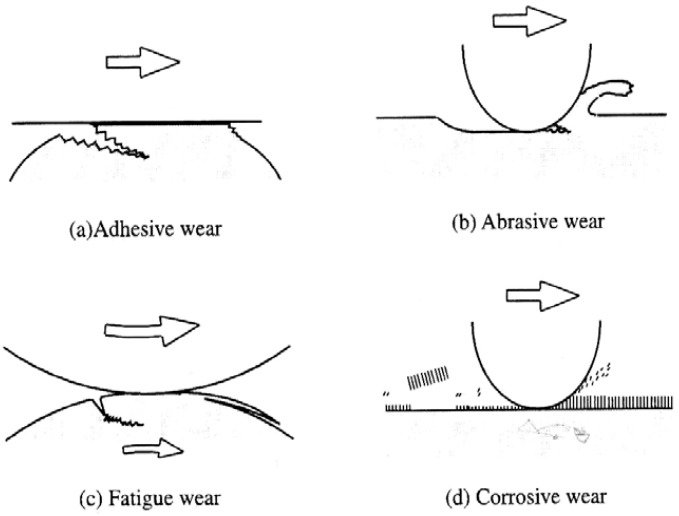

FIGURE 3.12: Schematic representation of the major wear modes: a) adhesive; b) abrasive; c) fatigue; d) corrosive [11].

3.3.1 Wear Mechanisms:

Wear can be classified based on the ways that the frictional junctions are broken, that is, elastic displacement, plastic displacement, cutting, destruction of surface films and destruction of bulk material. There are many types of wear mechanisms, but the most common wear mechanisms are: Abrasive wear (polishing, sourcing, scratching, grinding, gouging), Adhesive wear (galling, scuffing, scoring), Corrosive wear (Chemical nature), Fatigue (Delamination).

- **Adhesive Wear**: Adhesive wear is very common in metals. It is heavily dependent on the mutual affinity between the materials. All theories which predict wear rates start from the concept of true area of contact. It is usually assumed that the true area of contact between two real metal surfaces is determined by the plastic deformation of their highest asperities. Severity of adhesive wear is based on the area of contact which is given by $(A_R) =$

N/H. Here, N is load applied to press one surface over other surface and H is hardness of soft material. This expression provides appropriate results, if whole load is supported due to plastic deformation of the surface. However, for elasto-plastic deformation, the expression needs to be slightly modified, $(A_R) = (\frac{A_R}{H})_n$ where $(2/3 > n > 1)$. Here, assumption is that higher asperities could be deformed plastically, while the lower contacting asperities are subject to stay within elastic limits. In addition, the adhesive wear will depend on the shear strength of friction junctions. This means total true area of contact consists of plastic and elastic asperity contacts, where shear strength of the contacting asperities influence the rate of adhesive wear [89]. As shown in the fig. 3.12(a), if the interface between two surfaces is generated by a plastic contact characterized by enough adhesive bonding strength to resist relative sliding, large plastic deformation caused by dislocation is introduced under compression (at entrance) and shearing (at exit). As a result of such large deformation in the contact region, cracking phenomena are generated by mechanically induced stresses and strains, and thus they propagate in the combined fracture mode of tensile and shearing. When the crack reaches the contact interface, wear particles are formed and adhesive transfer is completed.

- **Abrasive Wear:** Abrasive wear, sometimes called cutting wear, occurs when hard particles slide and roll under pressure, across the tooth surface. Hard particle sources are: dirt in the housing, sand or scale from castings, metal wear particles, and particles introduced into housing when filling with lube oil. Scratching is a form of abrasive wear, characterized by short scratch-like lines in the direction of sliding. This type of damage is usually light and can be stopped by removing the contaminants that caused it. fig. 3.13 shows abrasive wear of a hardened gear. Following are the well-known reasons of abrasive wear mechanisms: Micro-cutting: Sharp particle or hard asperity cuts the softer surface. Cut material is removed as wear debris. Micro-fracture: Generally, occurs in brittle, e.g. ceramic material. Fracture of the worn surface occurs due to merging of a number of smaller cracks. Micro fatigue: When a ductile material is abraded by a blunt particle/asperity, the worn surface is repeatedly loaded and unloaded, and failure occurs due to fatigue. Removal of material grains: Happens in materials (i.e. ceramics) having relatively week grain boundaries. In fig. 3.12(b), if the scenario is similar than previous one

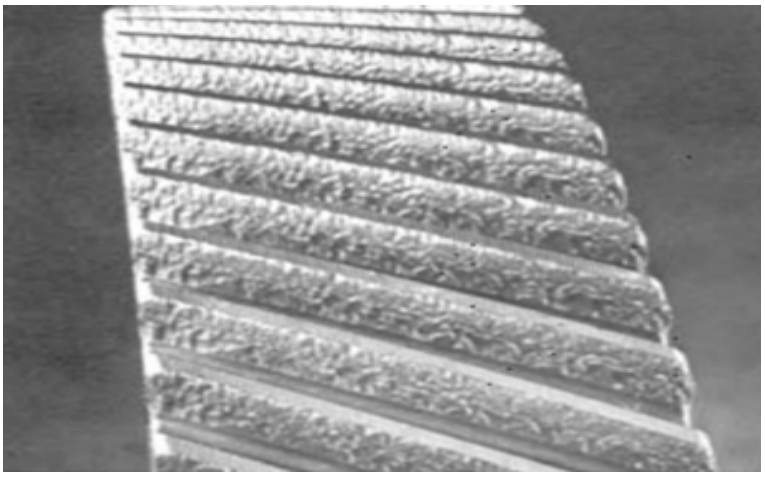

FIGURE 3.13: Abrasive wear of gear [12]

(adhesive wear), but the plastic contact occurs between hard and sharp or soft material, the harder penetrates to the softer one and an interlock takes place generating ploughing. A cut and scared groove is usually formed. In particular, when wearing material has ductile property, a ribbon-like long debris is generated by a sort of micro-cutting; while instead in the case of brittle material, wear particles are generated by crack propagation. Thus, in this context, hardness and stiffness properties of the two mating surfaces are extremely correlated to the wear behavior.

- **Fatigue Wear**: Fatigue is attributed to multiple reversals (apply and release) of the contact stress, occurring due to cyclic loading such as in rolling bearings, gears, friction drives, cam and follower. Abrasive and Adhesive wear involve a large contribution from fatigue. In fig. 3.12(c), it occurs after repeated friction cycles on both elastic and plastic contacts. Neither adhesive and abrasive mechanisms are involved: deformation, crack propagation, comparison of wear particles, and, in such cases, complete surface failure are stochastic consequences of prolonged running-in states of work generating a certain number of repeated contacts.

- **Corrosive wear**: The fundamental cause of Corrosive wear is a chemical reaction between the material and a corroding medium which can be either a chemical reagent, reactive lubricant or even air. Understanding the mechanisms of corrosive wear is important to reduce this kind of wear. The stages of

the corrosive wear: Firstly, the sliding surface chemically interact with environment (humid/industrial vapor/acid), which results in reaction product (like oxide, chloride), and it lead to wearing away of the reaction product film. In fig. 3.12(d), the material removal is not governed by mechanical interaction, but rather by the growth of chemical reactions (the most representative one is the oxidation, and in that case, it is not wrong to talk about oxidative wear). These are highly activated and accelerated by frictional deformation, frictional heating, micro-fracture and successive reaction products that in such cases end up in strongly adhere to the surfaces forming a reaction layer.

3.4 Lubrication

It is known since ages that oils and greases reduce the friction between sliding surfaces, by filling the surface cavities and making the surfaces smoother. Action of liquids/greases is known as lubrication. In other words, lubrication is a process by which the friction and wear rates in a moving contact are reduced by using suitable lubricant. As da Vinci observed about five centuries ago, "all things and anything whatsoever, however thin be, which is in the middle between objects that rub together lighten the difficulty of friction" [11]. Lubricant is a substance introduced between relatively moving parts to reduce friction (μ = 0.1 to 0.0001) and wear rate. The progress in scientific research indicated that reduction in friction occurs due to decrease in adhesion component compared to abrasion component of friction. Almost every relatively moving component in an assembly requires lubricant Lubricants are often classified as "Newtonian and "Non-Newtonian" fluids. This classification is on basis of relation between shear stress and shear strain rate (fig. 3.14). For Newtonian fluid, shear stress is given by

$$\tau = \eta\phi = \eta\frac{dx}{dy} = \eta\frac{du}{dy}, \tag{3.7}$$

In this relation, η is known as dynamic viscosity, which is one of the important lubrication parameters. Method of replenishing lubricant decides overall performance of the system. Lubricant thickness between two solid surfaces must be thick to avoid wear, but thin enough to minimize lubricant shearing. In other words, lubrication

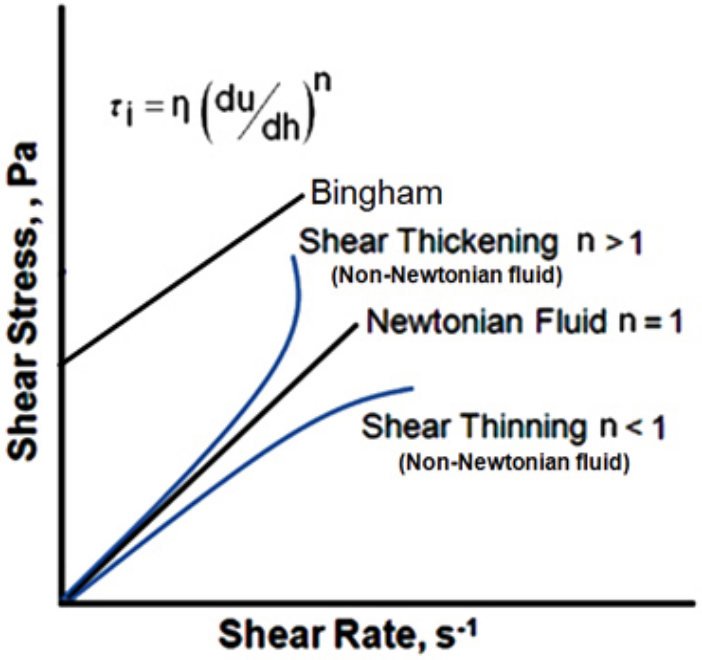

FIGURE 3.14: Newtonian and non-Newtonian fluid

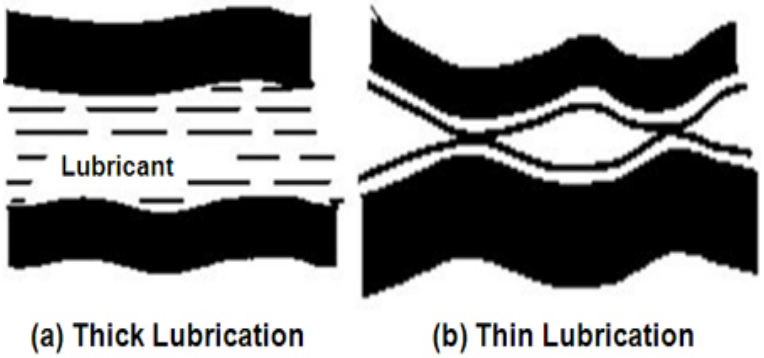

FIGURE 3.15: Fluid film lubrication

can be thick or thin based on the application. Thick & Thin Lubrications (fig. 3.15): Thick lubrication is governed by Reynolds theory. Thick lubrication is not advantageous because lesser the quantity of oil gives the lesser friction. Thin lubrication is far more complex. Requires scientific study at nano- to micro- level. From friction point of view, it is advantageous than thick lubrication

3.4.1 Lubrication mechanisms:

Although fluid film lubrication relies heavily on fluid mechanics and kinematics, yet it is still ultimately a problem of two surfaces that are either in partial-contact or separated by a thin fluid film. Further, Reynolds equation that governs fluid film lubrication is based on the assumption of thin film. Therefore, it is necessary to understand the importance of these lubrication mechanisms relative to the surface texture of tribo-pair. A dimensionless film parameter Λ (often referred as "specific film thickness") is used to classify four lubricant regimes.

$$\Lambda = \frac{h_{min}}{\sqrt{R_{rms,a}^2 + R_{rms,b}^2}}, \tag{3.8}$$

$R_{rms,a}$ is root mean square (rms) surface roughness of surface a, and $R_{rms,b}$ is rms surface roughness of surface b. Interestingly here rms value is used, while generally arithmetic avg. roughness is used. To clarify this, let us examine fig. 3.16 [13]. From tribological point of view, a surface without any asperity but with a number of valleys (that retains lubricants and provide a room for debris collection) is always preferred. Measurement of average roughness imposes a linear penalty on all points whether a point is too close to nominal line or too far. However, rms roughness parameter uses square term. Imagine, if there are three points: A one unit, B two units and C three units away from nominal line, RMS roughness parameter put penalty of one, four and nine on points A, B, C respectively. Therefore, rms value is a better roughness parameter compared to average roughness. Based on the value of dimensionless film parameter(Λ), Eq. (3.6) lubrication mechanisms are classified as follows: Boundary lubrication ($\Lambda < 1$), Hydrodynamic lubrication ($\Lambda > 5$), Mixed lubrication ($1 < \Lambda < 3$), Elastohydrodynamic ($3 < \Lambda < 5$). Peak surface roughness is generally two to three times of the rms surface roughness. Therefore, $\Lambda > 1$ does not indicate the clear separation between tribo-pair. This is a main reason to keep film parameter lesser than 3 but greater than 1 to identify mixed lubrication mechanism. To avoid any wear and minimize friction, a complete separation, between asperities of two relative moving surfaces is essential. This requires film parameter more than 3. Film parameter depends on film thickness and composite surface roughness of tribo-pair. Often foreign particles or wear debris change the hydrodynamic/elastohydrodynamic lubrication to mixed or boundary lubrication mechanism, as shown in fig. 3.17.

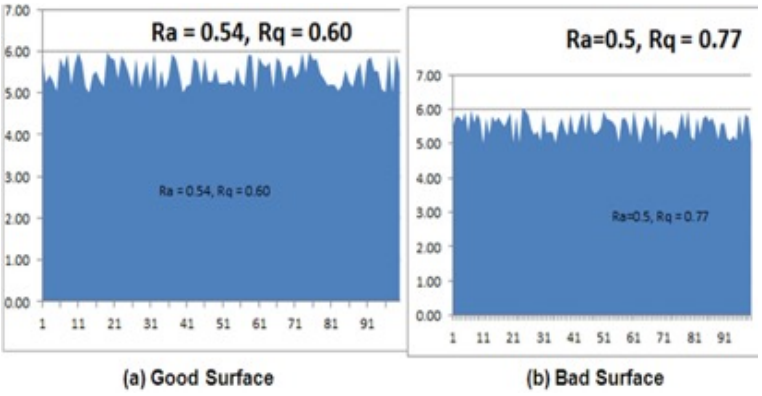

FIGURE 3.16: Comparison between average and root mean square roughness [12, 13]

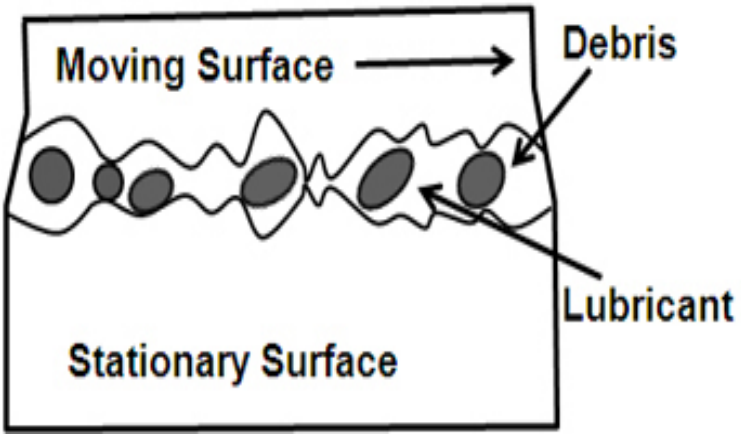

FIGURE 3.17: Foreign particles/wear debris shift hydrodynamic/elastohydrodynamic lubrication in boundary/mixed lubrication [13]

3.4.2 Stribeck Curve:

The Stribeck curve is an overall view of friction variation in the entire range of lubrication, including the hydrodynamic, mixed, and boundary lubrication. By means of the Stribeck curve the transitions from boundary lubrication to mixed lubrication and the transitions from mixed lubrication to elasto-hydrodynamic lubrication can be predicted. Knowledge of the lubrication regimes in which our machines run is essential to choose the best viscosity and type of lubricant with the target to avoid wear and improve energy saving, that is why the Stribeck curve is needed. To choose the right viscosity for an application is of crucial importance to avoid wear in machines, for this we usually follow the manufacturer recommendations but rarely do

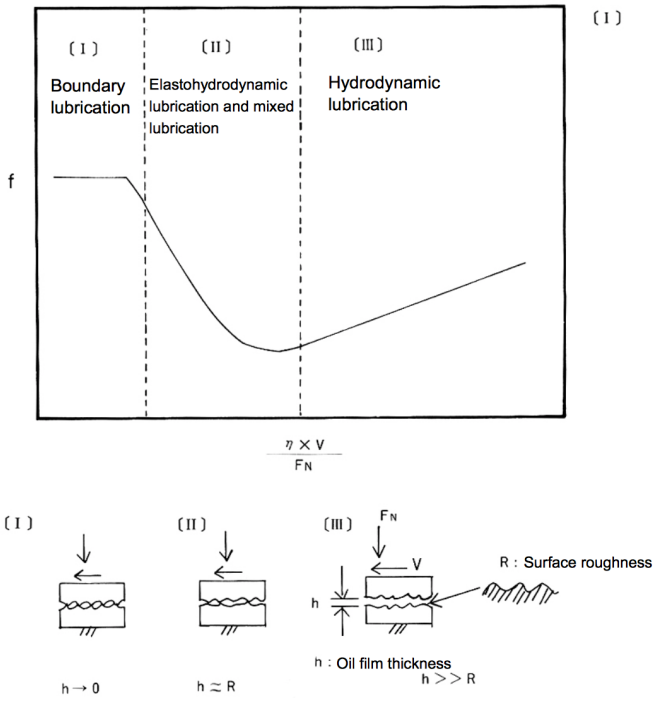

FIGURE 3.18: Stribeck curve and lubrication regions [14, 15]

we consider parameters as the surface relative speed or the real running temperature. If we are not sure usually we increase the ISO viscosity grade but this does not ensure the wear protection. The best way to solve this problem is to know the lubrication regime our machines run, that is why we need to know the Stribeck curve [13]. Described by Richard Stribeck during the first years of the 20th century, this curve provides us an idea of the friction coefficient variation between two surfaces in function of the lubrication regime. This regime depends on a parameter related with the lubricant viscosity, the surfaces relative speed and the load. If we follow the abscissa axis, first we find the boundary lubrication regime in which the friction coefficient is too high due the film is too thin, lower than the surface roughness, so we cannot avoid the wear. If we cannot avoid running in this regime, due the running temperature, very low relative speed and/or very high load, we must use solid lubricants and pastes. Other option is to increase the lubricant viscosity to move to the next lubrication regime [14].

In the mixed lubrication regime, the film thickness is higher, around the surface

roughness, so only there are isolated contacts. This regime provides a drastic friction coefficient decrease and we can find a curve minimum, it means is the suitable for energy saving. To avoid wear to use anti-wear additives is needed. Both regimes are considered unstable because the increase of temperature reduces the viscosity and increases the friction, as a result of that the lubrication regime moves to the left of the curve, the area that generates more wear. If we increase the viscosity or the relative speed we move to the elastohydrodynamic and hydrodynamic regimes, where we avoid wear because the film thickness is higher than the roughness. In the elastohydrodynamic regime, Hertzian contacts are found due to very small contact surface and very high load, up to 3.0 GPa, that increase the viscosity of the lubricant, deform both surfaces and reduce the roughness. This lubrication regime is near the minimum of the Stribeck curve, in fact some authors think the minimum is in this regime, so to keep in this regime the energy saving increases and reduces wear. Gears, bearings and cams run in this regime.

In the hydrodynamic regime, the film thickness is much higher than the roughness, due the relative speed and the viscosity of the lubricant, this is why we avoid the contacts between the surfaces and eliminate wear. This regime is defined by the Reynolds equation. But the Stribeck curve indicates us that this regime friction coefficient increase due to fluid drag with an increase in the speed, so the energy saving gets worse, mainly if the relative speed between the surfaces is too high, in this case we must reduce the viscosity of the lubricant to move closer to the minimum of the Stribeck curve. Journal bearings run in this regime. We can consider these regimes as stables because any variation of temperature produces a variation of the viscosity and the friction coefficient in the same direction so they stabilize themselves [5].

3.5 Fluid Film Lubrication:

Fluid is defined as a substance that easily moves and changes its relative position without a separation from the bulk mass. Fluid includes all gases, liquids and easy flowing solids. Film means an exceedingly thin layer or a thin covering. Lubrication

makes relative motion between two surfaces very smooth. It reduces the friction and minimizes the wear. In normal conditions, real area of contact between tribo-pair is hardly ten percent of apparent area. With such low contact area, stress-state always exceeds the elastic/fracture point of all known solids. It results in high plastic deformation in ductile materials, while it generates cracks in brittle materials. In such a condition, relative motion between surfaces causes excessive wear. Therefore, it is essential to reduce the severity of normal stresses imposed by applied load and to reduce the shear stresses induced due to relative motion. fig. 3.19 highlights few possible methods to achieve the reduction in normal and shear stresses. The first two concepts are useful for few degree oscillations. Continuous relative motion such as rotational motion requires solid lubricants, boundary lubricants, rolling elements and associate lubricants, pressurized (hydrostatic, aerostatic, hydrodynamic, aerodynamic) lubrication or magnetic/electric field. Electric or Magnetic field is a very good solution, but requires gigantic dimensions to compete with any mechanism of fluid film lubrication (FFL). In fluid film lubrication regime, the sliding surfaces are completely separated by a film of liquid or gaseous lubricant. Hydrodynamic lubrication film was formed due to the converging wedge shaped geometry (shown in fig. 3.20, and the squeeze film are formed with variation in load or speed variations. In both cases the viscosity of lubricant play an important role to support the load (shown in fig. 3.21).

Every mechanism of fluid film lubrication is suitable for a particular set of operating and environmental condition. Further, if applied load is reduced, the film thickness (separation between tribo-pair) will increase. Similarly, if more load is added to the moving surface, the film thickness will decrease. If a load greater than design load is applied the tribo-surface will not be able separated. To reduce this sensitivity feed-back control system is used, which increases the cost of overall system. To compensate cost, often a hybrid concept of hydrodynamic + hydrostatic or aerodynamic + aerostatic is used to achieve best of both the mechanisms of fluid film lubrications. In a hydrodynamic lubrication mechanism, a fluid is drawn into the region between the relatively-moving surface by the virtue of its viscosity and adhesion to the surfaces; and due to the converging geometry of the surfaces (as shown in fig. 3.20) a pressure is generated within the fluid that separates the tribo-surfaces.

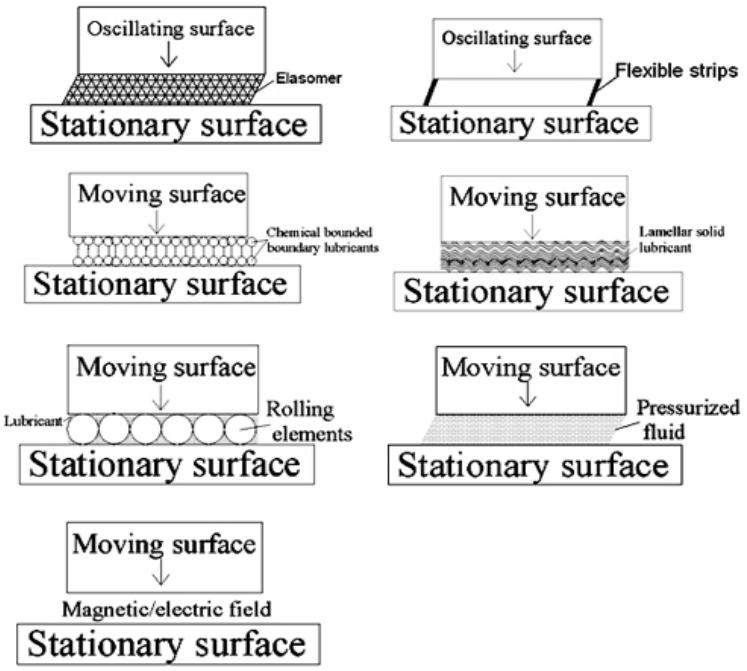

FIGURE 3.19: Various concepts to separate two solid surfaces [15]

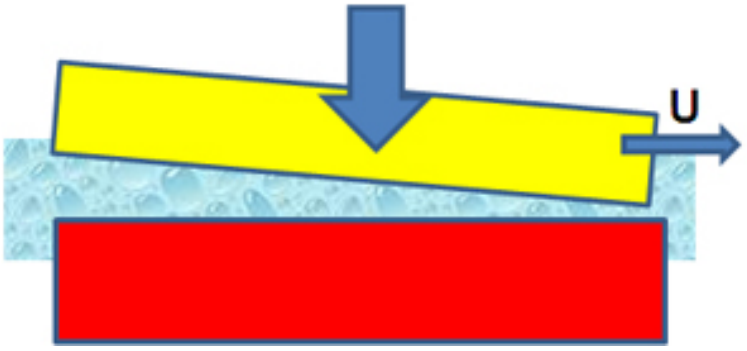

FIGURE 3.20: Converging wedge shape geometry

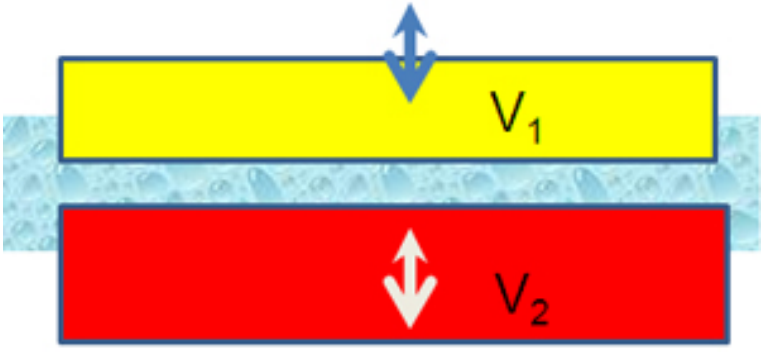

FIGURE 3.21: Squeeze lubrication

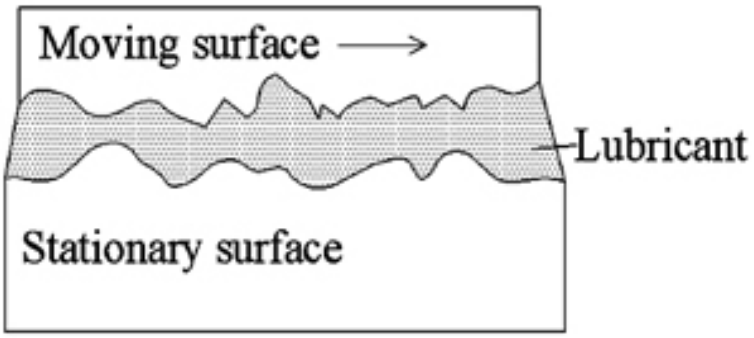

FIGURE 3.22: Hydrodynamic lubrication

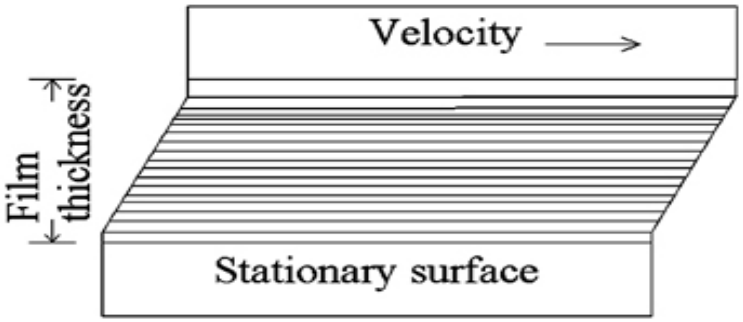

FIGURE 3.23: Shearing of lubricant

The separating film is only generated when there is relative motion. Higher the relative velocity thicker is the lubricant layer. This lubrication mechanism is referred as "the ideal form of lubrication", since solid surfaces are prevented from coming into contact (as shown in fig. 3.22, where two surfaces are completely separated) that provides high resistance to wear and low friction. Another well-known mechanism that always occurs at the start/stop of tribo-pair is boundary lubrication. This lubrication mechanism assumes (as shown in fig. 3.24) almost negligible separation between tribo-surfaces that occurs at high load and very low speed. In such cases, the working fluid between tribo-pairs adheres to or "wets" the surfaces, and carries a fraction of imposed load. The physical and chemical properties of thin molecular films and the surfaces to which they are attached determine the overall tribological behavior. The friction and wear, in the case of boundary lubrication, are much higher compared to those in full film lubrication. That is why hybrid concept of hydrostatic operation at start and hydrodynamic operation at running conditions came into existence. Third important fluid film lubrication mechanism is mixed lubrication which assumes (as shown in fig. 3.25) solid contact between some

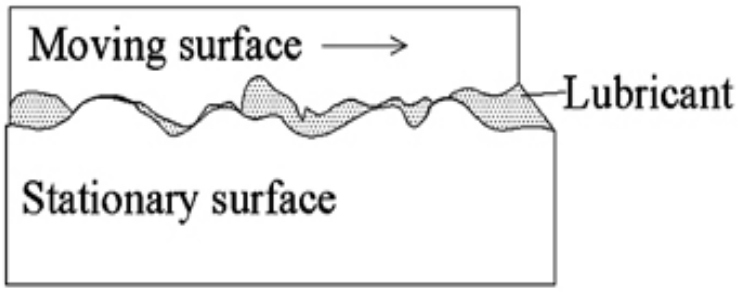

FIGURE 3.24: Boundary lubrication

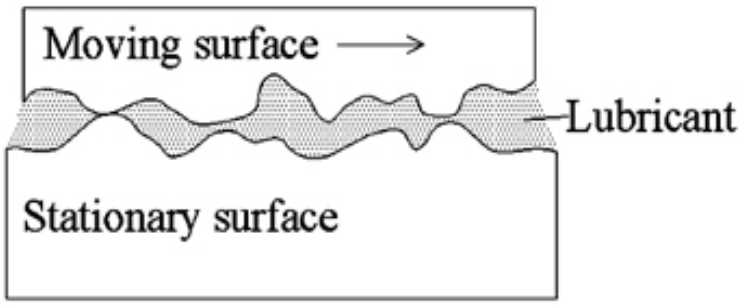

FIGURE 3.25: Mixed lubrication

asperities of tribo-pairs, while rest of the area covered by lubricant. The lubrication mechanism in this regime is governed by a combination of boundary and hydrodynamic lubrication. Interaction takes place between one or more molecular layers of boundary lubricating film.

Lowest friction producing fluid film lubrication mechanism is Elasto-Hydrodynamic Lubrication (EHL). EHL mostly occurs in rolling element bearings, gears, cam-follower contact. As the name suggests this lubrication mechanism utilizes: (1) elastic deformation, and (2) hydrodynamics. Relative velocity between tribo-pair develops hydrodynamic action. Excessive load or relatively soft surface results in elastic deformation of surface(s). In case of excessive load, generated fluid pressure is very high and the surfaces deform elastically. As lubricant viscosity is a strong function of pressure, particularly at high pressure, lubricant-viscosity may rise (as much as 10 orders of magnitude) considerably, and this further assists the formation of an effective lubrication. EHL analysis involves an iterative procedure to establish compatibility between hydrodynamic pressure developed by relative motion and separation between tribo-pair caused by this pressure. Simplest way to analyze EHL

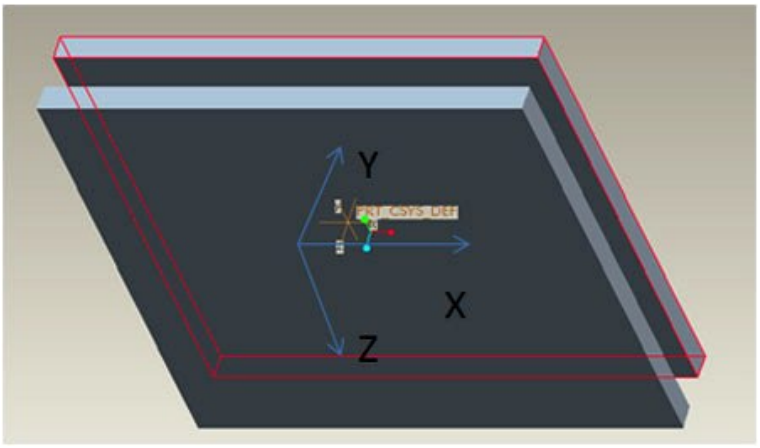

FIGURE 3.26: Fluid film lubrication between two plates [82,83,61]

FIGURE 3.27: Lubrication

is by making assumption of film thickness using hydrodynamic equations, evaluate elastic deformation of surfaces, modify film thickness and iterate. The iteration continues until the modified film thickness distribution matches with the new film thickness distribution.

In 1886, Reynolds derived an equation for estimation of pressure distribution for "Fluid Film Lubrication". Quantification of fluid film lubrication can be made by solving Reynolds' Equation, which provides fluid film pressure as a function of coordinates and time. Reynolds equation helps to predict hydrodynamic, squeeze, and hydrostatic film mechanisms [15].

- For liquid lubricant under isothermal conditions:

$$\frac{\partial}{\partial x}\left(\frac{h^3}{\eta}\frac{\partial P}{\partial x}\right)+\frac{\partial}{\partial z}\left(\frac{h^3}{\eta}\frac{\partial P}{\partial z}\right) = 6\left[\frac{\partial}{\partial x}(U_1+U_2)h+\frac{\partial}{\partial z}(U_1+U_2)h+ 2\left(\left(w_h-U_1\frac{\partial h}{\partial x}-U_2\frac{\partial h}{\partial z}\right)-w_0\right)\right] \quad (3.9)$$

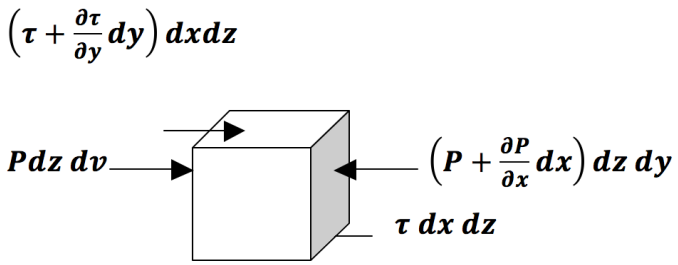

FIGURE 3.28: Fluid element subjected to pressure & viscous forces [14]

for geometry shown in fig. 2.26, fig 2.27.

- For hydrostatic case this equation will be reduced to:

$$\frac{\partial}{\partial x}\left(\frac{h^3}{\eta}\frac{\partial P}{\partial x}\right) + \frac{\partial}{\partial z}\left(\frac{h^3}{\eta}\frac{\partial P}{\partial z}\right) = 0, \tag{3.10}$$

- For hydrodynamic case this equation will be reduced to:

$$\frac{\partial}{\partial x}\left(\frac{h^3}{\eta}\frac{\partial P}{\partial x}\right) + \frac{\partial}{\partial z}\left(\frac{h^3}{\eta}\frac{\partial P}{\partial z}\right) = 6\left[\frac{\partial}{\partial x}(U_2 - U_1)h + \frac{\partial}{\partial z}(W_2 - W_1)h\right] \tag{3.11}$$

- For squeeze film case this equation will be reduced to:

$$\frac{\partial}{\partial x}\left(\frac{h^3}{\eta}\frac{\partial P}{\partial x}\right) + \frac{\partial}{\partial z}\left(\frac{h^3}{\eta}\frac{\partial P}{\partial z}\right) = 12(V_h - V_0). \tag{3.12}$$

3.6 Derivation of Reynold's equation

To model the pressure as a function of angle of inclination, let us consider a fluid element subjected to pressure and viscous forces, assuming gravity and inertia forces (as shown in fig. 3.28) acting on fluid element can be neglected. On balancing forces

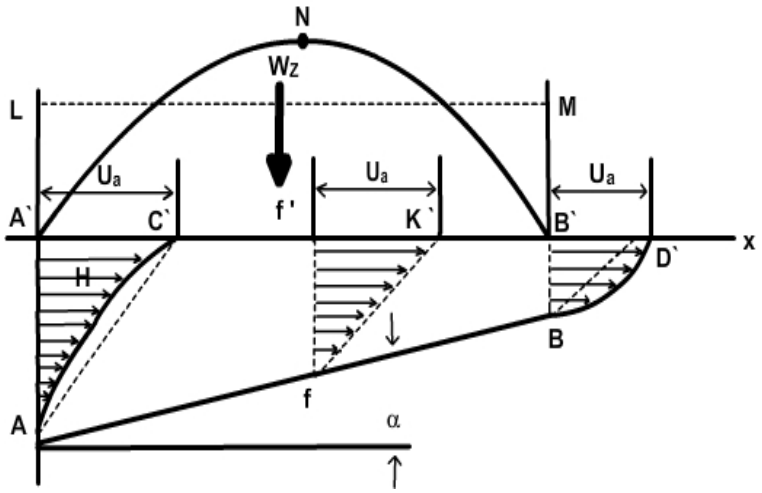

FIGURE 3.29: Development of fluid pressure in relatively moving inclined plates [14]

shown in fig. 3.28,

$$\begin{aligned} pdydz + (\tau + \frac{\partial \tau}{\partial y}dy)dxdz = (p + \frac{\partial p}{\partial x}dx)dydz + \tau dx &= \left(\frac{\partial \tau}{\partial y} - \frac{\partial p}{\partial x}\right)dxdydz = 0, \\ \frac{\partial \tau}{\partial y} &= \frac{\partial p}{\partial x} \end{aligned} \tag{3.13}$$

For laminar flow of Newtonian fluid,

$$\begin{aligned} \tau &= \eta\frac{\partial u}{\partial y}, \\ \frac{\partial}{\partial y}\left(\eta\frac{\partial u}{\partial y}\right) &= \frac{\partial p}{\partial x}. \end{aligned} \tag{3.14}$$

On substitution, Equation (3.14) is based on the following assumptions: Negligible inertia terms, Negligible pressure gradient in the direction of film thickness, Newtonian fluid. By assuming constant value of viscosity:

$$\frac{\partial P}{\partial x} = \eta\frac{\partial^2 u}{\partial y^2}. \tag{3.15}$$

Similarly, on force balance in z direction:

$$\frac{\partial P}{\partial z} = \eta\frac{\partial^2 w}{\partial y^2}. \tag{3.16}$$

FIGURE 3.30: Velocities of plates

To find flow velocity (u) in x- direction, integrate $\frac{\partial P}{\partial x} = \eta \frac{\partial^2 u}{\partial y^2}$ two times. On integrating first time

$$\eta \frac{\partial u}{\partial y} = \frac{\partial P}{\partial x} + C_1. \tag{3.17}$$

On integrating second time

$$\eta u = \frac{\partial P}{\partial x} \frac{y^2}{2} + C_1 y + C_2. \tag{3.18}$$

Assuming no slip at liquid-solid boundary;

$$\begin{aligned} y = 0, u &= U_2, \\ y = h, u &= U_1. \end{aligned} \tag{3.19}$$

Utilizing these boundary conditions, values of integration constants can be evaluated.

$$\begin{aligned} \eta U_2 &= C_2, \\ \frac{\eta(U_1 - U_2}{h} - \frac{\partial P}{\partial x} \frac{h}{2} &= C_1. \end{aligned} \tag{3.20}$$

On substituting C_1 and C_2

$$u = \left(\frac{y^2 - yh}{2\eta} \right) \frac{\partial P}{\partial x} + (U_1 - U_2) \frac{y}{h} + U_2. \tag{3.21}$$

Equation (3.21) is applicable in the case of following assumptions: Negligible inertia terms, Negligible pressure gradient in the direction of film thickness, Newtonian fluid, Constant value of viscosity, No slip at liquid solid boundary. In Eq. (3.21) on right hand side there are three terms, two velocity terms and one pressure term. Velocity terms represent "shear flow" also known as "Couette flow". Flow due to pressure gradient is termed as "Poiseuille flow"

$$w = \left(\frac{y^2 - yh}{2\eta} \right) \frac{\partial P}{\partial z} + (W_1 - W_2) \frac{y}{h} + W_2. \tag{3.22}$$

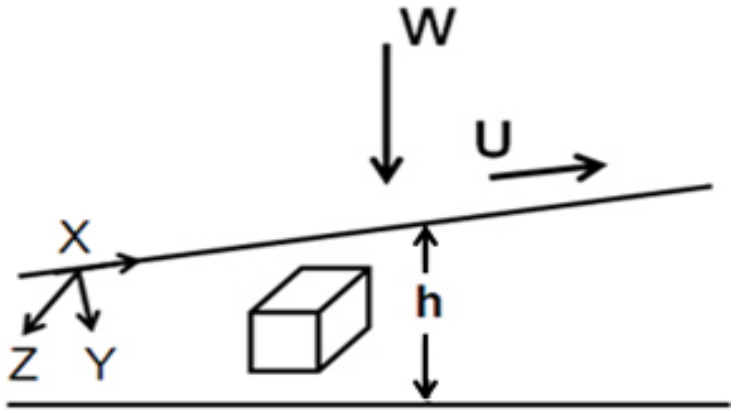

FIGURE 3.31: Inclined plates with fluid element and coordinate system [15]

The Poiseuille flow term retards the fluid flow at entrance. This pressure term boosts flow at exit as indicated in Fig. 3.29. In this figure ua = U1 - U2. To derive the Reynolds equation, Eq. (3.21 and 3.22) must be coupled with continuity equation. Continuity equation for incompressible fluid can be expressed as:

$$\frac{\partial u}{\partial x} + \frac{\partial v}{\partial y} + \frac{\partial w}{\partial z} = 0 \tag{3.23}$$

Integrating above equation in y-direction from y = 0 to y = h and using Leibnitz rule, we get

$$\frac{\partial}{\partial x}\left(\frac{h^3}{12\eta}\frac{\partial P}{\partial x}\right) + \frac{\partial}{\partial z}\left(\frac{h^3}{12\eta}\frac{\partial P}{\partial z}\right) = \frac{1}{2}\frac{\partial}{\partial x}\Big(U_1 - U_2\Big)h + (V_h - V_0) + \frac{1}{2}\frac{\partial}{\partial z}\Big(W_2 - W_1\Big)h \tag{3.24}$$

3.6.1 Effect of Cavitation on Friction during lubricated contact

Cavitation is the formation of empty cavities in a liquid, followed by their immediate and sudden implosion. The primary causes for their formation include vaporization at low pressure, air ingestion, flow turbulence, and internal re-circulation. The vaporization itself does not cause the damage - the damage happens when the vapour almost immediately after evaporation collapses when velocity decreases and pressure increases. In other words, cavitation bubbles are formed in locations where the

pressure in the liquid become lower than a critical value. If a pressure drop occurs because of the high velocities of a liquid, then the cavitation is called hydrodynamic. Cavitation phenomena play an important role and influence contact performance. Particularly, an appropriate value of pcav (cavitation Pressure or pressure in the cavity) and the ratio of cavitation pressure over supply pressure is crucial. Furthermore, cavitation should be taken into account in a mass-conserving way, when performing numerical simulations [90]. Optimal texturing parameters are generally independent of speed and viscosity. However, changes in these values may result in the occurrence of cavitation, which can ultimately change optimal texturing parameters. In the study of textured or rough surfaces cavitation may occur not only globally in divergent contact areas, but also locally inside of individual dimples or in-between asperities (micro-cavitation). As rupture and reformation of the lubricant film may occur multiple times, a mass-conservative treatment of cavitation has been shown to be crucial for accurate performance predictions [91].

Cavitation may also occur at the microhole location, indeed it has been found in particular conditions that almost half of the microholes are affected by cavitation and half, instead, may be affected if the pressure increase is not enough to prevent cavitation from taking place. Therefore, let us discuss what would be expected in terms of friction if cavitation takes place as the hole's depth is increased. Assume that, after a decrease of friction due to a small increase of h(depth), as soon as the microhole depth reaches the value of h $\frac{1}{4}$ hopt (optimal depth) cavitation takes place in the microhole [53]. When this happens, the local tangential stress will be further reduced because the very low viscosity of vapour makes the local tangential stress almost vanish at the microhole location. In order to explain the increase of friction above hopt one should admit that, when hopt is exceeded micro-cavitation should disappear leading to a new increase of the local tangential stress. The pressure increase at the cavity trailing edge [54], observed for different lubricant viscosities, which gives a net positive pressure, as well as the formation of the vortex inside the cavity, are responsible for the shear force and the increase of friction. The results of the simulation indicate that the larger vortex inside the cavity, obtained by the deeper and square-shaped dimples, and the proper pressure distribution over the cavity would result in larger gains in terms of shear-force reduction.

The occurrence of cavitation inside individual dimples was also shown experimentally by Qiu and Khonsari [92] and Zhang and Meng [93], using high speed cameras. Pressure distributions over a single micro-dimple texture can be described in three different cases: (i) cavitation does not occur (pcav or psup), (ii) predicted by a non-mass-conserving cavitation algorithm for pcav or psup and (iii) predicted by a mass- conserving cavitation algorithm for pcav o psup(supply pressure) . Note, however, that load is only generated in certain cases, as the positive pressures are also influenced. In some cases, the load support may even become negative, depending on the shape of the asymmetric pressure distribution. Additionally, lift can only be generated when the cavitation pressure is inferior to the supply pressure, as this will provide the necessary pressure gradient to ensure a sufficient lubricant supply (inlet suction [94, 95]. If cavitation and supply pressure are equal this pressure gradient does not occur, leading to starvation in the dimple, hence, no pressure can build up. If the supply pressure is much higher than the cavitation pressure, cavitation will not occur at all. In this case the pressure distribution over a single texture is antisymmetric and no lift can be generated either. It was experimentally observed that at low speeds no cavitation occurs in the dimples, but at higher speeds the gaseous and vapor cavitation occurs. Thus, cavitation pressure and therefore ultimately load carrying capacity is highly affected by the operational speed. Unlike the untextured specimens, which only showed minor scratches, the textured samples showed significant surface damage after conducting experiments [29]. However, their coefficient of friction (COF) was considerably lower during all tests performed. It was further found that for a given dimple diameter to depth ratio λ, a higher texture density leads to higher friction reduction and for a given density of texture dimples an optimal texture value for λ exists.

Chapter 4

MATERIALS AND EQUIPMENT

4.1 Introduction

A description of the setups and procedures used to carry out the various fabrications and characterization studies is presented in this chapter. This chapter introduces the materials that were investigated, the laser equipment and surface analysis instruments used. Two main materials were investigated, these are 100 Cr6 steel and Stainless steel polished. The femtosecond laser machining is described in terms of its setup and operational parameters. The modes of operation of the laser and of obtaining the laser pulses are described. The surface morphology analysis instruments used in the research included optical microscope, Scanning Electron Microscope, and Confocal Microscope. The Tribological characterization was performed by three different tribometers, pin-on-disk High temperature, Rheometer and Plint off tribometer. There are other material surface characterization instruments used in the research which are introduced in specific chapters when used.

4.2 Materials- Stainless steel

Stainless steel is an iron-based alloy with a significant chromium content; in many cases, together with chromium, other special chemical elements are intentionally added, such as nickel and molybdenum. The main characteristics of the Martenistic

and Austenitic steel is resistance to wet corrosion, or electrochemical corrosion, in aggressive environments such as fresh water, sea water, contaminated water based solutions, acid and base environments, industrial environments, etc. Another important characteristic of Martenistic and Austenitic steel is the resistance to oxidation at high temperatures, or chemical corrosion, as typically occurs in hot process gases. The typical fields of application for stainless steel are those in the chemical industry, oil industry, foodstuffs and paper manufacturing, the pharmaceutical, biomedical and transport sectors, in off-shore structures, household appliances, and the construction and urban furnishing sectors [96].

In accordance with the European standard EN 10088, steel is classed as stainless when its chemical composition has a minimum chromium content of 10.5%. However, it should be noted that in virtually all types of stainless steel available on the market, the chromium content is much greater than this value, normally ranging, in the most common cases, from 13% to 18%: this is due to the fact that in practice, a chromium content of at least 12% is needed to obtain satisfactory resistance to corrosion in water based solutions [97]. The presence of chromium alloy ensures the possibility of creating a very thin layer of oxide (also known as passive layer) on the steel surface, mainly made up of chromium oxides and hydroxides. This film is insoluble, compact and adheres well to the substrate thereby protecting the material on which it is formed. The film of chromium oxide/hydroxide is extremely thin – just a few nanometres – and transparent to luminous radiation, and therefore gives stainless steel its typical grey-silver metal finish, as clearly seen in cooking utensils, pans, cutlery and metal watch straps. All the above properties are the consequence of the rapid reaction of the chromium alloy with oxygen in the atmosphere. The four steel grades described above, belonging to various levels of the tree structure of stainless steels illustrated in fig. 4.1, also represent the four main families of stainless steels currently used; these families, all defined on the basis of their microstructure at ambient temperature, are:

1. Martensitic stainless steel (such as X30Cr13)
2. Ferritic stainless steel (such as X6Cr17)
3. Austenitic stainless steel (such as X5CrNi18-10 and X5CrNiMo17-12-2),

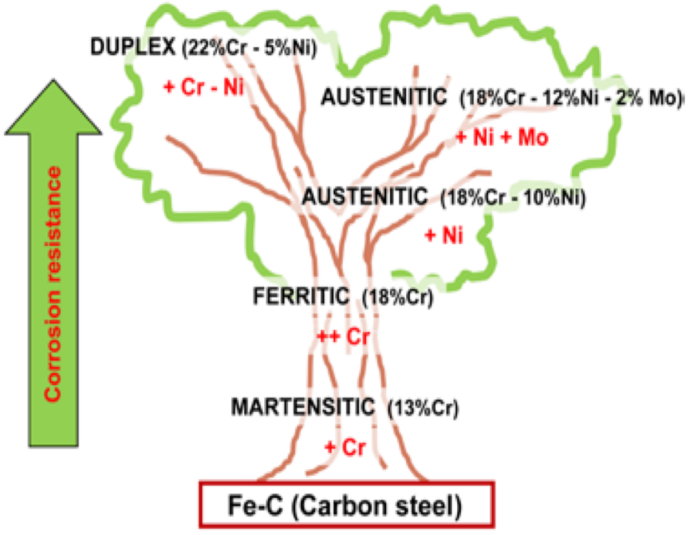

FIGURE 4.1: Schematic of the evolution of stainless steels starting from plain carbon steels: the stainless-steel tree structure [16, 17]

4. Austen-Ferritic, two-phase or duplex stainless steel (such as X2CrNiMoN22-5-3).

4.2.1 Used Materials

In the following sections, the main chemical and physical properties of the two materials used in this thesis are briefly presented. In both cases, the experiments were performed in ambient air without any gas shielding and no chemical pretreatments were carried out before the experiments. The metallic samples used in this thesis were Chrome steel 100 Cr6 and stainless steel (1.4112) (martensitic).

1. Chrome Steel 100 Cr6
2. Stainless steel (1.4112)

Quality	**100Cr6**	*Technical card*
According to standards	**EN ISO 683-17: 1999**	*Lucefin Group*
Number	**1.3505**	

Chemical composition

C%	Si%	Mn%	P% max	S% max	Cr%	Mo% max	Al% max	Cu% max
0,93-1,05	0,15-0,35	0,25-0,45	0,025	0,015	1,35-1,60	0,10	0,050	0,30
± 0.03	± 0.03	± 0.04	+ 0.005	+ 0.005	± 0.05	± 0.03	+ 0.010	+0.03

Product deviations are allowed

Temperature °C

Hot-forming	Quenching 1)	Quenching 2)	Tempering 1) 2)	Stress relief annealing 3)
1050-900	heating up to 650, pause, then 800-830 water	830-870 oil/ polymer salt bath 500-550 salt bath 180-200	150-300 air	600-650 furnace cooling

3) stress relief annealing is suggested to be carried out after machining and before final heat treatment

Isorhermal annealing +I	Spheroidized annealing +AC	Recrystallization annealing	Pre-heating welding	Stress-relieving after welding
800 rapid cooling to 720, pause, then air (HB max 210)	720-750 cooling 10 °C/h to 650, pause, then 40 °/h to 300, then air (HB max 220)	750-760 furnace cooling to 300, then air	not recommended	

Ac1	Acm	Ms	Mf
755	850	300	85

Hardness in the globular annealed and cold-worked state (hot rolled +AC+C) can be HB 240

Mechanical and physical properties

Table of tempering values obtained at room temperature on round of Ø 10 mm after quenching at 840 °C in oil

HV 30	832	800	772	746	674	633	577	528	471	434
HRC	65	64	63	62	59	57	54	51	47	44
R N/mm²			2400	2500	2420	2300	2100	1900	1650	1410
Tempering **°C**	**100**	**150**	**200**	**250**	**300**	**350**	**400**	**450**	**500**	

Hardening depth from surface to core (**0**) on round tempered at 850 °C in oil. Hardness values expressed in *HRC*

mm	20	15	10	5	**0**	5	10	15	20
Ø 20			*65*	*64*	*64*	*64*	*65*		
Ø 30		*64*	*62*	*59*	*58*	*59*	*62*	*64*	
Ø 40	*62*	*57*	*52*	*50.5*	*50*	*50.5*	*52*	*57*	*62*

Evolution of the austenitic **grain size** as a function of the material heating temperature

Grain size	8 - 9	7- 8	7	6	4 - 5	4
Temperature °C	830	850	900	950	1000	1050

Thermal expansion	$10^{-6} \cdot K^{-1}$	►	11.4						14.7
Modulus of elasticity	longitudinal GPa	210							
Modulus of elasticity	tangential GPa	80							
Bulk Modulus	GPa	140							
Poisson number	*v*	0.30							
Test at **°C**		**20**	**100**	**200**	**300**	**400**	**500**	**700**	

The symbol ► indicates temperature between 20 °C and 100 °C, 20 °C and 700 °C .....

Data under fatigue with low cycle number. Values for quenched and tempered material

Cyclic yield strength, σ_y' MPa	Cyclic strength exponent, **n'**	Cyclic strength coefficient, **K** ', MPa	Fatigue strength coefficient, σ_f ', MPa	Fatigue strength exponent, **b**
1324	0,15	3403	2642	- 0,09

Specific heat J/(Kg•K)	Density Kg/dm³	Thermal conductivity W/(m•K)	Electrical resistivity Ohm•mm²/m	Electrical conductivity Siemens•m/mm²
475	7.81	46.6	0.22	4.55

EUROPE EN	ITALY UNI	CHINA GB	GERMANY DIN	FRANCE AFNOR	U.K. B.S.	RUSSIA GOST	USA AISI/SAE
100Cr6	100Cr6	GCr15	1.3505	100C6		9Ch1	52100

FIGURE 4.2: Characteristics of the 100 Cr6 steel balls used [18]

Quality	**X90CrMoV18**	**Martensitic Stainless Steel**
Number	**1.4112**	

TECHNICAL CARD
GRUPPO LUCEFIN
REVISION 2012

Chemical composition

C%	Si% max	Mn% max	P% max	S% a) max	Cr%	Mo%	V%	
0,85-0,95	1,00	1,00	0,040	0,015	17,0-19,0	0,90-1,30	0,07-0,12	EN 10088-1: 2005
± 0.03	+ 0.05	+ 0.03	+ 0.005	+ 0.003	± 0.2	± 0.05	± 0.03	

Product deviations are allowed

a) for improving machinability, it is allowed a controlled sulphur content of 0,015 % - 0,030 %; for polishability, it is suggested a controlled sulphur content of max 0,015 %

Temperature °C

Melting range	**Hot-forming**	**Full annealing**	**Soft annealing +A**
1440-1420	1100-900	910-890 cooling 15 °C/h to 590, then air	840-780 slow cooling
Isothermal annealing +I	**Quenching +Q**	**Tempering +T**	**Stress-relieving +SR**
900-840 controlled cooling to 690, then air	1050-1000 oil / polymer (HRC 58)	550-450 air	350-100 air

MMA **welding** – AWS electrodes

pre-heating	*annealing after w.*
200-150	750-700

joint with steel

carbon	CrMo alloyed	stainless
E70 xx	E8018-B 2	E309 – E308

cosmetic welding
E309 special

Transformation temperature during heating **Ac1** ~ 790, **Ac3** ~ 870 and during cooling **Ms** ~ 280, **Mf** ~ 130

Mechanical properties

Hot-formed EN 10088-3: 2005 in conditions 1C, 1E, 1D, 1X, 1G, 2D

size		Testing at room temperature					
mm		**R**	**Rp** 0.2	**A%**	**Kv** +20 °C	**HB** a)	a) for information only
from	to	N/mm²	N/mm² min	min	J min	max	
	100					265	+A annealed material

Bars, typical values according to UNS S44003 steel 440B

size		Testing at room temperature									
mm		**R**	**Rp** 0.2	**A%**	**C%**	**HB**	**R**	**Rp** 0.2	**A%**	**C%**	**HB**
from	to	N/mm² min	N/mm² min	min	min	max	N/mm² min	N/mm² min	min	min	max
		738	427	18	35	269	827	655	9	20	285
		+A **hot-rolled** annealed					+A+C **cold-drawn**				

Forged (ASTM A 473-99 steel ASTM 440B)

size		Testing at room temperature					
mm		**R**	**Rp** 0.2	**A%**	**C%**	**Kv** +20 °C	**HB** a)
from	to	N/mm²	N/mm² min	min	min	J min	max
							269 +A annealed material

a) Only for guidance

Table of tempering values at room temperature after quenching at 1020 °C in oil

HB	595	560	543	525	525	371	311	279
HRC	57	55	54	53	53	40	33	29
Tempering **°C**	**100**	**200**	**300**	**400**	**500**	**600**	**650**	**700**

FIGURE 4.3: Characteristics of the stainless steel (1.4112)[18]

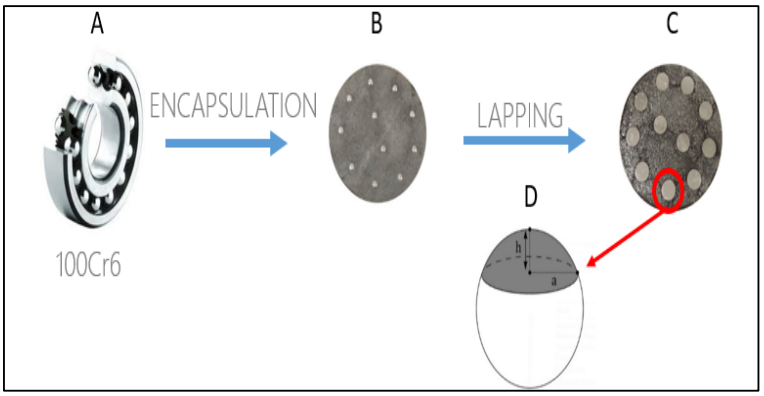

FIGURE 4.4: Sample Preparation

4.2.2 Sample Preparation

The micro surface texturing has been performed on polished stainless steel (1.4112) samples sent by Robert Bosch GmBh-Germany, and 100Cr6 steel spheres from commercial bearings fig. 4.4-A. The 100Cr6 spherical caps were firstly encapsulated in a resin cylinder (fig. 4.4-b) and then truncated by lapping (fig. 4.4-C) in order to obtain a flat circular surface with a diameter 2a of about 4 mm (fig. 4.4-D). Such flat surfaces correspond to our laboratory prototypes of bearing pads. Before being subjected to the laser surface texturing process, the samples were polished at a root-mean-square surface roughness of about 20 nm, as verified by atomic force microscopy.

Steps in the sample preparation: (A) 100Cr6 balls are extracted from commercially available ball bearings, and subsequently, (B) encapsulated in a resin matrix holder. (C) The resin holder is introduced in a lapping machine where the holder (and the spheres) is abraded until a defined penetration is reached. The lapping ends with a mirror finishing process. (D) After the subsequent laser micromachining process, the resin matrix is gently removed and the truncated microtextured spheres are recovered for the further tribological assessment.

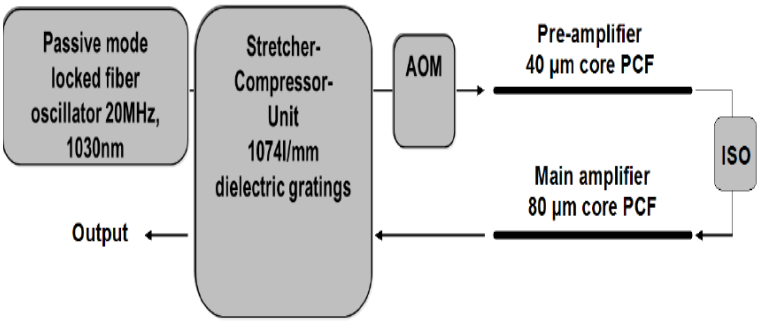

FIGURE 4.5: Sketch of the Active Fiber System GmbH [19]

4.3 Equipment

4.3.1 Laser Equipment

4.3.1.1 Femtosecond laser: Active Fiber System Ultrafast laser

Micro-texturing of the samples was performed by using active fiber system due to the various advantages of ultra short femtosecond pulses in laser surface texturing (e.g. clean textures, and Burr free edges of geometrical patterns). The ultra-short laser source from this Active Fiber Systems GmbH mod.Sci-Series is based on chirped pulse amplification technique (CPA)[19] and a two-stage amplification by diode pumped Yb-doped photonic crystal fibers. The laser source can be sketched as follows (see fig. 4.5). It consist of solid state seed oscillator, working with a passive mode locking system based on a SESAM [88]. The time duration of outgoing pulses is around 500fs with a wavelength 1030nm, and the repetition rate of 20MHz. Dielectric stretcher grating used to temporally stretch the ultra-short pulses from the oscillator up to 500ps and, it consists of a dielectric grating with 1740grooves/mm. An acousto-optic modulator (AOM), allows the repetition rate of the laser to be reduced in the range between 50kHz and 10MHz, by selecting a precise number of pulses.

It has two single-pass amplification stages. Each of them consists of laser diode-pumped Yb-doped photonic crystal fibers, spaced out by an optical isolator, providing a total gain factor of 25000. In particular, the preamplifier fiber is an air-clad

photonic crystal of 1.2m. The core of the fiber has a $40\mu m$ diameter while the internal cladding $170\mu m$ one. This fiber is pumped by a laser diode at the wavelength of 976nm. The maximum gain factor is up to 35dB. The main amplification fiber is 1.2m long and has a $80\mu m$ core diameter and a $200\mu m$ internal cladding diameter. This allows a pump stage by a multimodal diode laser at 976nm, with a coupling efficiency up to 80%. A water cooling system is used to prevent thermo-optical and thermo-mechanical damages in the fiber, when high power are provided. A dielectric compression grating operates for time compression of the previously stretched pulses. The grating consists of 1740grooves/mm. The generated laser beam has a Gaussian profile with a M^2 factor less than 1.5 and linear polarization. The time duration compression grating is mounted on a motorized stage which allows the pulse duration to be varied in the range between 650fs and 20ps. The maximum pulse energy is limited to $100\mu J$ up to 500kHz. At higher repetition rates, the maximum available average power is 50W. Second and third harmonic generators are also provided, with conversion efficiency respectively equal to 50% and 15%.

4.3.1.2 Femtosecond laser: Set-up for pulse selection

In fig. 4.6, the experimental set-up for the surface texturing through Direct Laser Writing by laser ablation is sketched. The laser source is the fiber laser system described in the above section. The linearly polarized beam outgoing from the acousto-optic modulator was converted to circular polarization by means of a quarter-wave plate, in order to prevent anisotropic absorption of light in the inner walls of the craters [98]. To efficiently focus the laser beam on the target, it was first expanded by means of a Galilean beam expander, built by a divergent lens of focal length $f_1 = -25$mm and a convergent lens with focal length $f_2 = 85$mm , before being guided to a computer interfaced galvoscanner, equipped with a $100mm$ focal length F-Theta lens. The laser spot diameter after focusing df can be written as [20]:

$$d_f = M^2 \frac{\lambda}{\pi} \frac{f}{d}. \tag{4.1}$$

In Eq. (4.1), f is the focal length, d is the spot diameter before the focusing lens, λ is the laser wavelength, M^2 is the beam quality factor. From Eq. (4.1), it is clear that

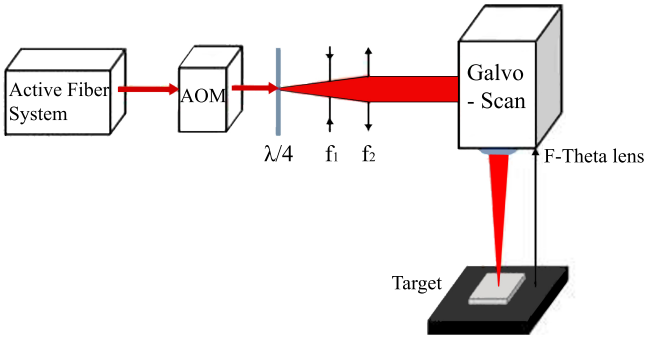

FIGURE 4.6: Experimental set-up for the selection of a precise number of pulses. Two pulse duration were used: 650fs and 10ps. The laser wavelength is 1030nm [20]

the higher the spot before the focusing lens, the more efficient the focalization. In our case, the beam spot size was $25\mu m$ and the galvoscanner F-Theta lens with $100mm$ focal length, allow rays with different incident angles to be focused on the same focal plane, so that uniform working conditions are assured. Moreover, the galvoscanner allows the beam to be moved on the target surface, in order to generate a matrix of craters at different working parameters on the target surface. The targets were placed in the focal plane of the F-Theta lens and then irradiated. The galvoscanner allowed moving the focused beam on the target surface in order to produce different texture geometries by direct laser writing through laser ablation.

4.4 Surface Characterization Equipment

4.4.1 Scanning Electron Microscope

SEM was used to study the surface topography and composition of the material used for laser surface texturing in this research work. A scanning electron microscope works by collecting signals produced when a high-energy beam of electrons hits the surface of the material as shown in fig. 4.7. Typical signals such as back scattered electrons, secondary electrons, characteristic x-rays and light are collected. The primary mode of SEM is the secondary electron mode whereby a high-resolution image of the surface morphology can be obtained with a large depth of focus. The magnification of the image can go from about 40 times to a few ten thousand times depending on the resolution required. Materials have to be electrically conductive to be analysed with a SEM. Non-conductive materials need to be coated with a conductive layer (typically carbon or gold) before it is placed in the sample chamber for analysis. Coating of non-conductive materials can be avoided by using a variable pressure SEM resulting in minimisation of the charging effect. The SEM used in the research to analyze the morphology of the laser ablated microstructures was a SEM of Zeiss Sigma series. It allows the magnification factor up to 500000X, with a resolution of 1.5nm at accelerating voltage of 15kV. It is equipped with two detectors: The InLens detector allows an efficient detection of the secondary electrons generated by the interaction between the primary electrons beam and the specimen surface. The SE2 detector allows detection of both the secondary and the backscattered electrons. These come from the elastic scattering of primary electrons in a deep range of the interaction volume and carry depth information.

4.4.2 Optical Microscope

In this research work, optical microscope was used during the fabrication process. It helps to verify the parameters of the textured geomtries on the sample surfaces during laser surface texturing process. Optical microscope uses a system of lenses to magnify sample images through the aid of visible light. Optical microscopes are

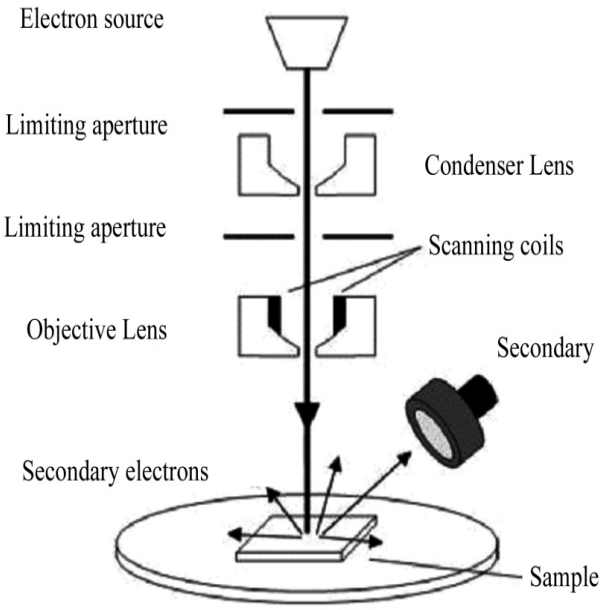

FIGURE 4.7: Schematic diagram of SEM setup [21]

generally connected to a computer system for visualization and the images are captured using a CCD camera and shown on a computer screen for further analysis such as size measurement. Two optical microscope systems were used in the research and they are Nikon Eclipse ME600 and Leica DM4000M as shown in fig. 4.8. The Nikon Eclipse ME600 microscope was equipped with a 100 W illumination stage as well as having the capability of producing high quality optical images. It is equipped with five objectives for 5X, 10X, 20X, 50X and 100X magnification and a PC-interfaced digital camera which allows the measurements of samples features such as the size of the ablated structures composing the texture pattern. A motorized z-axis sample holder allows precise focus on the sample surface and to make valuations of the depth of ablated structures. Two light sources are provided, allowing measurements in both reflection and transmission configuration. The microscope can be used in differential interference contrast (DIC) imaging, which is an imaging method based on the contrast difference of the samples, and in dark field (DF) mode. With DIC and DF, it is possible to see details from optically transparent samples that are invisible in the ordinary microscope images.

Nikon Eclipse ME600

Leica DM4000M

FIGURE 4.8: Optical Microscopes- Nikon Eclipse ME6000, Leica DM4000M(www.bosch.com)

Working Principle

Differential Interference Contrast (DIC), an extension of polarization contrast, is suitable for the visualization of even minute differences in height on surfaces. A birefringent prism (4) is used which splits the polarized light beam into two partial beams on its way to the sample. These two partial beams strike the sample (6) with lateral displacement from each other. If the surface is completely flat, nothing will happen. However, if there is a small step between the partial rays, one of the two beams have to travel along a path which is $2\Delta h$ longer. Once the partial beams have returned via DIC prism (4) and analyzer (7), they display the same direction of vibration again and can interfere with each other in the intermediate image. The path difference experienced on the surface then changes into grey values which can be seen by the eye: steps become visible in the form of relief. As an auxiliary object, the lambda-plate (7a) finally changes the grey values into colors again [99].

Dark Field (DF) is a method where the light is emanating from the illumination lamp and collimated by the Collector. Most of the light is then blocked by the Condenser-aperture-diaphragm, which has a central stop that blocks the central rays of the beam. The light is then reflected by a 45deg mirror with a circular hole in the center. In this way, the light travels towards the sample on the outside of the actual objective lens. It is then focused on the sample by an inner mirror at the end of the objective housing. Light is deflected by any unevenness on the sample surface, and part of it is passed back via the objective lens to the eye of the operator

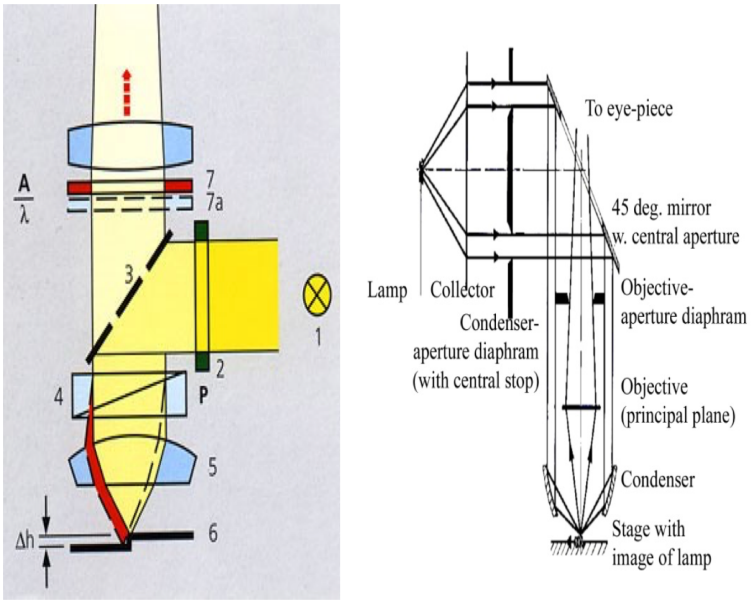

FIGURE 4.9: Schematic diagram of Microscopic setup [22, 23]

[22]. In this way, no directly reflected light is seen by the operator (i.e. a perfectly clean mirror surface appears black). Only height differences, given by the dust and edges, on the surface are seen in the image.

4.4.3 Microscopy technique (confocal):

Two different Confocal microscope systems were used in this research work. They are chosen according to the amount of surface area required to be scanned. Larger surface areas were scanned by CSM confocal microscope and smaller surface areas were scanned by Olympus LEXT OLS 4000 Confocal Laser Microscope. In addition, confocal microscopy offers several advantages over conventional wide field optical microscopy, including the ability to control depth of field, elimination or reduction of background information away from the focal plane.

FIGURE 4.10: CSM Platform (Open Platform) [www.csm.com]

4.4.3.1 CSM- Confocal Microscope

The ConScan Objective represents the perfect combination of fine resolution 3D confocal microscopy and the advantages of light microscopy. It provides high resolution 3D chromatic confocal technology for analyzing the 3D topography of micro-scratches and micro-indentations. It allows the non-contact measurement and also opens up new possibilities in quantitative surface characterization in the micron range by using two objectives for different height ranges. By scanning the sample surface in the x-y directions, the ConScan provides the micro-topographic structure of any type of surface (rough, as well as polished) for any type of material. This includes glossy, transparent and opaque materials, which can prove extremely difficult to image with other conventional imaging systems.

Measurement Principle:

White light confocal microscopy

The concept behind confocal microscopy involves the use of the chromatic length aberration (CLA) principle. The first step in optical confocal analysis is to produce white light and direct it through a filtering optical component towards the surface of the sample. With use of the chromatic aberration caused by the dispersive lens, the white light is separated into its component wavelengths, each of which corresponds

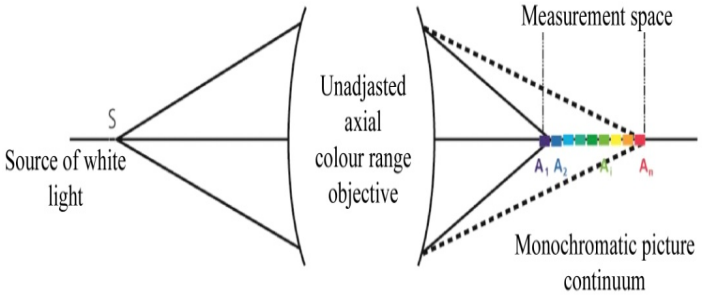

FIGURE 4.11: Chromatic coding principle[www.csm.com]

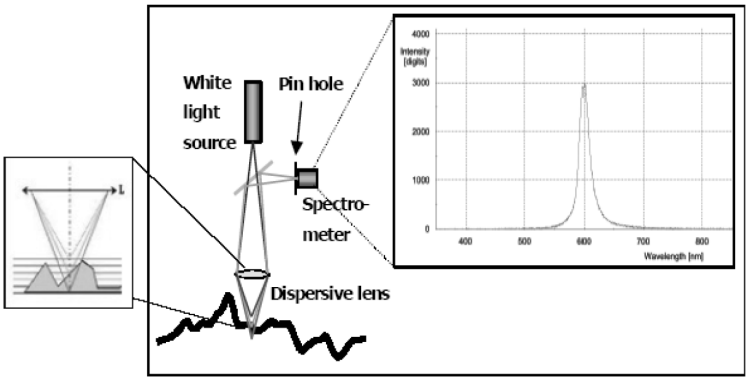

FIGURE 4.12: Image acquisition principles of the ConScan objective[www.csm.com]

to a different z-coordinate in the optical axis. This separated light reaches the sample surface as a continuous wavelength-coded range of foci.

As each wavelength is represented at a different distance from the lens, the returning light waves will be different according to the height characteristics of that specific area of the sample. Therefore, the resultant spectrum can be regarded as a spectrophotometric signature of the material surface; spectral peaks represent the "height" of the sample at that focus point. The system scans over the surface of the sample, creating these spectral height signatures at sub-micron intervals, summating to an overall image with axial accuracy in the nanometer range [100, 101].

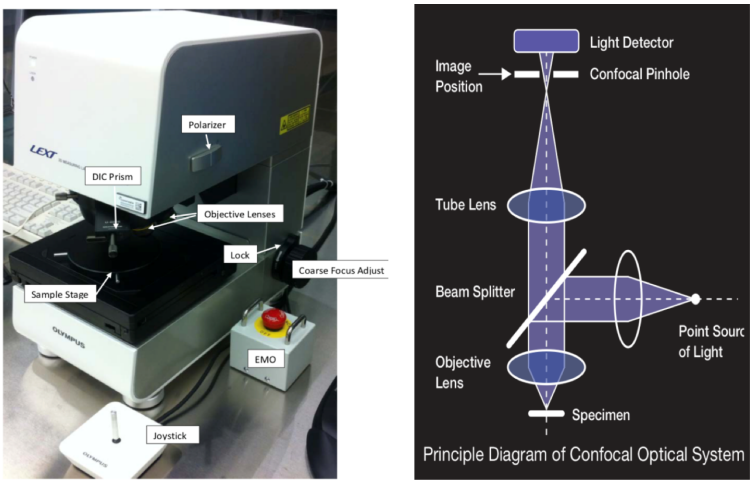

FIGURE 4.13: Features of the Confocal 3D Microscope [24]

4.4.3.2 Olympus LEXT OLS 4000 Confocal Laser Microscope:

The Olympus LEXT OLS4000 is a confocal microscope capable of taking high-resolution 3D images. The magnification (Optical and Digital) of this microscope ranges from 108x – 17,280x. It is capable of resolving features 10 nm in size in the z direction (sample height) and 120 nm in the x-y plane. The system is capable of performing a variety of metrology measurements. Step height, surface/line roughness, and area/volume measurements are some of the more commonly used metrology measurements. The LEXT OLS4000 is equipped with a confocal optical system that only captures the in-focus image while simultaneously eliminating flare. In addition, the confocal technology can be used as a height sensor because only thin image planes of the same height are captured. The operation of LEXT OLS4000 in the confocal mode consisted in generating an image on the basis of light reflection from the discrete focal plane. The light, creating an image with different focusing depth, was eliminated using the double confocal pinhole aperture.

In this mode, the microscope used a light beam with wavelength $\lambda = 405nm$ (violet), and the light source was a LED, with 120 mW of power. Obtaining a spatial mapping of the examined object's surface entailed its precise scanning, point by point on x-y axes. This process was realized by a special scanner patented by Olympus. The scanner used a Micro Electro-Mechanical System (MEMS). The images were acquired using a system of two photomultipliers, with average (standard) and high

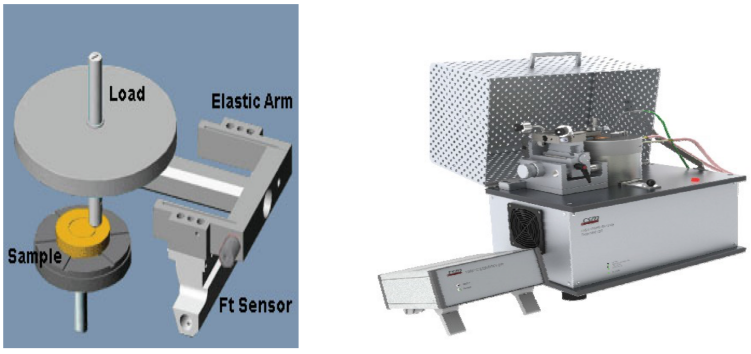

FIGURE 4.14: CSM High Temperature Tribometer[csm.com]

sensitivity. Such a system enabled proper amplification of the optical signal. Therefore, it allowed for measuring the surfaces of elements with a low reflection coefficient and large surface slope angle, up to 85 degrees. The motorized revolving nosepiece included a set of 5 microscopic lenses with various magnification ranges.The samples were placed on a motorized stage that allowed for precise realization of displacement on x-y axes (range: 100 mm) and axis z (range: 10 mm) [24].

4.5 Tribometry or Tribological Equipment

Tribological properties were evaluated by using three different tribometer and they are CSM high temperature tribometer, MCR Rheometer 301 and Plint-off Tribometer. These tribometeres are choosen according to the type of contact between two rubbing bodies, e.g, conformal or non-conformal point contacts, reciprocating sliding contacts etc.

4.5.1 High Temperature Tribometer - CSM Instruments

The instrument allows to measure friction forces, friction coefficients, wear rate as a function of the sliding velocity in a pin-on-disk or ball-on-disk configuration. It can be operated with rotational speed between 0.3-500 rpm , load ranges up to 60 N, frictional force up to 20 N, and temperature range between $420 - 1000^oC$.

It can precisely calibrate friction and wear measurements at elevated temperatures up to 1000^oC. Efficient heating/cooling system to accurately maintain desired test temperature, high thermal stability, automatic shut-off at selected track length or friction coefficient threshold, test in liquids, within their thermal stability range.

In tribometry, a flat, a pin or a sphere is loaded onto the test sample with a precisely known force. The pin is mounted on a stiff lever, designed as a frictionless force transducer. The friction coefficient is determined during the test by measuring the deflection of the elastic arm. Wear coefficient for the pin and disk materials are calculated from the volume of material lost during the test. This simple method facilitates the study of friction and wear behavior of almost every solid-state material combination with or without lubricant. Furthermore, the control of the test parameters such as speed, frequency, contact pressure, time and the environmental parameters (temperature, humidity and lubricant) allows simulation of the real-life conditions of a practical wear situation. Experiment stops automatically when the coefficient of friction reaches a predefined threshold value or when a specified number of cycles is reached.

In our experiments, the core of the system is simply constituted by a rotating sample-disk (Aluminum alloy 6061 sheet with a measured root mean square surface roughness of Ra=.08 μm) in contact with laser surface textured truncated spheres. A pin-on-disc tribometer consists of a stationary "pin" under an applied load in contact with a rotating disc (alumina sheet). A Normal load of 2 N was applied to a textured steel ball (9 mm diameter), used as a counterpart material. The contact pair (disk and pin end) was immersed in a lubricant bath, whose temperature was constantly monitored during the tests. The adopted lubricant is a pure mineral oil (Oroil Therm 7 from Orlando Lubrificanti S.r.l., Argenta, Italy), with dynamic viscosity $\eta = 0.0516 Pas$ at 50^oC.

4.5.2 Rheometer

An MCR 301 rotational rheometer from Anton Paar was used for tribological tests. The instrument controls the rotational speed and measures the resulting torque very accurately. In addition force controlled measurements are possible by applying a

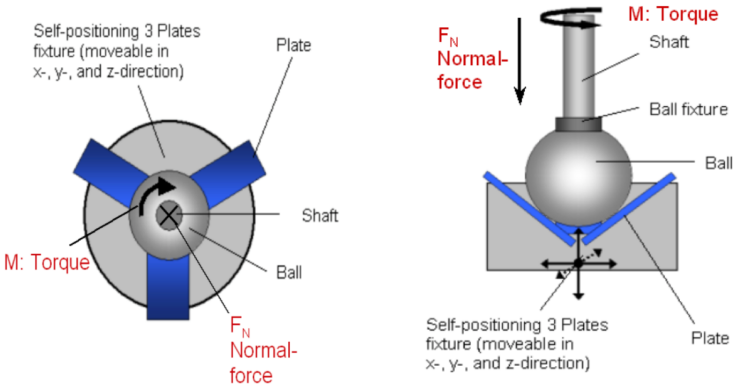

FIGURE 4.15: Schematic representation of the ball on three-plates-device in side and top view. The torque and the normal force applied by the rheometer are indicated by arrows

torque and measuring the resulting speed. The normal force can be set and recorded during all tests. The MCR 301 rheometer used features the following measurement ranges: rotational speed: 10^{-6} to 3000 rpm; Torque: 10^{-2} to 0.2Nm; normal force: 0.01 to 50N.

The rheometer MCR-301 was used as a tribometer to perform the friction test under a normal force of 20N at 25^oC. The setup is based on the ball-on-three-plates-principle (or-ball-on-pyramid) consisting of a steel ball holder, an inset where three small plates can be placed, and a bottom stage movable in all directions on which the inset can be fixed. fig. 4.15 depicts the setup schematically. The ball fixture enables the use of balls made of different materials, and their easy replacement. The plate texture at the bottom part is mounted on a specially designed spring system allowing motion in all directions of the coordinate system: x, y, z. This flexibility ensures the concentric positioning of the fixture to achieve a uniform force distribution from the ball onto all the three plates.

The rotational speed applied to the shaft is producing a sliding speed of the ball with respect to the plates at the contact points. The resulting torque can be correlated with the friction force by employing simple geometric calculations. The normal force (F_N) of the rheometer is transferred into a normal load (F_L) acting perpendicular to the bottom plates at the contact points. We have, then, the following relations:

$$F_L = \frac{1}{3}\sin(\alpha)F_N, \tag{4.2}$$

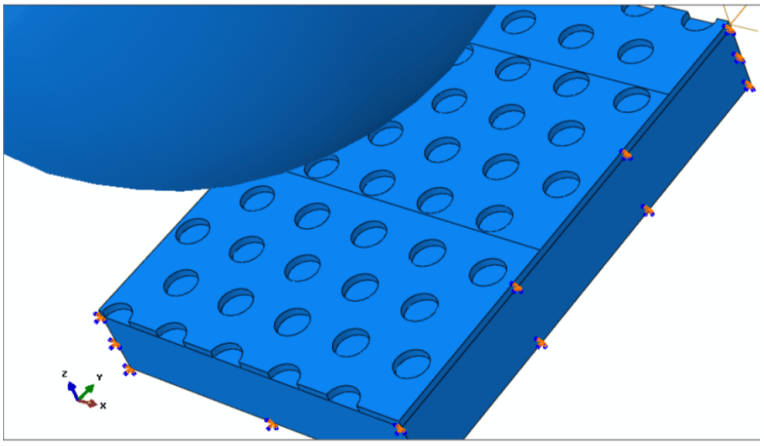

FIGURE 4.16: Schematic representation of the ball in contact with the textured surface

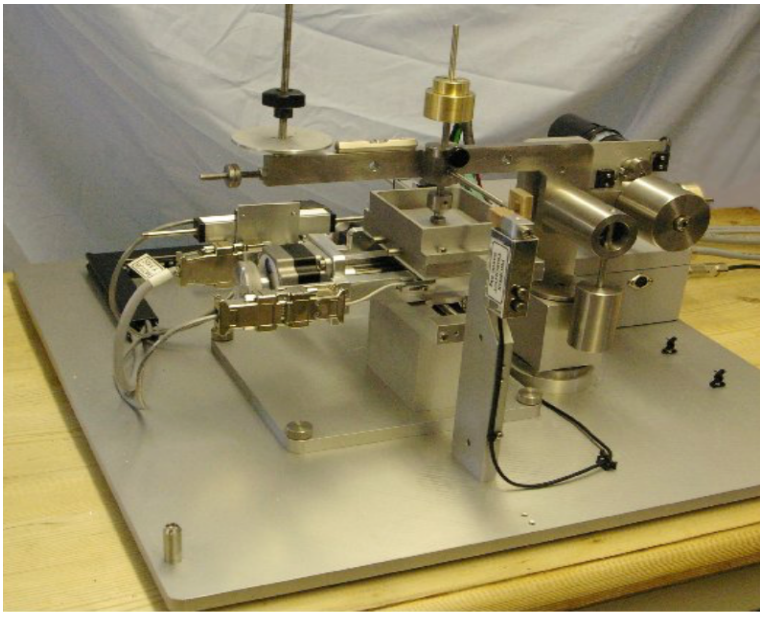

FIGURE 4.17: FTE79 Tribometer

with r_{ball} being the radius of sphere and α the angle of the plates, respectively. In the specific configuration employed in the apparatus, we employ $\alpha = \pi/4$, a ball with a radius $r_{ball} = 6.35mm$, a force; $F_N = 20N$ thus,$F_L = 4.71N$.

4.5.3 TE79 Tribometer:

A Phoenix TE79 tribometer (England) was used to determine the coefficient of friction of the textures under reciprocating sliding contacts. It comprises the loading and friction force measurement system mounted on a base plate, control hardware with PLINT SLIM 2000 serial interface unit and control software. The machine is bench-top mounted and includes a transparent enclosure and ambient humidity and temperature sensor. The enclosure is also used as a safety cover for the machine and incorporates a magnetic proximity switch. The machine will not run if the enclosure is removed. The fixed pin or ball sample is carried on a trunnion and gimble mounted loading beam. This is counterbalanced both to give a neutral balance and to bring the centre of gravity onto the contact plane. Load is applied by dead weights in a range from 0.1 N to 50 N. The loading beam is restrained by a strain gauge force transducer in a sliding link. This link ensures that only the tangential component of force in the contact (the friction force) is measured even with the large deflections associated with elastomeric test pieces. As the lower specimen surface moves the friction force on the ball or pin sample is measured. The load beam lift/lower is servo controlled so that the load can be applied at a specific point in the test. The program can also introduce a dwell between load application and movement. This dwell period is an important parameter in determining the start-up friction in elastomeric contacts. [phoenix-tribology.com].

In reciprocating mode of the TE79 Tribometer, it provides X/Y axis movement with linear positional feedback. Tangential (friction) force measurement is in the X direction. The axes are formed by cross-axis linear slides with 1 mm pitch lead screws and are driven by stepper motors. The fixture for the lower (moving) specimen includes an electrical resistance heater and two thermocouples for temperature measurement and control above ambient conditions. A programmable motion controller is used to coordinate movement of the two axes. Numerous motions are possible including: Simple reciprocating along one track in the X direction. Reciprocating in the X direction with indexing in the Y direction at stroke end, so that the wear track resembles a square wave. Reciprocating in the X direction with indexing in opposite Y directions at stroke end, so that the wear track is rectangular.

In this thesis, a reciprocating ball-on-disk sliding approach was used with total cycle count of 300 and stroke distance of 5 mm, giving a total sliding distance of 1.5 m. Samples were ultrasonically cleaned in Teepol and Acetone, each for 5 minutes. An 8 mm diameter alumina counterpart ball was used for all tests, with a new clean spot being used for each test. A load of 200 gf (2 N) was used with an approximate Hertzian contact pressure of 750 MPa. The conditions tested were varying sliding speeds (5, 10, 50, 100, 500 & 1000 mm/seconds), temperatures (20 C, 40 C, 80 C) and lubricants (dry, glycerol, 15W40 mineral oil). Stribeck curves have been produced by comparing the average coefficient of friction and calculating the Hersey number for each sample type. Hersey numbers were calculated using the following formula:

$$HerseyNumber(dimensionless) = \frac{speed(mms^{-1}) \times viscosity(mPa \cdot s)}{Load(mN)}. \quad (4.3)$$

4.6 Pressure measurement system: Pressure Distribution Mapping System FPD-8010E

FPD-8010E was used to produce multi-faceted measurement data such as pressure distribution in our experiments. The Prescale Digital Analysis System (FPD-8010E) works with Prescale film to quantify pressure data in numerical format. Prescale^{TM} pressure indicating film measures contact pressures as low as 7.25 psi up to pressures as high as 43,500 psi. When pressure is applied, tiny microbubbles burst within the film to show the various degrees of pressure, through color density, that corresponds to the pressure and pressure distribution. The Digital Analysis System quantifies the output on your used Prescale film. User-friendly software includes on-display pressure distribution and enlargement, cross-sectional distribution, 3D image display.

4.7 Contact Angle Measurement System

Contact angle is a quantitative measure of the wetting of a solid by a liquid. The instrument of choice to measure contact angles and dynamic contact angles is an

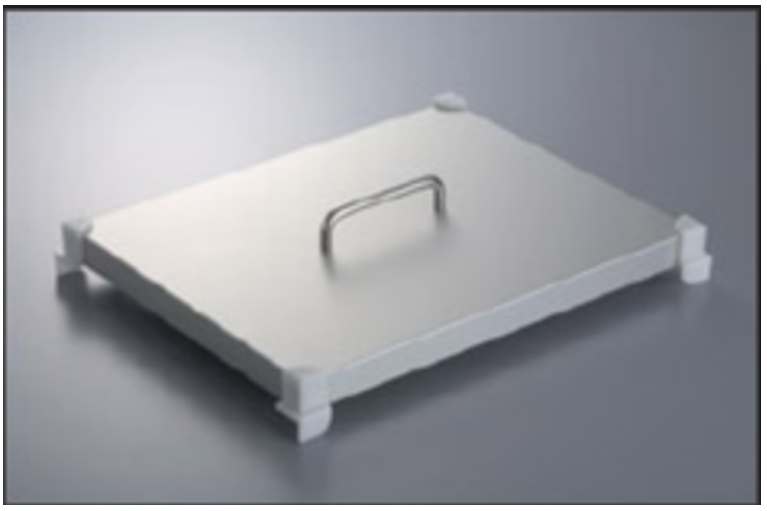

FIGURE 4.18: FPD-8010 E [Fujifilm.com]

optical tensiometer. Surface chemistry (wettability) of the laser textured surfaces were analysed by using optical tensiometer in this research work.

4.7.1 Attension theta optical tensiometer

An optical tensiometer records drop images and automatically analyzes the drop shape. The drop shape is a function of the surface tension of the liquid, gravity and the density difference between sample liquid and surrounding medium. On a solid the drop shape and the contact angle also depends on the proper- ties of the solid (e.g. SFE, topography). The captured image is analyzed with a drop profile fitting method in order to determine contact angle and surface tension. Surface free energy can be calculated by performing contact angle measurements with several known liquids. As an optical method, the measurement precision of optical tensiometers depends on the quality of the pictures and the analysis Software. Attension Optical Tensiometers utilize a high quality monochromatic cold led light source to minimize undesirable sample evaporation. Image quality is guaranteed by a high-resolution digital camera, quality optics and the accuracy of the drop fitting method.

A video-based optical contact angle measuring device, Attension Theta Optical Tensiometer, was used to assess the wettability properties of the surfaces. Using the sessile drop technique, the static contact angle (CA) was measured by dispensing

FIGURE 4.19: Theta Optical Tensiometer [google image]

droplets of 6ul under atmospheric conditions and after stabilization. In addition of glycerol and mineral oil, Milli-Q water was used to compare the wettability values of hydrophobicity or hydrophilicity. A hot stage was used in order to heat both the sample and the dispensed liquid to 80degC. All measurements were repeated 3 times for statistical purposes. Spreading curves were obtained by analyzing droplet images recorded each 10 frames per second, starting from the first contact of the droplet onto the surface and for a duration of 25s. Spreading values were estimated by measuring the diametric contact distance of the drop to the surface and projected to calculate the area of a disk.

Chapter 5

Results and Discussion

This chapter reviews the tribological effects of the micro-surface texturing on the technological steel. It also reviews the different experimental procedure to examine the tribological effects in conformal and non-conformal contacts, which are explained in different section in this chapter. Firstly, we have investigated the non-uniform geometrical patterns for bearing pads, and later we have investigated the effects of different geometrical patterns in non-conformal point contacts. Further, we have studied the tribological and wettability behavior of different micro-textured geometrical patterns in reciprocating sliding contacts.

5.1 Non-Uniform Laser Surface Texturing of an Un-Tapered Square Pad for Tribological Applications

As a first research work, we have exploited the intrinsic flexibility and micrometric accuracy of femtosecond laser ablation to realize complex micro-structural modifications on the surface of a laboratory prototype of a steel thrust bearing (untapered) pad. Such experimental work follows some theoretical predictions achieved by employing the Bruggeman Texture Hydrodynamics theory (BTH) to design an anisotropic and non-uniform texture maximizing the thrust load of the pad prototype[25].

The resulting micro-structured surfaces have been tribologically tested in fully-flooded lubricated conditions in order to verify the existence of a macro-hydrodynamic friction regime induced by the collective flow actions of the micro-structural defects.

One of the proposed optimal texture geometries, calculated by adopting a multigrid optimization procedure based on a genetic algorithm, is depicted in fig. **??** for the square pad geometry[25]. In the figure, the red stripes show the local angular alignment of the grooves, whereas the red circles indicate the untextured areas. The number of the stripes, which have been drawn in the fig. 5.1, have only a qualitative purpose, i.e., they do not represent the lattice spacing and the dimensions of the defects, nor have they been somehow scaled. They only represent the areas where the dimples are located over the squared pad, as well as their orientation. We observe that the microgrooves have been aligned in such a way to hinder the flow of the lubricant towards the lateral direction, thus preventing any immediate leakage and, hence, friction increase. Furthermore, the stripes inclination close to the lateral boundaries enables the redirecting of the fluid, at a scale larger than the scale of the grooves, towards the internal portion of the domain, through a micro-herringbone construction. This determines a large number of fluid particles sheared at the contact interface and, consequently, an increase in the bearing pressure. In addition, expulsion fingers have been created on the outlet corners of the pad with the aim of lengthening the fluid path under the pad domain. Indeed, the expulsion fingers redirect part of the flow, which normally would exit from the middle part of the rear side, toward the rear part of the pad. In this way, each fluid particle exerts a prolonged shearing action. Such a combination of expulsion fingers and micro-herringbone geometry significantly increases the load support capabilities to the extremely lengthened particle route under the contact. This finally positively affects friction, which is consequently reduced due to an increased mean interfacial separation.

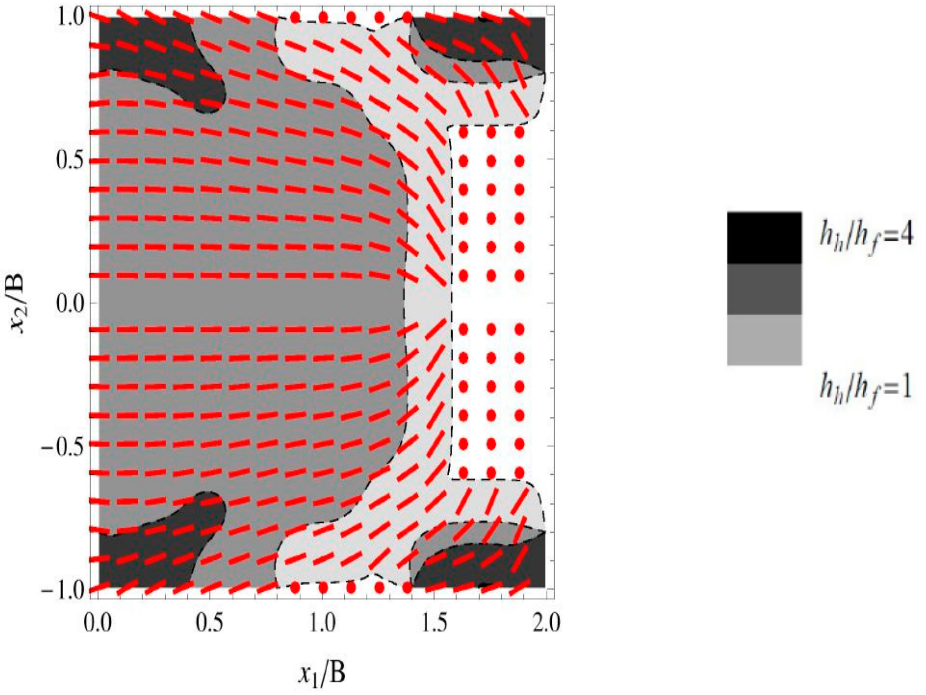

FIGURE 5.1: Schematic representation of an optimized micro-grooved partial textured squared pad. The red circles indicate the untextured areas, while the red strips show the local angular alignment of the grooves. The gray scale indicates the dimple depths, where hh is the dimple depth and hf is the nominal separation between the two sliding surfaces. Adapted from [25] with the permission of the author

5.1.1 Fabrication of Samples

The fabrication of the surfaces on the truncated spherical caps were produced by operating at the lowest achievable repetition rate of 50 kHz and an average power of 50 mW. The high level of accuracy and reproducibility of the ablated micro-features is, indeed, only achieved by working with near threshold laser fluence. The focused spot size on the sample surface was about 15 μm. Three of the circular truncated surfaces, obtained with the sample preparation procedure described in Section 4.1.2.1 of chapter 4, were laser-machined as follows.

The grey area shownin the fig. 5.2 was removed by femtosecond laser milling reaching the depth of more than 100 μm, which is an order of magnitude higher than the expected average fluid thickness under the bearing. We have used one of the milled samples as a flat control squared pad. The other two samples were laser machined

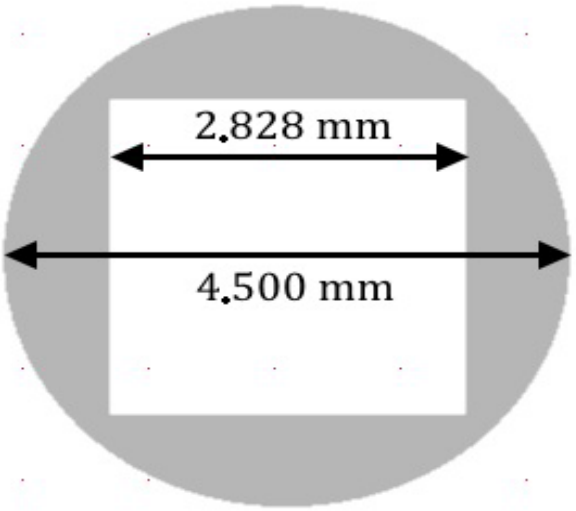

FIGURE 5.2: Schematic representation of the truncated bearing. The grey area was removed by laser milling up to 100-μm-depth

with the defined geometry. As according to the theoretical design, which is described in fig. 5.1, a texture pattern composed of five groups of micro-grooved dimples with different depths, ranging from 5 μm to 25 μm (fig. 5.3), was machined inside the squared section. Each dimple is contained within the dimensions of an imaginary square cell of length 200 μm and width 40 μm, as represented in fig. 5.3(b). The area ratio of the texture is about 50%. The deeper dimples have been positioned in the suction and expulsion fingers located at the corners of the textured area. The variable inclination of the dimples with respect to the sliding direction follows the red stripes, as shown in fig. 5.1, which aim to guide the fluid towards the internal part of the pad.

The two laser textured samples differ in the way the dimples were realized. In one sample, dimples of elliptical shape were fabricated by moving the laser beam along a path of four concentric ellipses with a hatch distance of 3 μm. In the other sample, each dimple was micro-machined by drawing an array of equidistant parallel ablation traces with a lateral displacement of 3 μm one from each other, resulting in a micro-groove of almost rectangular shape (see fig. 5.3(c)). Following the scheme of fig.

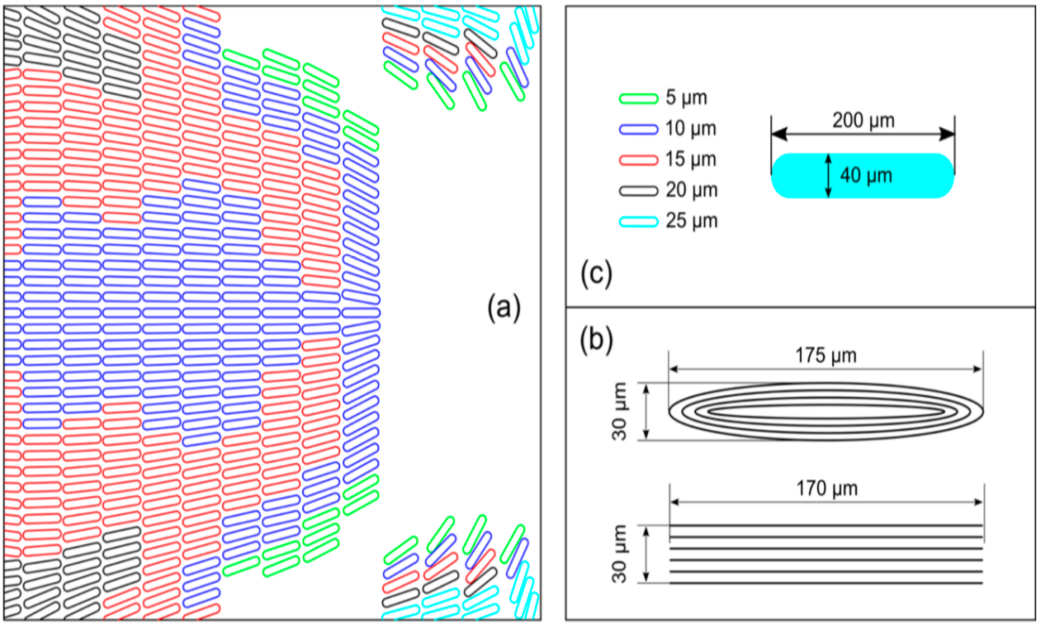

FIGURE 5.3: (a) Schematic of the texture pattern; (b) dimple size; (c) ablation strategy to realize each dimple

Dimple Depth (μm)	**Number of Loops (Elliptical Shape)**	**Number of Loops (Rectangular Shape)**
5	5	4
10	10	9
15	15	14
20	20	19
25	25	25

TABLE 5.1: Number of loops for each dimple depth and shape.

5.3(a), the ablation depth of each dimple was accurately controlled by adjusting the number of overlapped loops. In Table 5.1, the number of loops executed to target each dimple depth is reported according to the dimple geometry. The translation speed of the focused laser beam on the sample surface was held constant at 20 mm/s. After the femtosecond laser surface, micro-texturing, the samples were cleaned in an ultrasonic bath to remove the loosely attached ablation debris.

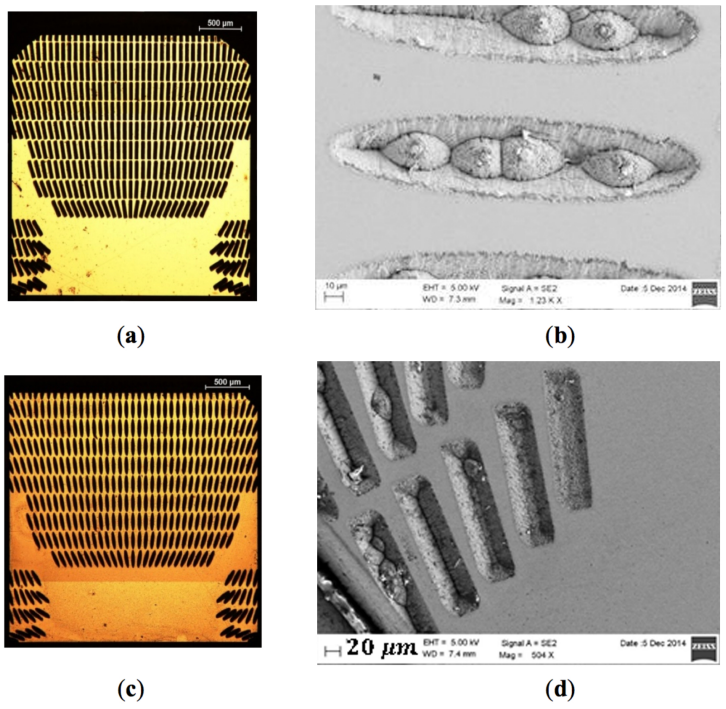

FIGURE 5.4: Optical microscope images of the overall textured area, and high magnification SEM images of some micro-grooved dimples of sample with rectangular (a,b) and elliptical (c,d) shape texture pattern

5.1.2 Morphological Characterization

The morphology of the fabricated micro-features was characterized by optical and scanning electron microscopy. fig. 5.4, shows an overall view acquired with an optical microscope of the worked area of the two samples with rectangular and elliptical dimples, respectively, together with high magnification SEM images of some micro-grooved dimples. The machined part is completely free from melting and burrs, due to the high level of accuracy provided by the ultrashort pulse duration ablation regime, together with the near threshold laser fluence selected for the LST process. The confocal microscope analysis confirmed that the depth of the dimples met the required specifics with micrometer precision, as, for example, reported in fig. 5.5 incase of rectangular dimple with three different depths of 10μm, 15 μm, and 20 μm, corresponding to 9, 14, and 19 laser scanning loops, respectively. However, as it can be already noticed in fig. 5.5 (c), with the increase of the number of loops and the dimple depth, some morphological defects start to appear. In particular, the bottom of the dimples is more irregular and the vertical walls are more tapered.

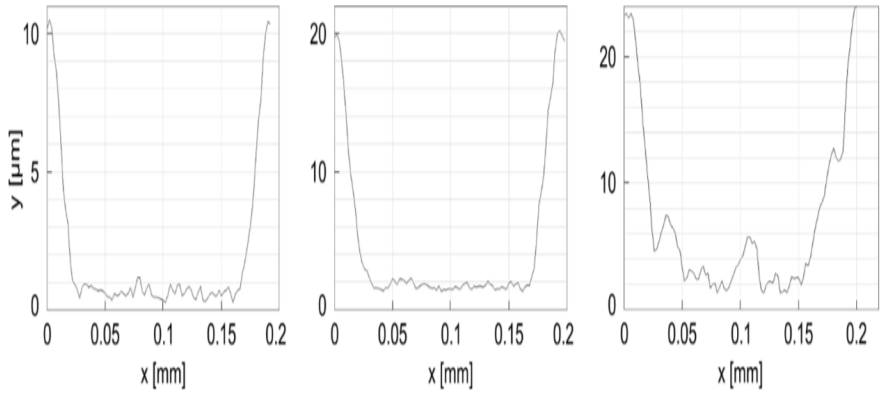

FIGURE 5.5: Confocal profiles along the major axis of an ablated rectangular dimple after (a) 9 loops; (b) 14 loops; and (c) 19 loops

This effect can be ascribed to the attenuation of the laser fluence hitting the bottom of the dimples as far as the depth increases. It is not the beam that attenuates but the laser fluence, and this is due to the fact that the beam focus is on the surface, therefore below the surface the beam is diverging. As far as the depth increases the beam spot increases and the fluence drops. Since we are already working at a near threshold fluence (because we want to avoid completely melting and burrs at the edges), even a small drop of the fluence due to the beam divergence results in a decrease of the ablation rate, causing metal particles re-deposition inside the dimples. The possible way to solve this issue is to increase the focal length but by increasing the focal length also the spot size increases. Therefore, a trade-off has to be found. This problem is more pronounced in elliptical dimples because at the two edges of the ellipse, the ablated metal particles has more difficulty to escape out of the dimples (also due to the low fluence) and redeposit into the dimple. In case of rectangular dimples the particles have more space to escape.

5.1.3 Tribological Characterization

The tribological characterization of the LST samples was carried out on pin-on-disk Tribometer. Lubricant temperature was constantly monitored during the tests. A

normal load was applied to the sphere holder by means of a calibrated weight. The following tribology experiments were conducted on the samples. Firstly, the Stribeck curves of the two (elliptical and rectangular dimple patterns) laser textured pads, applying a load of 1 N, were measured and compared, aiming to find out which of the two dimple geometries yielded the best tribological performance. Each measurement consisted of several steps. During each step, the disc was rotated at a constant speed while the tangential displacement value of the elastic supporting arm of the ball holder was detected by a Linear Variable Displacement Transducer (LVDT). The displacement sensor signal was converted via software into a tangential force value T through a suitable calibration curve. Being known the normal load N, the total friction coefficient was calculated by (the ratio of the tangential force T with the normal force):

$$f_t = \frac{T}{N}, \tag{5.1}$$

The friction coefficient μ between the two surfaces was obtained from:

$$\mu = f_t - f_d, \tag{5.2}$$

where f_d is the friction coefficient between the ball holder and the lubricant oil, which was experimentally estimated by raising the arm and separating the two surfaces. Following this procedure, the friction coefficients of the two laser-textured pads at different sliding velocity U of the disk ranging from 324 mm/s to 15.0 mm/s were determined and plotted. We started with the fastest speed, where the lubrication regime was always of the hydrodynamic type, and changed it towards slower values in each step. This practice was adopted to strongly minimize any possible undetectable surface wear. Each measurement was repeated 5 times in order to have a mean value of μ with its related error, along with constant monitoring of the oil temperature. Before testing on another sample or at another condition, all components of the tribometer that came into contact with the lubricating oil were carefully cleaned and the aluminum base was polished. The laser textured pad exhibiting the best tribological performance was further investigated by measuring the Stribeck curves in case of three different loads of 0.25 N, 1.0 N, and 1.5 N, respectively.

Finally, in order to evaluate the hydrodynamic contribution of the anisotropic texture pattern, the tribological behaviors of the texturized sample and the control untextured one were compared by operating the tribometer in reciprocating mode. In this mode, the rotation speed is periodically inverted with a frequency that can be set by software. The LVDT sensor still estimates the tangential force value (T) which is, in this case, alternatively positive and negative. Alternately reversing the sliding contact direction with respect to the texture distribution allows for better highlighting of the anisotropic behavior of the texture pattern. These last measurements were conducted at a constant temperature of $24 \pm 2\,\mathrm{deg}\,C$, a rotating speed of 0.136 m/s, a normal load of 0.25 N, and a reversing frequency of 1 Hz.

5.1.4 Results and Discussion

The comparison of the tribological behavior of the textured pads with elliptical and rectangular dimples at different sliding speeds is represented in fig. 5.6. From the Stribeck curves, both obtained by maintaining a constant temperature of $20\mathrm{deg}\,C$ and applying a load of 1 N, the three lubrication regimes can be easily recognized. At sliding speeds, slower than 0.03 m/s, the measured friction coefficient is relatively high, typical of the boundary lubrication.

For speeds in the range between 0.04 and 0.1 m/s, a mixed lubrication regime is established and the friction coefficient decreases until, by further increasing the speed above 0.2 m/s, it starts growing again because of the fluid hydrodynamic resistance. Although the trend of the two Stribeck curves is similar, it can be noticed that the friction coefficient measured for the pad with elliptical dimple texturing (sample E) is always approximately 20% higher compared to the rectangular geometry (sample L). This is explained by the greater number of morphological defects noticed at the bottom of the deepest elliptical dimples due to re-deposition of particles. The defects at the bottom can be seen from the profile of figure 5.5 (c), where we can see that in the case of the deepest dimples (the one with 19 loops) some protusions are present at the bottom of the dimples. The more the texture geometry differs from the theoretical design, the less effective is the collective contribution of the dimple pattern to reduce friction. This consideration also applies to the smaller area coverage of the elliptical texture with respect to the rectangular texture. Indeed, in this study the

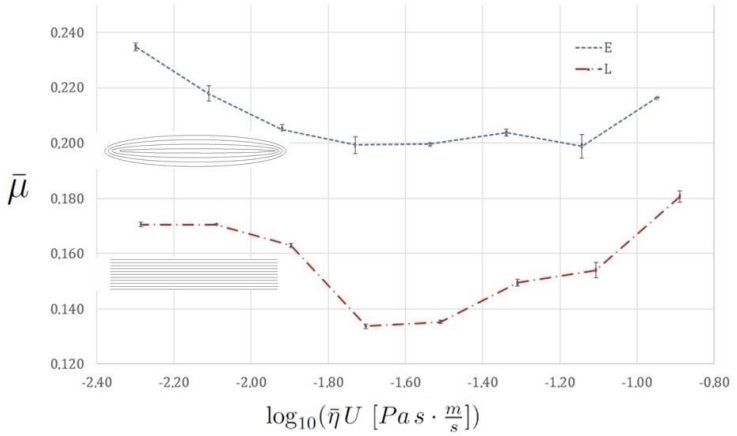

FIGURE 5.6: Comparison between the Stribeck curves measured for the two textured pads with rectangular (sample L) and elliptical (sample E) micro-grooved dimples, respectively. The temperature was set at 20 $\pm$ 2 deg C and a normal load of 1 N was applied during the measurements

obtained different texture area density is the consequence of keeping an equal lattice spacing between the two textures (in order to reduce the experimental parameters). Unfortunately, this leads to a larger boundary contact area in the boundary regime and to a lower average interfacial separation (in the inlet zone) in the hydrodynamic regime for the elliptical texture, with a consequent friction increase. Since it showed better tribological performances, the pad with the rectangular dimple pattern was further investigated by measuring the Stribeck curves at three different loads, i.e., 0.25 N, 1 N, and 1.5 N, with linear sliding speeds ranging from 324mm/s to 15.0 mm/s. The results are illustrated in fig. 5.7, where it is clearly noticeable that, especially for the load below 1 N, the designed anisotropic texture pattern generates a hydrodynamic lubrication regime in a wide range of sliding speeds. It is worth noticing that such hydrodynamic regime is the fingerprint of the anisotropic texture, given that it would not be produced through the wet sliding contact of the untextured surface. In addition, it is worth noticing that for the highest load of 1.5 N, the friction coefficient significantly reduces at values below 0.13 for sliding speed faster than 0.1 m/s, as related to the occurrence of the friction minimum in the mixed lubrication regime.

Finally, the textured and the untextured flat control samples have been tested under reciprocating sliding contact, in order to highlight the effect of sliding speed

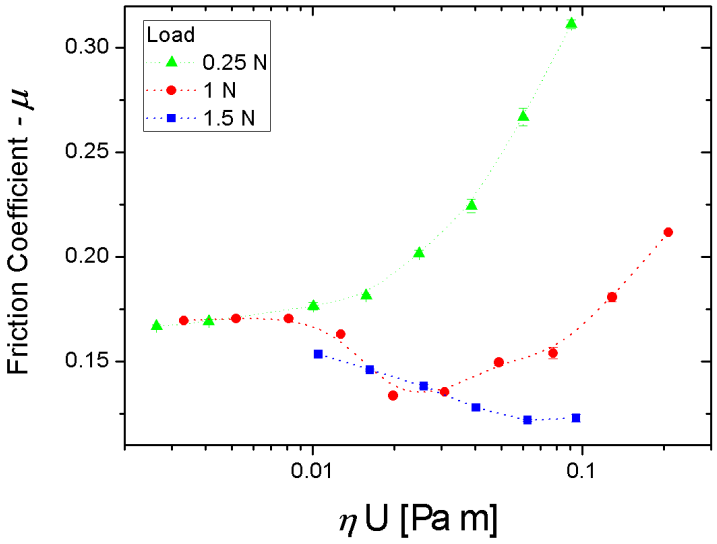

FIGURE 5.7: The mean coefficient of friction as a function of for the textured sample at three different normal load values as a function of the sliding speed. The temperature was set at $20 \pm 2\,\mathrm{deg}\,C$

direction and texture anisotropy on the friction. In particular, the friction force has been measured on the flat control surface and on the textured sample "L" as a function of the reciprocating motion time in fig. 5.8 and fig. 5.9, respectively. The measurements have been performed keeping the oil bath temperature at a constant value of $24 \pm 2\,\mathrm{deg}\,C$, the average sliding speed at 136 mm/s, and applying a normal load of 0.25 N. The sliding speed was periodically reversed with a frequency of 1 Hz. In both graphs, the ratio between the measured (apparent) tangential force and the normal load is reported as a function of contact time. In the first approximately 30 s of the measurements, the arm of the tribometer was raised and the tangential force is relatively low oscillating with positive/negative small values around the zero, according to the rotation direction of the disc. When the arm was lowered, the tangential force absolute value is much higher exhibiting the same oscillation behavior. However, in the case of the untextured control sample (fig. 5.8), the oscillations are symmetric with respect to the zero, as must be expected. The textured sample results shown in fig. 5.9 reveal, instead, a substantial asymmetry of the oscillation amplitudes. Here, the tangential force is twice as intense when the direction of rotation is opposite to that for which the texture pattern has been designed. The same measurement was repeated for four different time intervals, obtaining similar behaviors and thus proving confidence in the results and supporting the existence of

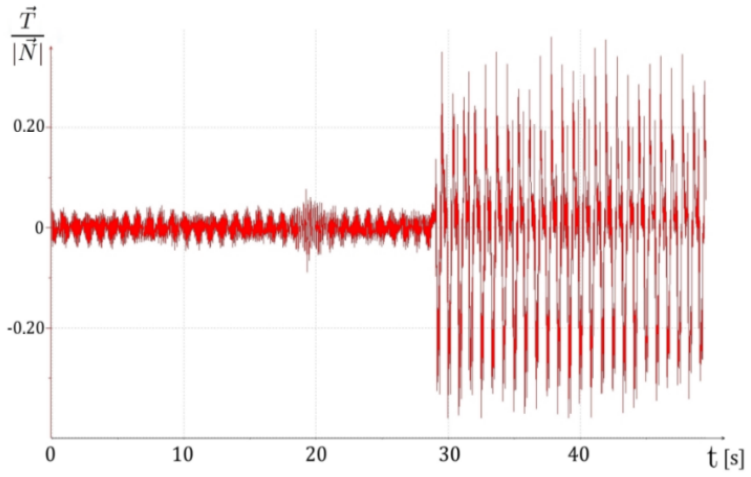

FIGURE 5.8: Friction coefficient behavior calculated as the tangential force T to the normal force N ratio, measured in the case of the untextured sample. The tribometer operates in the reciprocating mode with isothermal conditions of the oil bath ($24 \pm 2\,\mathrm{deg}\,C$), linear translation speed of 136 mm/s reversed with a frequency of 1 Hz, and a normal load of 0.25 N

the micro-hydrodynamic collective contribution originated by the anisotropic surface microstructures.

5.1.5 Conclusions

Exploiting the high level of precision and flexibility achievable through femtosecond laser ablation, square un-tapered bearing pads with non-uniform surface micro-texturing have been fabricated starting from flattened steel spheres. Specifically, an innovative texture pattern design was implemented consisting of a non-homogeneous array of surface micro-grooved dimples of different depths, inclinations and distribution. Such a geometry was inspired by previous studies that, based on the BTH theory, aimed to develop and optimize a surface micro-pattern enabling a macro-hydrodynamic friction regime during lubricated sliding contact. According to the theoretical predictions, this regime is entirely due to the collective flow action of the micro-structural defects, and it could not be established in the case of a flat untextured surface. The specific micro-grooved dimples depth, orientation and spatial distribution enable, indeed, better retaining the lubricant under the pad and/or redirecting part of it towards the internal pad portion through oppositely developed

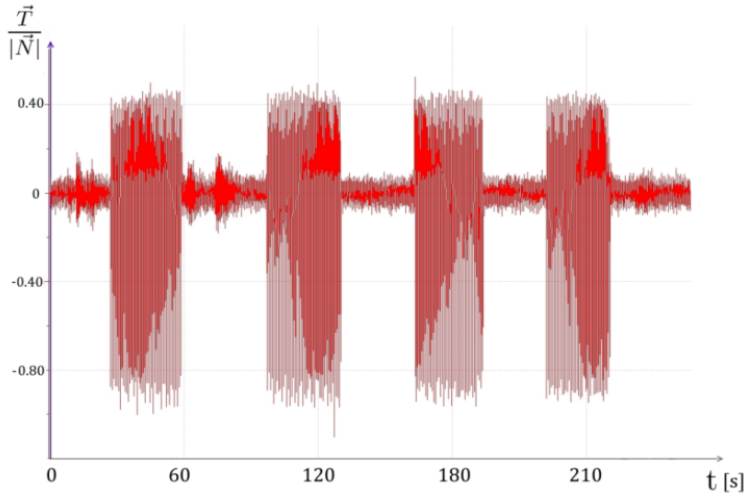

FIGURE 5.9: Friction coefficient behavior calculated as the tangential force T to the normal force N ratio, measured in the case of the textured sample. The tribometer operates in the reciprocating mode with isothermal conditions of the oil bath ($24 \pm 2\,\mathrm{deg}\,C$), linear translation speed of 136 mm/s reversed with a frequency of 1 Hz, and a normal load of 0.25 N

suction fingers. This collective micro-fluid-dynamic action of the dimples was expected to increase significantly the pad load support capabilities.

Following the theoretical non-uniform surface texture design, two different pads were fabricated which differed in the shape of the micro-dimples and the ablation strategy implemented to produce each dimple. In one sample, dimples of elliptical shape were fabricated with concentric laser beam elliptical paths, while in the second sample rectangular dimples were produced with a hatch of parallel ablation lines. The ablation depth of each dimple was finely controlled by adjusting the number of loops. However, the confocal microscope morphological characterization revealed an increase of the walls taper with the depth, as well as the appearance of some asperities at the bottom, especially in case of elliptical dimples.

The tribological behavior of each textured pad was investigated using a pin-on-disk tribometer. The rectangular dimple textured pad exhibited an overall lubricated friction coefficient which was approximately 20% lower than the elliptical dimple

counterpart. The improved tribological performance was ascribed to the better morphology of the rectangular dimples. A further tribological investigation of this last sample at varying loads revealed that, especially for loads below 1 N, the designed anisotropic texture pattern generates a hydrodynamic lubrication regime that is not expected for the conformal contact of two flat surfaces in the investigated range of sliding speeds. This is also confirmed by the absence of any wear sign on the pad surface after the tribological characterization. Finally, it was found that the friction coefficient of the textured pad was almost doubled when reversing the rotating direction of the tribometer disk in reciprocating mode. This results strengthens the hypothesis that the hydrodynamic regime is established only when the sliding direction the one for which the non-uniform texture pattern has been designed in order to produce a collective micro-fluid-dynamic action. On the contrary, the untextured control pad showed equivalent friction coefficient values irrespective of the sliding direction in reciprocating mode. The experimental results presented in this work are very promising and demonstrates that non-uniform surface texturing allows developing a new generation of so-called "super-bearings", with unique and enhanced tribological performances that, in addition, can be tailored according to the sliding direction.

5.2 Effects of the micro surface texturing in lubricated non-conformal point contacts

Topography of the surfaces plays important role in influencing the tribological properties of the materials and, in particular, the friction behavior of the two-rubbing surfaces during conformal and non-conformal contacts. The topic of the tribological performances of the micro-textured surfaces during non-conformal point contacts under lubricated conditions is only partially enlightened in literature. The largest part of theoretical and experimental analyses has been investigated on conformal contact conditions, where the contact area is much larger than the pocket size. In this study, what happens, in terms of friction, when the contact region has a width comparable with the hole diameter has been investigated. . Indeed, such conditions are significant in a variety of applications, involving conformal point contacts, such

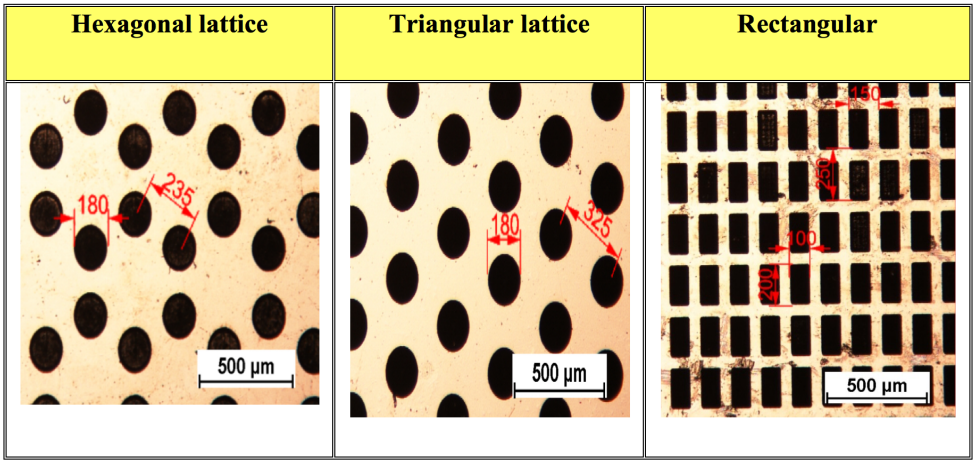

FIGURE 5.10: LST samples with different texture geometries (Triangular geometry: dimples with diameters d=183 μm, depth h6.7 μm, areal density A [%] =0.29; Hexagonal geometry: dimples d=183 μm, h6.6m, A [%] =0.27; Rectangular geometry: dimples: major axis L=200 μm, minor axis W=100 μm depth h7.3 μm, areal density A [%] =0.53, compared to the stainless steel polished surface.

as in ball bearings. Here, different tests are performed to study the tribological effects, which arise due to the contact length or contact pressure (stress) and the void coverage factor. These tests are performed by using a lubricant of two different viscosities from PAO (Poly-Alpha-Olefin).

5.2.0.1 Surface texture manufacturing by Femtosecond laser ablation process (fsLA)

The surface of the samples has been micro-textured with three different geometrical patterns as shown in fig. 5.10, where we report all quotes characterizing the three textures. Specifically, we have fabricated a Hexagonal and triangular pattern, both with circular dimples, and a rectangular one with rectangular dimples. The micro surface texturing has been performed upon stainless steel (1.4112) samples, having a surface roughness of 0.2 μm. Fabrication has been done by using a scanner interfaced ultrafast fiber CPA laser system (mod. Sci-series from Active Fiber Systems GmbH),and the resulting laser beam spot size on the sample surface $2w_o$ was about 25 μm. The laser has been operated at a repetition rate f of 50kHz, with an av-

Types of texture geometry	**Void Ratio** (%)	**Speed (mm/s)**	**Hatch**	**Track depth** (μm)
Hexagonal	27	22	Concentric	6.6
Triangular	29	34	Concentric	6.7
Rectangular	53	50	Crossed horizontal and vertical	7.3

TABLE 5.2: Process parameters defined for each texture geometry[circular dimples textured in hexagonal and triangular lattice, quasi rectangles textured in rectangular lattice]

erage power P between 60 and 70 mW. Therefore, the laser fluence, determined as $F = \frac{2E}{\pi w_o^2}$, where E is the pulse energy, was between 0.49 and 0.57 J/cm^2. For the three different textured geometries, different milling strategies have been used. For both the hexagonal and triangular texturing, the dimples have been generated by moving the laser beam along concentric circles, with a hatch distance of a few micrometers and a speed of 22 mm/s and 34 mm/s, respectively. For the rectangular geometry, crossed horizontal and vertical milling hatches have been performed at 50 mm/s. In these irradiation conditions, the number of pulses overlapping on the same focal area was determined as $N = \frac{2w_o f}{v}$ and resulted between 25 and 57. The threshold fluence ranged from 0.16 J/cm2 to 0.15 J/cm2. It was calculated starting with the single pulse threshold fluence (Fth(1) = 0.21 J/cm^2) and the incubation coefficient factor (S = 0.91) values found in the literature [102, 75] and using the Jee incubation model [103], in order to take into account the reduction of the ablation threshold due to the irradiation with multiple pulses. Therefore, laser ablation was performed nearly above the threshold fluence, in order to achieve a high level of accuracy and reproducibility of the machined microstructures. The desired dimple depth was achieved by finely adjusting the number of overlapped loops. The main process parameters are summarized in Table 5.2.

5.2.0.2 Characterization

The tribological properties of the micro-textured samples were evaluated by using different instruments. The rheometer MCR-301 was used as a tribometer to perform

the friction test under a normal force of 20N at 25deg C. Given the rheometer configuration, by means of the classic Hertzian relations, we can estimate the contact diameter as $D = 115.8\mu m$ has been estimated. We observe that; indeed, such a value is comparable with the characteristic dimensions of the dimples. With regards to the experiments, before carrying out the friction tests, the tribopairs have been ultrasonically cleaned using isopropanol, followed by rinsing with Petrolether and air dried. Experiments have been performed under pure sliding conditions by using a steel ball (100 Cr6, G-28) within the sliding range, which varies from 0.0001m/s to 1.4m/s. The samples with different geometrical patterns have been aligned parallel to the ball sliding direction. In detail, in the case of the rectangular dimples, we have aligned the longer axis with the sliding velocity of the ball. Whereas, in the case of the hexagonal and triangular geometrical patterns, given the circular dimples, the textures are perfectly isotropic and, thus, there is no preferential direction for the alignment.

A fixed quantity of lubricant, i.e. $1\mu l$ poly-alpha-olefin without additives (base oil: IsoflexTopas L32), whose properties are included in Table 5.3, was distributed on each plate at the point of the tribo-contact with μ-Pipette during each test and a new ball was used for each test. In each measurement cycle, three identically textured samples were placed in the sample holder and were tested. The measurement cycle can be divided into two different regimes. The first regime is the endurance part in which the rotational speed was kept constant at 20 rpm and the load was equal to 20 N. The second regime was the so-called Stribeck part in which the load F_N is kept constant at 20 N but the rotational speed is ramped up from 0 to 3000 rpm in a logarithmic way. This ramp-up was repeated three times within one Stribeck part. Both regimes occured twice. The first endurance part took 45 minutes and was carried out in order to avoid any transient effect, due to a running-in behavior, when recording the first set of Stribeck curves. Indeed, after this first Stribeck package, including three curve measurements, a second endurance part was run for another 60 minutes. In the end, the Stribeck part with three curve measurements was repeated. Therefore, for each measurement cycle we obtained six Stribeck curves which we averaged in the result plots.

Low Viscosity Lubricant (Type 1-Poly-alpha-olefin)	39.5 mm^2/s at 20^oC
High Viscosity Lubricant (Type 3-Poly-alpha-olefin)	1300 mm^2/s at 40^oC

TABLE 5.3: Viscometric Characteristics

Finally, the morphologies of the surfaces have been characterized. Contact pressure measurements have been performed with Fujifilm pressure measurement foils. The foils have been positioned in the contact area and glued to the tested samples. Pressure measurement tests have been carried out under a load equal to $F_N = 20N$, applied on the steel ball, without lubricant in a static condition for 10 minutes. After each test, the area of the contact pressure has been examined by using Leica DM4000 Microscope and Fujifilm Pressure Distribution Mapping system (FPD-8010E).

5.2.0.3 Results and Discussion

Preliminary pressure measurement tests have been conducted to visualize the differences, in terms of stress distribution, between the textured and the un-textured samples. Indeed, the contact pressure plays a crucial role in determining the wear ratio and, consequently, the friction [104, 105, 106].

In detail, foils have been tested with both textured and un-textured samples under the same conditions and, later, analyzed by using Leica DM4000 microscope. Depending on the level of the red colour (see insets of fig. 5.11), and by employing the Fujifilm Pressure Distribution Mapping system (FPD-8010E), it is possible to obtain in each point an estimation of the pressure value. Being the technique based on the qualitative evaluation of the images of the measurement foil, the pressure results plotted in fig. 5.11 have to be considered indicative, but, at the same time, they provide significant information on how the surface topography influences the pressure distribution. The dark red spots noticed in the insets of fig. 5.11 indicate the area effected by a high applied pressure (stress), whereas the light red spots represent the contact zone under an area of low pressure or stress. Incidentally, we notice that these values are consistent with the dimensions previously calculated

from the Hertzian theory.

More in detail, in fig. 5.11, the contact pressure distributions in two cases is shown: the first one refers to the un-textured samples, whereas the second one is obtained testing the rectangular textured pattern. In spite of the rough estimations offered by the pressure sensitive foils,it can be observed quite clearly that the micro-texture produces a significant increase of the pressure distribution. This is due to the presence of the micro-holes edges which, ultimately, act as stress intensity factors [103, 107]. Such an effect seems crucial in non-conformal contacts where the contact area is comparable with the pocket size. Indeed, in fig. 5.12, confocal images for the rectangular geometry (on the top) and for the hexagonal pattern (on the bottom) show that the worn zone has the same size of the rectangular micro-hole or pocket.

The higher pressure due to the presence of the micro-texture is a potential evidence of larger wear. This is particularly critical in all the regimes where we do not have a fully developed lubrication film and where, as a consequence, the wear ratio tends to be higher. Larger wear indicates larger friction, and, therefore, the presence of a micro-pattern seems to be detrimental in conformal contacts [106]. However, the presence of micro-holes may play also a positive role. Indeed, in the mixed and boundary regimes, where the wear is larger, the holes constitute an opportunity to entrap the debris and, therefore, contribute to a smoother interface between the contacting bodies [105]. This may entail the reduction of the interfacial friction. Ultimately, in the presence of micro-textured surfaces in point non-conformal contacts, two competitive mechanisms can be expected: on one side, the presence of the holes edges produce an intensification of the stress distribution and, therefore, an increase of the wear ratio; on the other hand, the holes can capture the debris related to the wear process and, therefore, can help in obtaining a smoother interface and, ultimately, a smaller friction force.

All this is confirmed in fig. 5.13, where we plot the friction coefficient, μ, as a function of the sliding velocity, u. Each micro-texture geometry has been tested under the same conditions by using two different lubricants (shown in Table. 5.3). In both cases, we focus on the mixed and boundary regimes, where it is well known that the wear plays a fundamental role and, consequently, it is more interesting to investigate

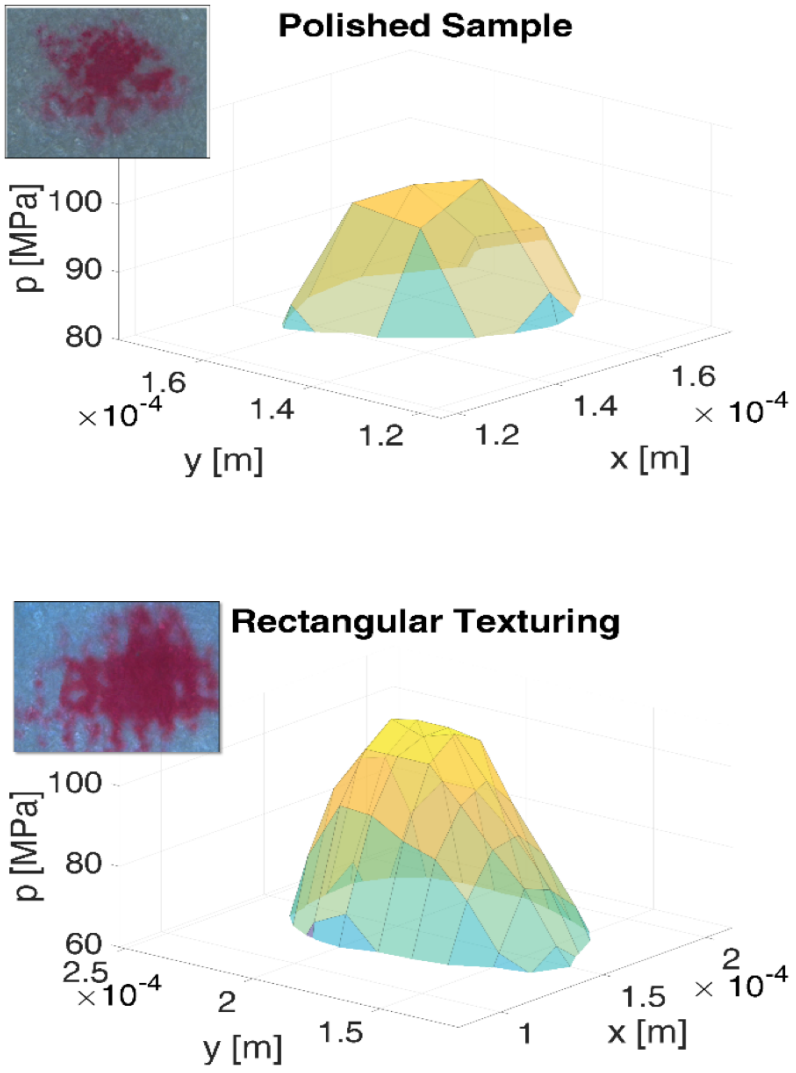

FIGURE 5.11: Contact pressure distribution maps (FPD-8010E) based on the analysis of the acquired microscope images of the Fujifilm measurement foils shown in the insets

the effects of a textured pattern. In fig. 5.13(a) and fig. 5.13(b), we observe that, in comparison with the results of the untextured samples, the hexagonal and the triangular patterns produce a deterioration of the frictional performances, whereas the rectangular pattern shows an improvement in the order of 20%. Interestingly, these two opposite trends look stronger at low speed, where the wear is expected to be larger. The different behavior can be explained by assuming that the two aforementioned mechanisms, both related to the wear, intervene differently in the two cases. Indeed, for the triangular and the hexagonal lattices, the wear increase, related to the change in the topography, prevails and determines an increase of

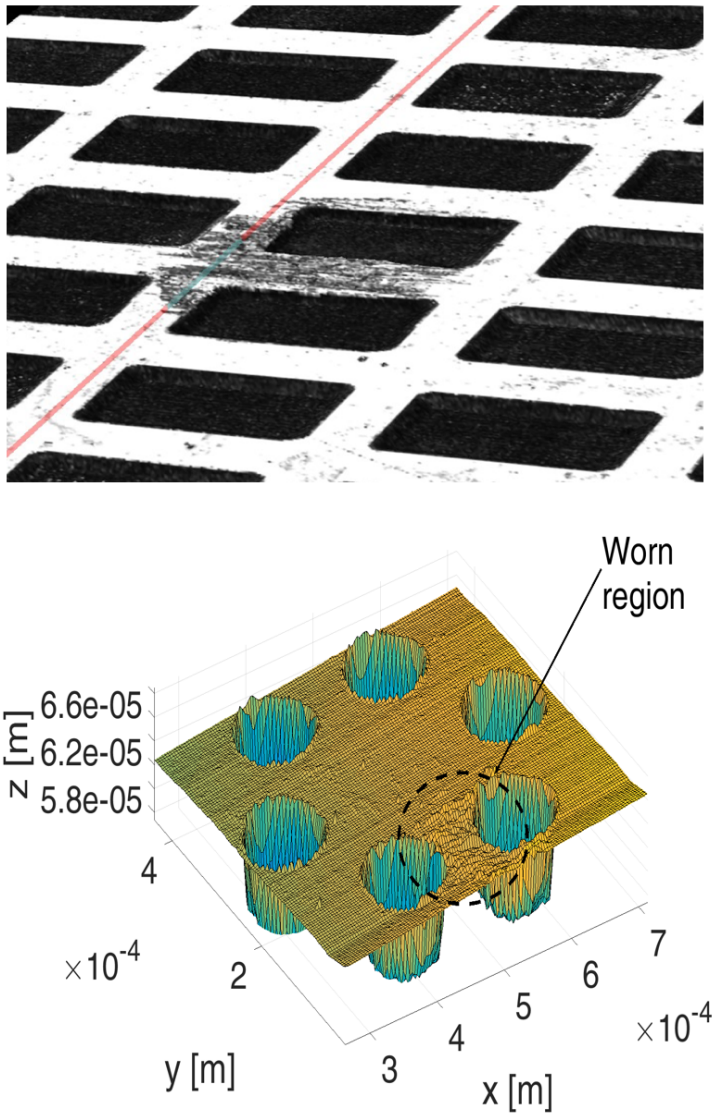

FIGURE 5.12: Industrial Laser Confocal Microscope 3D Images (50X) for the rectangular geometry texture (on the top) and CSM Confocal Microscope Images for the hexagonal texturing (on the bottom). In both cases, the worn zone is clear

the friction force. Conversely, in the case of the rectangular micro-holes, the debris entrapment effect seems to dominate and determines, in the mixed and the boundary lubrication regimes, a reduction of the frictional losses. As the first process, i.e. the stress intensification and, consequently, the larger wear, cannot depend significantly on the dimple geometry since it is mainly related to the presence of sharp edges in the contact region, the very different experimental outcomes have to be related to the second mechanism, i.e. the debris entrapment, which is strictly dependent on its turn on the void ratio. Indeed, a larger fraction of dimples on the total sample

surface can guarantee more space, for the wear particles, to be captured in the micro-holes. This is what occurs in our case where the rectangular pattern, with a void ratio of 53%, performs much better than the other two cases.

5.2.0.4 Conclusions

The non-conformal point contacts of laser textured and untextured surfaces have been experimentally investigated. It has been shown that introducing a surface texture may have opposed outcomes. Indeed, in comparison with un-textured samples, it can bring to a deterioration of the frictional performances, but, on the other hand, can also determine a significant reduction of the frictional losses. This has been related to the occurrence of two different competing mechanisms: one deals with the stress intensification provoked by the holes edges, which contribute to intensify the stress, thus increasing the wear ratio and, therefore, the friction losses. The other element is related to the debris particles entrapment, to the creation of a smoother interface and, consequently, to a reduced friction. Depending on the mechanism which prevails, the texture introduction can worsen or improve the tribological performances. The experimental tests show that a high void ratio can be useful to enhance the entrapping effect and decrease the friction. Ultimately, these results indicate the necessity to pay more attention to the micro-texture in conformal contacts as a tool to optimize friction.

5.3 Experimental investigation of the tribological and wettability properties of laser-textured martensitic steel surfaces

The objective of the following experimental investigation was to define a novel approach to find the most appropriate lubricant for a mechanical equipment by studying the friction behavior during the reciprocating sliding contact under dry and lubricated conditions. Micro-texturing was performed on martensitic steel surfaces by using a 1030-nm-wavelength femtosecond laser system. Surfaces were micro-textured with three different geometrical patterns with same parameters as shown

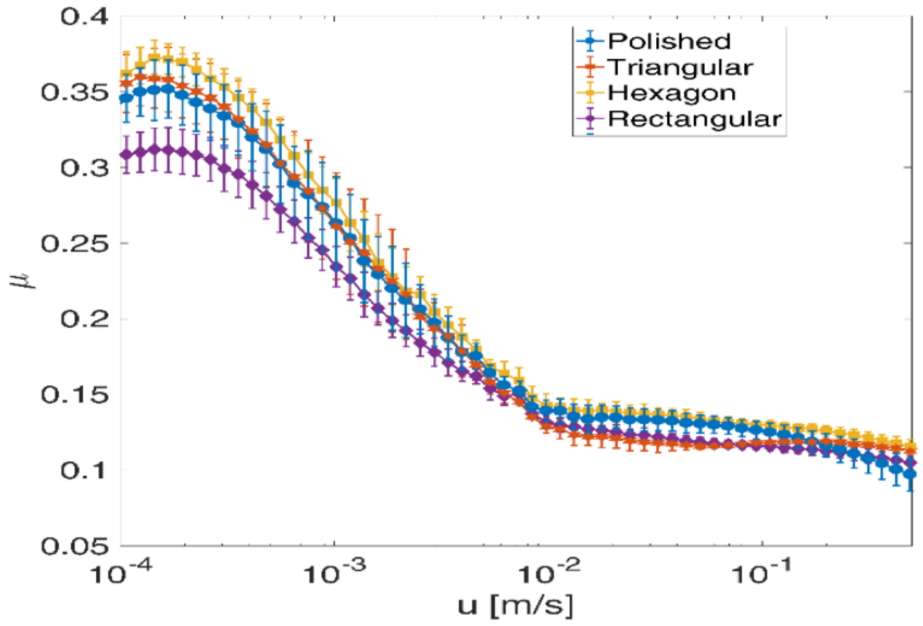

Figure: 5.13 (a)

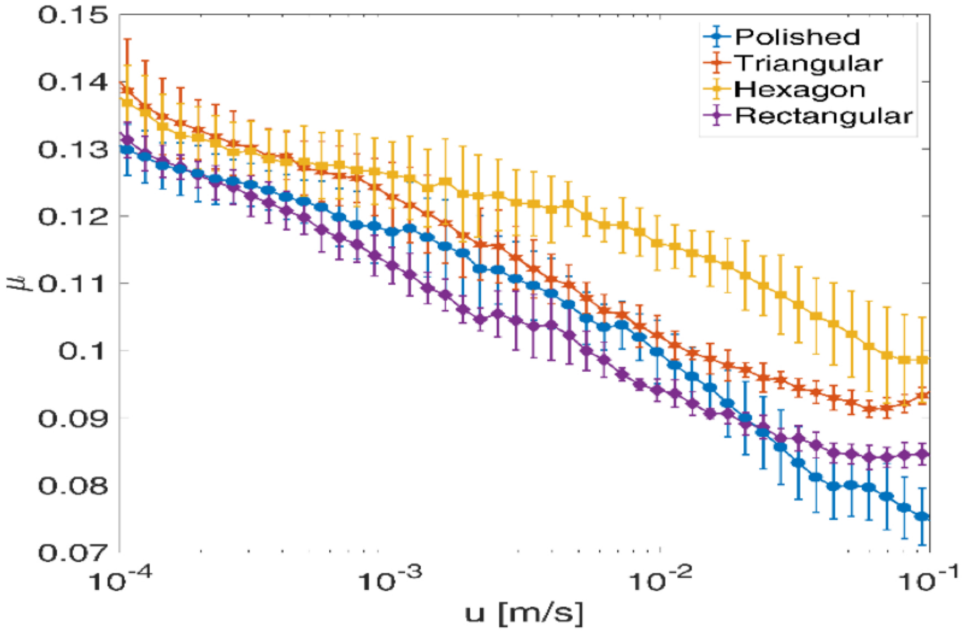

Figure: 5.13 (b)

FIGURE 5.13: Friction coefficient, μ, vs. sliding velocity, u. Figure 5.13(a) and 5.13(b) refer respectively to the low viscosity (Type 1) and the high viscosity lubricant (Type 3). For each measure, we report the scatter as an errorbar.

in fig. 5.10. The fabrication was also performed in the similar procedure as explained in section 5.2.2, and the same texture geometry(rectangular, hexagonal and triangular) used of the previous section.

5.3.1 Characterization

The tribological properties of the micro-textured samples were evaluated by using different apparatus. A Phoenix TE79 tribometer (fig. 5.14) was used to determine the coefficient of friction of the textures under various conditions. A reciprocating ball-on-disk sliding approach was used with total cycle count of 300 and stroke distance of 5 mm, giving a total sliding distance of 1.5 m. Samples were ultrasonically cleaned in Teepol and acetone, each for 5 minutes. An 8mm diameter alumina counterpart ball was used for all tests, with a new clean spot being used for each test. A load of 200 gf (2 N) was used with an approximate Hertzian contact pressure of 750 MPa. The conditions tested were varying sliding speeds (5, 10, 50, 100, 500 & 1000 mm/s), temperatures (20deg C) and lubricants (dry, glycerol, 15W40 mineral oil). Stribeck curves have been produced by comparing the average coefficient of friction and calculating the Hersey number for each sample type. Hersey numbers H were calculated following the formula $H = \frac{u\eta}{F}$, where u is the speed in mm/s, η the viscosity in mPa.s and F the load in mN.

5.3.1.1 Contact Angle Measurement

An Alicona G5 focus variation microscope (FVM) was used to evaluate the textured surfaces, in term of ablated pocket dimensions and surface roughness. A video-based optical contact angle measuring device, Attension Theta Optical Tensiometer, was used to assess the wettability properties of the surfaces. Using the sessile drop technique, the static contact angle (CA) was measured by dispensing droplets of 6 μl under atmospheric conditions and after stabilization. In addition different lubricants-glycerol, mineral oil, Milli-Q water with different visocisites (shown in Table 5.4), was used to compare the wettability values to hydrophobicity or hydrophilicity. A hot stage was used in order to heat both the sample and the dispensed liquid to 80 deg C. All measurements were repeated 3 times for statistical purposes.

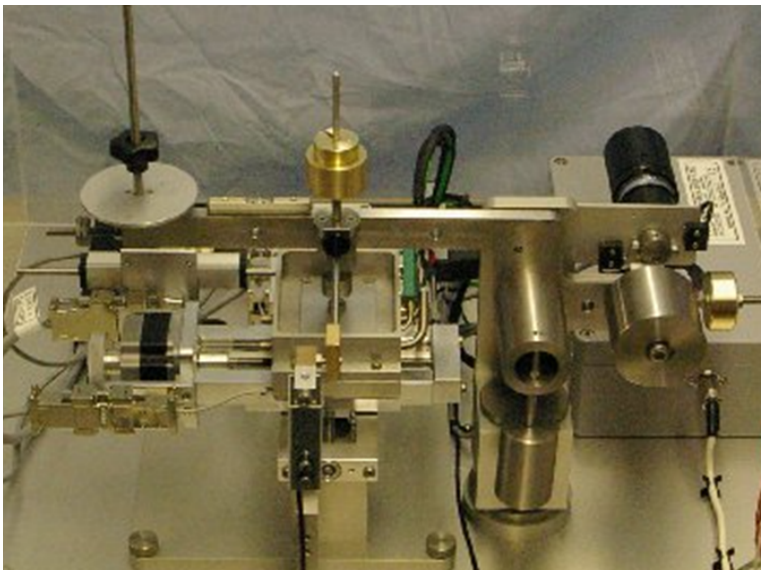

FIGURE 5.14: Image of Phoenix TE79 tribometer

	Dynamic viscosity (mPa·s)	
Dry/ Air	Glycol	Mineral Oil
0.01983	1413.8	287.23

TABLE 5.4: Viscometric characteristics for the considered fluids.

Spreading curves were obtained by analyzing droplet images recorded each 10 frames per second, starting from the first contact of the droplet onto the surface and for a duration of 70 seconds. Spreading values were estimated by measuring the diametral contact distance of the drop to the surface and projected to calculate the area of a disk.

5.3.2 Results and discussion

Friction measurement tests have been conducted to visualize the differences, in terms of the Stribeck curve for un-textured stainless steel surfaces, under dry and lubricated conditions. Indeed, the trend of the Stribeck curve plays a crucial role in choosing a lubricant and sliding velocity for having a highest friction reduction on textured surfaces. In fig. 5.15, lubricated un-textured polished surfaces give lesser friction, as compared to the dry. During dry condition, the coefficient of friction decreases with an increase of the sliding velocity or Hersey number, but, still, it

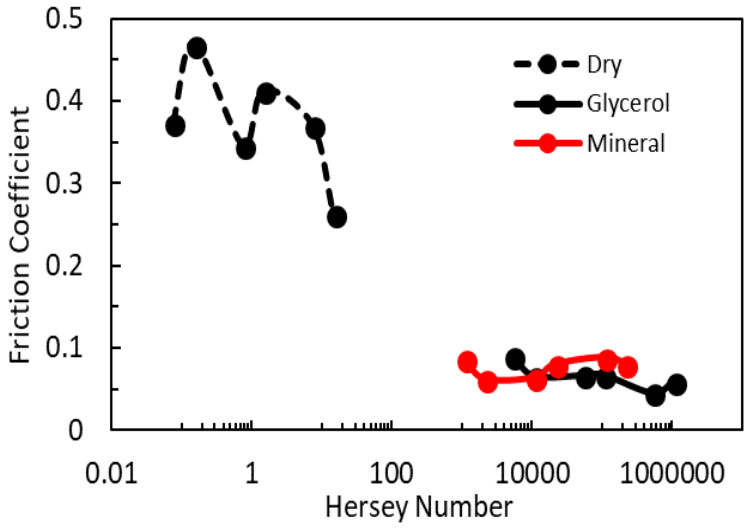

FIGURE 5.15: Friction coefficient vs Hersey number under dry and lubricated conditions on lubricated un-textured polished steel

has much higher friction coefficient in comparison with the lubricated conditions. During dry conditions, it shows a really high momentum with an increase of sliding velocity, which causes more initial wear as compared to lubricated condition. Among glycerol and mineral oil, mineral oil is low viscosity lubricant (shown in Table 5.4), and gives a consistent friction reduction throughout, with an increase of the sliding speed, which leads to increase of the Hersey number. Whereas, having the glycerol a very high viscosity, it shows a friction reduction as compared to mineral oil with an increase of the Hersey number.

In the nutshell, we can say that the lubricated un-textured surfaces give better results as compared to dry un-textured surfaces. Mineral oil doesn't have a huge variation in the coefficient of friciton with an increase of the sliding velocity, and glycerol has more right shift (due to viscous effects) and less friction of the Stribeck curve. Based on these results it has been possible to choose the sliding velocity where the 5mm long wear track can be easily re-lubricated. This helps to initiate the process of defining a best suitable parameter (e.g. sliding velocity & type of lubricant) for achieving the higher friction reduction on the textured surfaces. Finally, the friction measurement tests have been conducted in terms of the Stribeck curve for different textured and un-textured surfaces with chosen mineral oil as a lubricant under reciprocating sliding contact. In fig. 5.16 textured surfaces have lower COF as

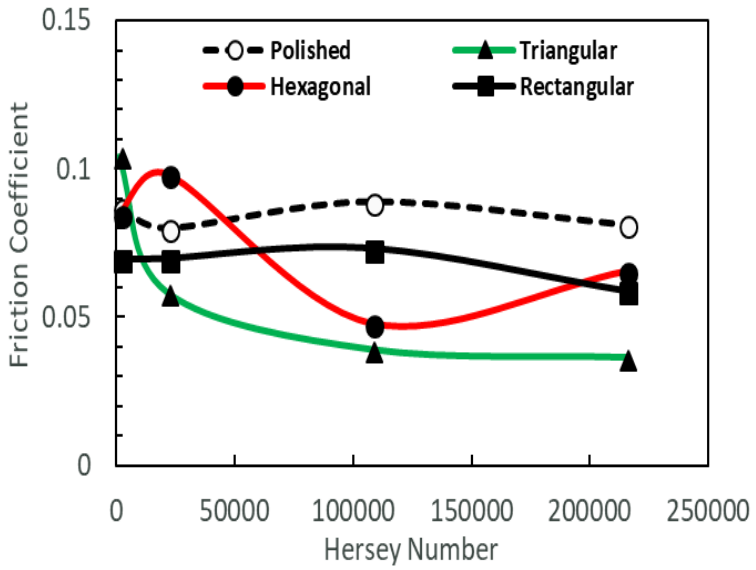

FIGURE 5.16: Friction coefficient vs Hersey number for un-textured and different textured surfaces, using mineral oil as a lubricant

compared to the un-textured from boundary to mixed regime. Triangular textured surfaces show the highest friction reduction as compared to other textured surfaces from boundary to mixed regime with an increase of Hersey number, but they also have a highest friction coefficient at low sliding velocity of 5mm/s or boundary conditions.

Rectangular texture shows a lowest COF at a low sliding velocity of 5mm/s, but with an increase of the sliding velocity or Hersey number, it shows consistent results from boundary to mixed regime. It also stays with a lower COF as compared to the un-textured surface from boundary to mixed regime. The friction coefficient almost remains consistent with an increase of sliding velocity. Hexagonal textured surfaces show the increase of friction in the beginning. This could be due to distortion form edges or debris, which lead to increase of friction while sliding. But later, this texture geometry shows a friction reduction from boundary to mixed regime with increase of the Hersey number towards the elasto hydrodynamic regime.

Also, the contact angle measurement tests have been conducted to understand the wettability properties of the textured and un-textured surfaces (fig. 5.17). It has been conducted with three different lubricants, which include water, Glycerol, Mineral oil. In case of using water as a lubricant, polished un-textured samples show

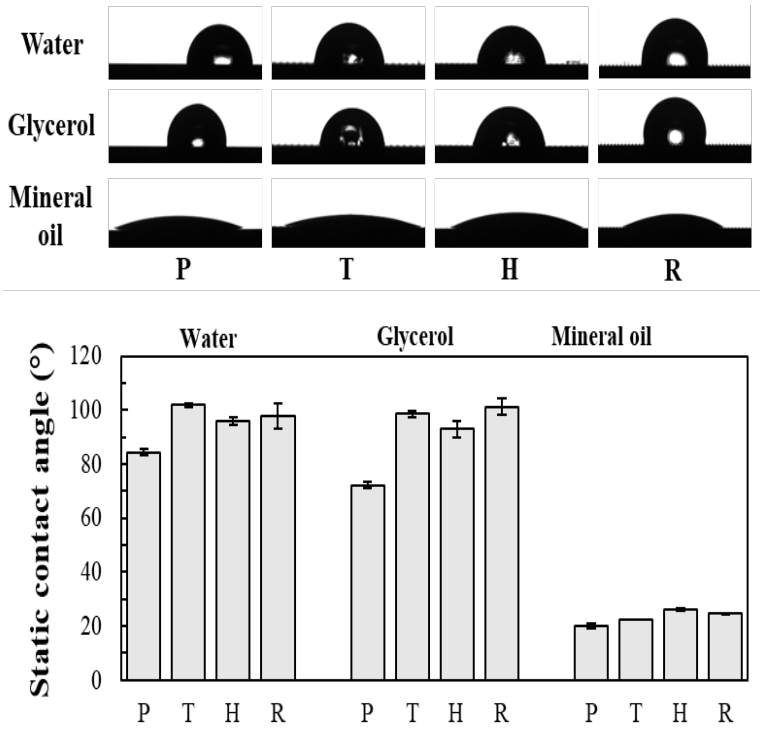

FIGURE 5.17: Image and measurement of static contact angles of the polished (P), triangular (T), hexagonal (H), and rectangular (R) textured surfaces, using comparatively water, glycerol and mineral oil as probe liquid

the contact angle (CA=84^o), whereas textured samples with different geometrical patterns show the contact angle at the hydrophilic-hydrophobic barrier (CA=90^o). In case of Glycerol as a lubricant, polished un-textured sample is more "glycerol"-philic with a contact angle (CA(PG)) =72^o, and the textured samples reach the glycerol-phobicity with a contact angle lies between 92^o and 105^o, CA(TG)=99^o, CA(HG)=93^o and CA(RG)=101^o. Mineral oil exhibits a philic behavior with CA around 25^o for the textured and un-textured surfaces. This result also supports the tribology, which shows the less friction coefficient in case of mineral oil with textured and un-textured surfaces.

The three considered textures show a slight improvement of Contact Angle for three liquids, however difference between textures is not really relevant regarding the contact angles. This is probably due to the size of the textures, that are too big to trap air inside. There is a small difference between the textured surfaces and the polished one, which is only produced by a combined effect of change in surface

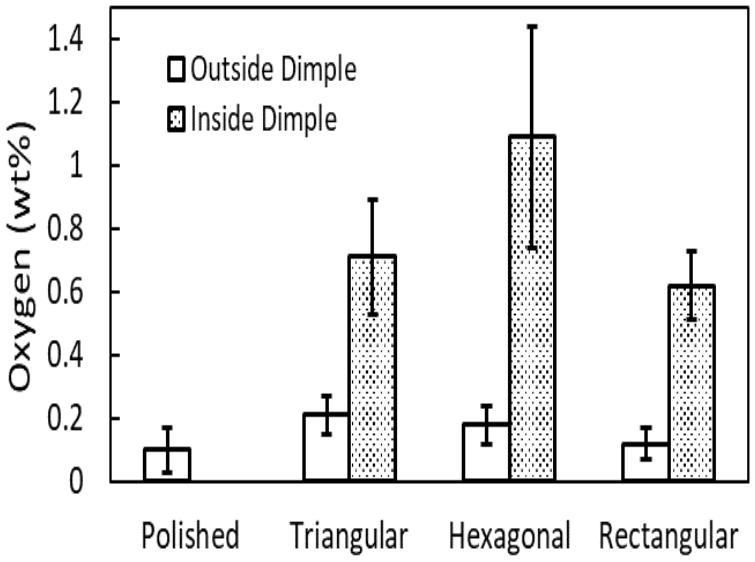

FIGURE 5.18: Oxygen content measured by EDS (wt%) on untextured surfaces and inside/outside the different laser-textured dimples

chemistry and increase in surface roughness. In fig. 5.18, EDS analysis provides elemental composition. We can see that, among the textured surfaces, the surfaces with a higher void ratio has a least oxygen content inside the dimples as compared to the textured surfaces with a lesser void ratio. So, that could be the reason why the rectangular textured surfaces (VR=52%) show lesser amount of oxygen content inside the dimples as compared to triangular (VR=29%) and hexagonal textured surfaces (VR=27%). We can clearly see the trend of increasing oxygen content with decreasing void ratio. Also, the "Void ratio" plays a vital role in effecting the slight change of CA.

The behavior of the lubricant while spreading on the textured surfaces was shown in fig. 5.19. The spreading is better with mineral oil as compared with the glycerol. However, the wettability of mineral oil is decreasing with the increase of the time. Spreading curves are measured until reaching a plateau, meaning stabilization. For mineral oil, the first contact angle measured is around 60 deg decreasing progressively to the 25^o, almost wetting. For glycerol, the first contact angle is measured around 120^o, decreasing progressively to 85^o. Observed spreading of the lubricant reflects the influence of both, the viscosity of the lubricant and wetting properties

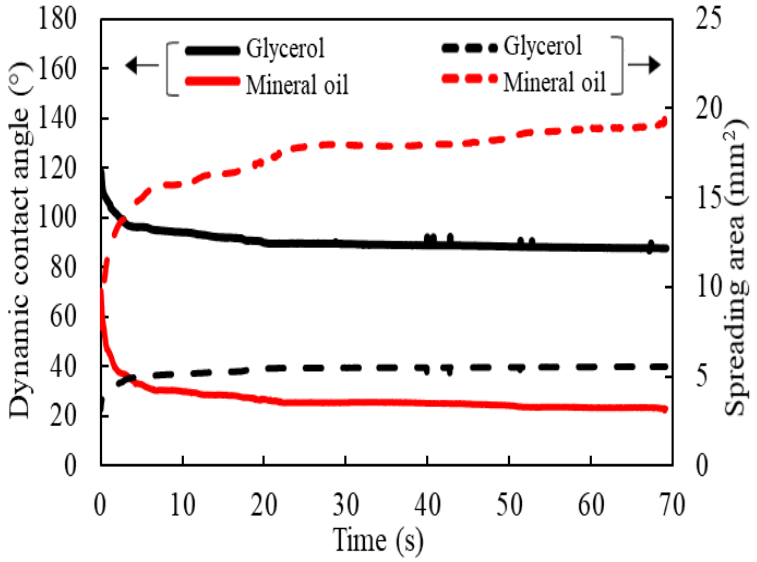

FIGURE 5.19: Spreading of lubricants on rectangular textured surface ($6\mu l$, $20\text{deg}\,C$) with respect to the contact angle and area

of the surface. Mineral oil exhibited a more constant philic behavior and an almost complete spreading over the polished and textured surfaces. It explains why the mineral oil gives the consistency in the friction reduction. It also explains, why choosing mineral oil is good for the mechanical equipment's because mineral oil wets the surface, regardless the working conditions and surface finishing, and its philic behavior will help to maintain the lowest coefficient of friction.
At high temperature, the spreading is even better for oil. At $80\text{deg}\,C$, the oil spreads better and faster through the surface, and thus the results for friction are better (fig. 5.19).

5.4 Conclusions

The study of the micro-textured effects on the tribological and wettability properties of laser-textured martensitic steel surfaces found that introducing surface texturing in different geometrical patterns leads to friction reduction under different lubrication regimes of the Stribeck curve. Indeed, in comparison with un-textured samples, the textured samples show lesser friction and a slight reduction of the contact angle with different lubricants. Mineral oil shows more consistency in the friction reduction due to the philic behavior of the mineral oil or the complete spreading of the

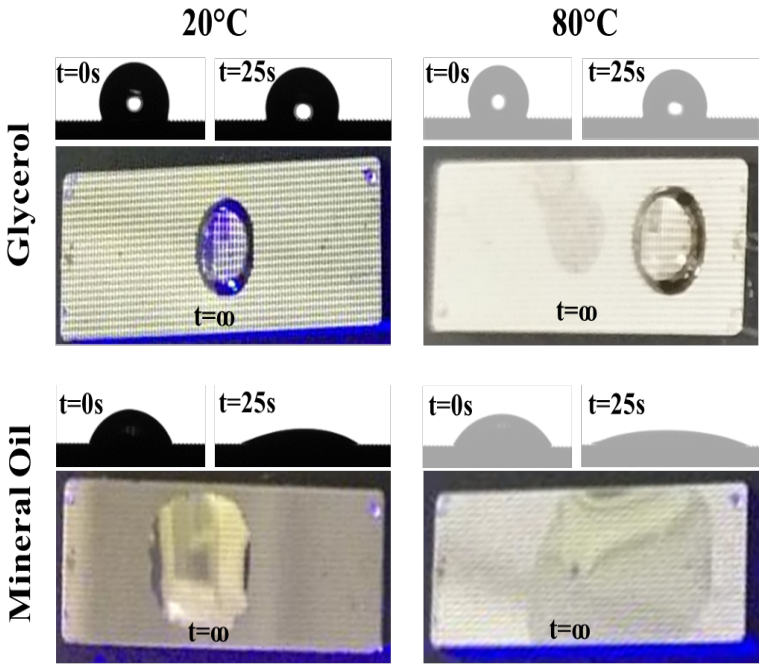

FIGURE 5.20: Evolution of spreading of lubricants (glycerol and mineral oil) on rectangular textured surface with the increase of temperature

lubricant on textured and un-textured samples. The experimental tests show that a mineral oil can be useful to decrease the friction for low and high dynamic velocities. Ultimately, these results present a novel and practical approach for the design of the tribological systems geometry of the surface texturing, lubricant, working temperature and sliding velocity.

Chapter 6

Conclusion

In the present work, I have investigated the influence of the micro-textured geometrical patterns on tribological properties during conformal and non-conformal contact in dry as well as lubricated conditions. In brief, the purpose of present thesis is to reveal the laser textured geometrical patterns, which help to enhance the tribological properties, for e.g. friction reduction.

Different experimental techniques and micro-textured geometrical patterns were used to reveal it. Results suggest that the joint action of virtual prototyping (BTH lubrication theory) and ultrafast laser micro-prototyping can lead to unconventional and impressive results in terms of enhanced or tailored contact mechanical properties of the generic lubricated tribopair. It demonstrates that non-uniform surface texturing allows developing a new generation of so-called "super-bearings", with unique and enhanced tribological performances that, in addition, can be tailored according to the sliding direction.

Results from the study of non-conformal point contacts provides simultaneous occurrence of two competing effects, when the contact area has size similar to the width of textured surfaces. One was related to the stress intensification, due to the presence of the micro-hole edges on the contact topography, which leads to a consequent increase in wear and friction. On the other hand, micro-texture may play a

positive role in the friction optimization given the possibility, offered by the micro-holes, to entrap wear debris and, then, to preserve a smoother interface between the contacting pairs. These results point out the necessity to pay more attention to the micro-texture in conformal contacts as a tool to optimize friction. These results also work as benchmark for further investigation in this regime, which has been poorly investigated in the literature.

Studying the tribological and wettability properties of laser-textured martensitic steel surfaces during reciprocating sliding contact provides the result, which suggest that laser textured surfaces have friction reduction in different lubrication regime as compared to un-textured surfaces and also slight reduction of the contact angle with different lubricants. It allows to define a novel approach for the design of tribological systems depending on surface texturing, lubricant, working temperature and sliding velocity.

In conclusion, this work shows that depending on the microgeometry of the surface texture, the coefficient of friction under lubrication regime can be accurately controlled. However, there are several mechanisms behind these results, like e.g. wettability, chemistry of surfaces and lubricants, fluid dynamics and cavitation at the micro-scale, that deserve further investigation to be fully controlled. This would lead to fabricate tribological surfaces with optimized geometrical patterns, enhancing the lifetime and reducing friction in different mechanical equipment's. It will help the scientific community to develop the mechanical system that are beneficial for the establishment of the green environment.

Bibliography

[1] Simon C Tung and Michael L McMillan. Automotive tribology overview of current advances and challenges for the future. *Tribology International*, 37 (7):517 – 536, 2004. ISSN 0301-679X. doi: https://doi.org/10.1016/j.triboint.2004.01.013. The New Trends and Frontiers in Tribology.

[2] I Etsion. Improving tribological performance of mechanical components by laser surface texturing. *Tribology Letters*, 17(4), 2004.

[3] Yuri Kligerman and Izhak Etsion. Analysis of the hydrodynamic effects in a surface textured circumferential gas seal. *Tribology Transactions*, 44(3):472–478, 2001. doi: 10.1080/10402000108982483.

[4] B. Jaeggi, B. Neuenschwander, M. Schmid, M. Muralt, J. Zuercher, and U. Hunziker. Influence of the pulse duration in the ps-regime on the ablation efficiency of metals. *Physics Procedia*, 12:164 – 171, 2011. ISSN 1875-3892. doi: https://doi.org/10.1016/j.phpro.2011.03.118. Lasers in Manufacturing 2011 - Proceedings of the Sixth International WLT Conference on Lasers in Manufacturing.

[5] I. M. Hutchings. *Tribology: Friction and Wear of Engineering Materials*. Edward Arnold, London, 1992.

[6] Bharat Bhushan. *Modern Tribology Handbook*. CRC Press, 2001.

[7] D Dowson. *History of Tribology*. London ; Bury ST Edmunds(UK) : Professional Engineering Publishing, cop., 1998.

[8] B. N. J. Persson. *Sliding Friction Physical Principles and Applications*. Springer, 1999.

[9] Amontons GA. *Histoire de l'Académie royale des sciences, avec les mémoires de mathématique et de physique.* Académie royale des sciences, 1699.

[10] J Halling. *Principles of Tribology.* The Macmillan Press Ltd, London, 1975.

[11] Bhushan B. *Modern Tribology Handbook Vol 1.* CRC Press, 2002.

[12] Kenneth C Ludema. *Friction, Wear, Lubrication: A Textbook in Tribology.* CRC Press, 2010.

[13] Raymond G. Bayer. Mechanical wear prediction and prevention. Technical report, New York : M. Dekker, 1994.

[14] W.E. Campbell. Boundary lubrication- an appraisal of world literature. *AMERICAN SOCIETY OF MECHANICAL ENGINEERS*, pages 87–117, 1969.

[15] Seiichro Hironaka. Boundary lubrication and lubricants. Technical report, School of Engineering, Tokyo Institute of Technology, 1984.

[16] Technical handbook of stainless steels (www.atlasmetals.com.au), atlas speciality metals, melbourne, australia, 2003..

[17] B A BURGAN N R BADDOO. *Structural Design of Stainless Steel.* The Steel Construction Institute Silwood Park Ascot Berkshire SL5 7QN, 1997.

[18] *Lucefin.com.*

[19] Margaret M. Murnane Sterling Backus, Charles G. Durfee III and Henry C. Kapteyn. High power ultrafast lasers. *Review of Scientific Instruments*, 69: 1207–1223, 1998.

[20] Malvin Carl Teich Bahaa E. A. Saleh. *Fundamentals of photonics, 2nd edn., Chap3.* John Wiley&Son Inc., 2007.

[21] *Zeiss sigma SEM manual [www.zeiss.com] Scanning Electron Microscopes (SEM).*

[22] B Herman. *Fluorescence Microscopy*, chapter undamental optics of microscopy., pages 17–20. BIOS Scientific Publishers - Springer, Oxford, United Kingdom, 1998.

[23] Svelto Bradbury and B Bracegirdle. *Introduction to Light Microscopy: Microscopy Handbooks*, volume 42, chapter The objective, pages 69–76. BIOS Scientific Publishers - Springer, Oxford, United Kingdom, 1998.

[24] KRZYSZTOF NADOLNY WOJCIECH KAPLONEK. Advanced 3d laser microscopy for measurements and analysis of vitrified bonded abrasive tools. *Jorunal of Engineering Science and Technology*, 2012.

[25] M Scaraggi. Optimal textures for increasing the load support in a thrust bearing pad geometry. *Tribol. Lett.*, 53:127–143, 2014.

[26] J.A. Walowit Hamilton, D.B. and C.M. Allen. Theory of lubrication by microirregularities. *American Society of Mechanical Engineers – Transactions – Journal of Basic Engineering*, 88(1):p. 177–185, 1966.

[27] I. Etsion and L. Burstein. A model for mechanical seals with regular microsurface structure. *Tribology Transactions*, 39(3):677–683, 1996. doi: 10.1080/10402009608983582.

[28] I. Etsion, Y. Kligerman, and G. Halperin. Analytical and experimental investigation of laser-textured mechanical seal faces. *Tribology Transactions*, 42(3): 511–516, 1999. doi: 10.1080/10402009908982248.

[29] J.A. Walowit Anno, J.N. and C.M. Allen. Microasperity lubrication. *American Society of Mechanical Engineers (ASME).*, 1967.

[30] Eric Willis. Surface finish in relation to cylinder liners. *Wear*, 109(1):351 – 366, 1986. ISSN 0043-1648. doi: https://doi.org/10.1016/0043-1648(86)90278-4.

[31] Yu.G. Schneider. Formation of surfaces with uniform micropatterns on precision machine and instruments parts. *Precision Engineering*, 6(4):219 – 225, 1984. ISSN 0141-6359. doi: https://doi.org/10.1016/0141-6359(84)90007-2.

[32] H. Tian, N. Sara, and N.P. Suh. Boundary lubrication studies on undulated titanium surfaces. *Tribology Transactions*, 32(3):289–296, 1989. doi: 10.1080/10402008908981891. cited By 94.

[33] Xiaolei Wang, Koji Kato, Koshi Adachi, and Kohj Aizawa. Loads carrying capacity map for the surface texture design of sic thrust bearing sliding in

water. *Tribology International*, 36(3):189 – 197, 2003. ISSN 0301-679X. doi: https://doi.org/10.1016/S0301-679X(02)00145-7.

[34] Xiaolei Wang, Koshi Adachi, Katsunori Otsuka, and Koji Kato. Optimization of the surface texture for silicon carbide sliding in water. *Applied Surface Science*, 253(3):1282 – 1286, 2006. ISSN 0169-4332. doi: https://doi.org/10.1016/j.apsusc.2006.01.076.

[35] Xiaolei Wang, Koji Kato, and Koshi Adachi. The lubrication effect of micropits on parallel sliding faces of sic in water. *Tribology Transactions*, 45(3): 294–301, 2002. doi: 10.1080/10402000208982552.

[36] Ulrika Pettersson and Staffan Jacobson. Influence of surface texture on boundary lubricated sliding contacts. *Tribology International*, 36(11):857 – 864, 2003. ISSN 0301-679X. doi: https://doi.org/10.1016/S0301-679X(03)00104-X. NORDTRIB symposium on Tribology 2002.

[37] Manabu Wakuda, Yukihiko Yamauchi, Shuzo Kanzaki, and Yoshiteru Yasuda. Effect of surface texturing on friction reduction between ceramic and steel materials under lubricated sliding contact. *Wear*, 254(3):356 – 363, 2003. ISSN 0043-1648. doi: https://doi.org/10.1016/S0043-1648(03)00004-8.

[38] Ehmann K Wang Q Lin C Greco A, Raphaelson S. Surface texturing of tribological interfaces using the vibromechanical texturing method. *ASME. J. Manuf. Sci. Eng*, 131((6)):061005–061005–8, 2009.

[39] I. Etsion and O. Michael. Enhancing sealing and dynamic performance with partially porous mechanical face seals. *Tribology Transactions*, 37(4):701–710, 1994. doi: 10.1080/10402009408983349.

[40] I. Etsion and G. Halperin. A laser surface textured hydrostatic mechanical seal. *Tribology Transactions*, 45(3):430–434, 2002. doi: 10.1080/10402000208982570.

[41] X.Q Yu, S He, and R.L Cai. Frictional characteristics of mechanical seals with a laser-textured seal face. *Journal of Materials Processing Technology*, 129(1):463 – 466, 2002. ISSN 0924-0136. doi: https://doi.org/10.1016/S0924-0136(02)00611-8. The 10th International Manufacturing Conference in China (IMCC 2002).

[42] Aviram Ronen, Izhak Etsion, and Yuri Kligerman. Friction-reducing surface-texturing in reciprocating automotive components. *Tribology Transactions*, 44 (3):359–366, 2001. doi: 10.1080/10402000108982468.

[43] G. RYK, Y. KLIGERMAN, I. ETSION, and A. SHINKARENKO. Experimental investigation of partial laser surface texturing for piston-ring friction reduction. *Tribology Transactions*, 48(4):583–588, 2005. doi: 10.1080/05698190500313544.

[44] I. Etsion Kligerman, Y. and A. Shinkarenko. Improving tribological performance of piston rings by partial surface texturing. *Transactions of the ASME. Journal of Tribology*, 127(3):632–8., 2005.

[45] G. Ryk, Y. Kligerman, and I. Etsion. Experimental investigation of laser surface texturing for reciprocating automotive components. *Tribology Transactions*, 45(4):444–449, 2002. doi: 10.1080/10402000208982572.

[46] T.A. Nguyen P. Baumgart, D.J. Krajnovich and A.G. Tam. A new laser texturing technique for high performance magnetic disk drives. *IEEE Transactions on Magentics*, 31(6):2946–2951, 1995.

[47] I Etsion. State of the art in laser surface texturing. *Journal of Tribology*, 127 (1):248–253, 2005.

[48] A. V. Bulgakova, N. M.; Bulgakov. Pulsed laser ablation of solids: transition from normal vaporization to phase explosion. *Applied Physics A Materials Science & Processing*, 73(2):199–208, 2001.

[49] S. Nolte F. von Alvensleben B. N. Chichkov, C. Momma and A. Tünnermann. Femtosecond, picosecond and nanosecond laser ablation of solids. *Applied Physics A*, 63(2):109–115, 1996.

[50] Carsten Momma, Boris N Chichkov, Stefan Nolte, Ferdinand von Alvensleben, Andreas Tünnermann, Herbert Welling, and Bernd Wellegehausen. Short-pulse laser ablation of solid targets. *Optics Communications*, 129(1):134 – 142, 1996. ISSN 0030-4018. doi: https://doi.org/10.1016/0030-4018(96)00250-7.

[51] R. Le Harzic, D. Breitling, M. Weikert, S. Sommer, C. Föhl, S. Valette, C. Donnet, E. Audouard, and F. Dausinger. Pulse width and energy influence on laser micromachining of metals in a range of 100fs to 5ps. *Applied Surface Science*, 249(1):322 – 331, 2005. ISSN 0169-4332. doi: https://doi.org/10.1016/j.apsusc.2004.12.027.

[52] S.V. Garnov S.M. Pimenov V.I. Konov V. Romano B. Borsos Kononenko, T.V. and H.P. Weber. Laser ablation and micropatterning of thin tin coatings. *Applied Physics A*, 71(6):627–31, 2000.

[53] M. Scaraggi, F.P. Mezzapesa, G. Carbone, A. Ancona, and L. Tricarico. Friction properties of lubricated laser-microtextured-surfaces: An experimental study from boundary- to hydrodynamic-lubrication. *Tribology Letters*, 49(1): 117–125, 2013. doi: 10.1007/s11249-012-0045-2. cited By 33.

[54] Michele Scaraggi, Francesco P. Mezzapesa, Giuseppe Carbone, Antonio Ancona, Donato Sorgente, and Pietro Mario Lugarà. Minimize friction of lubricated laser-microtextured-surfaces by tuning microholes depth. *Tribology International*, 75:123 – 127, 2014. ISSN 0301-679X. doi: https://doi.org/10.1016/j.triboint.2014.03.014.

[55] A. Ancona, G. Carbone, M. De Filippis, A. Volpe, and P.M. Lugarà. Femtosecond laser full and partial texturing of steel surfaces to reduce friction in lubricated contact. *Advanced Optical Technologies*, 3(5-6):539–547, 2014. doi: 10.1515/aot-2014-0045. cited By 2.

[56] W.M. Steen. *Laser Material Processing. Springer, London Limited, 2003.* Springer, 2003.

[57] *Spectra Physics: Laser Description Manual Quanta Ray Pro 290, 2006.*

[58] P. Lorazo, L.J. Lewis, and M. Meunier. Short-pulse laser ablation of solids: From phase explosion to fragmentation. *Physical Review Letters*, 91(22), 2003. doi: 10.1103/PhysRevLett.91.225502. cited By 200.

[59] R. Kelly and A. Miotello. Contribution of vaporization and boiling to thermal-spike sputtering by ions or laser pulses. *Physical Review E - Statistical Physics, Plasmas, Fluids, and Related Interdisciplinary Topics*, 60(3):2616–2625, 1999. doi: 10.1103/PhysRevE.60.2616. cited By 65.

[60] L.V. Zhigilei, Z. Lin, and D.S. Ivanov. Atomistic modeling of short pulse laser ablation of metals: Connections between melting, spallation, and phase explosion. *Journal of Physical Chemistry C*, 113(27):11892–11906, 2009. doi: 10.1021/jp902294m. cited By 215.

[61] D. Perez and L.J. Lewis. Molecular-dynamics study of ablation of solids under femtosecond laser pulses. *Physical Review B - Condensed Matter and Materials Physics*, 67(18), 2003. doi: 10.1103/PhysRevB.67.184102. cited By 235.

[62] X. Xu. Phase explosion and its time lag in nanosecond laser ablation. *Applied Surface Science*, 197-198:61–66, 2002. doi: 10.1016/S0169-4332(02)00304-5. cited By 62.

[63] Orazio Svelto. *Principles of lasers (4th edition)*. Springer, 1998.

[64] A. Miotello and R. Kelly. Critical assessment of thermal models for laser sputtering at high fluences. *Applied Physics Letters*, 67:3535, 1995. doi: 10.1063/1.114912. cited By 346.

[65] H Choudhary. Numerical simulation and experiments of nano pulsed uv laser on metal and polymer. Master's thesis, Indian Institute of Technology Kanpur, Kanpur, India, 2012.

[66] Johan Meijer. Laser beam machining (lbm), state of the art and new opportunities. *Journal of Materials Processing Technology*, 149(1):2 – 17, 2004. ISSN 0924-0136. doi: https://doi.org/10.1016/j.jmatprotec.2004.02.003. 14th Interntaional Symposium on Electromachining (ISEM XIV).

[67] J. Meijer, K. Du, A. Gillner, D. Hoffmann, V.S. Kovalenko, T. Masuzawa, A. Ostendorf, R. Poprawe, and W. Schulz. Laser machining by short and ultrashort pulses, state of the art and new opportunities in the age of the photons. *CIRP Annals*, 51(2):531 – 550, 2002. ISSN 0007-8506. doi: https://doi.org/10.1016/S0007-8506(07)61699-0.

[68] M Jensen. *Laser micromachining of polymers*. PhD thesis, Technical University of Denmark, 2004.

[69] R. Srinivasan, R. R. Hall, W. D. Loehle, W. D. Wilson, and D. C. Allbee. Chemical transformations of the polyimide kapton brought about by ultraviolet laser radiation. *Journal of Applied Physics*, 78(8):4881–4887, 1995. doi: 10.1063/1.359776.

[70] M. Hayden L. S. Stephens, R. Siripuram and B. McCartt. Deterministic micro asperities on bearings and seals using a modified liga process. *Transactions of the ASME. Journal of Engineering for Gas Turbines and Power*, 126(1): 147–154, 2004.

[71] J. Zhao, F. Sadeghi, and H.M. Nixon. A finite element analysis of surface pocket effects in hertzian line contact. *Journal of Tribology*, 122(1):47–54, 2000. doi: 10.1115/1.555328. cited By 21.

[72] K. Tønder. Hydrodynamic effects of tailored inlet roughnesses: Extended theory. *Tribology International*, 37(2):137–142, 2004. doi: 10.1016/S0301-679X(03)00043-4. cited By 54.

[73] K. Tønder. Inlet roughness tribodevices: Dynamic coefficients and leakage. *Tribology International*, 34(12):847–852, 2001. doi: 10.1016/S0301-679X(01)00084-6. cited By 69.

[74] M. Varenberg, G. Halperin, and I. Etsion. Different aspects of the role of wear debris in fretting wear. *Wear*, 252(11-12):902–910, 2002. doi: 10.1016/S0043-1648(02)00044-3. cited By 164.

[75] A. Kovalchenko, O. Ajayi, A. Erdemir, G. Fenske, and I. Etsion. The effect of laser surface texturing on transitions in lubrication regimes during unidirectional sliding contact. *Tribology International*, 38(3):219–225, 2005. doi: 10.1016/j.triboint.2004.08.004. cited By 350.

[76] Nam P. Suh, Mohsen Mosleh, and Phillip S. Howard. Control of friction. *Wear*, 175(1):151 – 158, 1994. ISSN 0043-1648. doi: https://doi.org/10.1016/0043-1648(94)90178-3.

[77] N. Sara, H. Tian, and N.P. Suh. Boundary lubrication of undulated metal surfaces at elevated temperatures. *Tribology Transactions*, 32(3):389–395, 1989. doi: 10.1080/10402008908981904. cited By 38.

[78] A. Mattews Holmberg, K. and H. Ronkainen. Coatings tribology – contact mechanisms and surface design. *Tribology International*, 31:107–120, 1998.

[79] Dowson D. *History of Tribology*. Longman, London, 1979.

[80] Desaguilers jt, a course of experimental philosophy. london (1744); .

[81] F. P Bowden and D. Tabor. *The Friction and Lubrication of Solids*. Clarendon Press, Oxford, Vol. I (1950) and Vol. II (1964).

[82] J. B. P. Williamson J. A. Greenwood. Contact of nominally flat surfaces. *Proc. R. Soc. London A*, (295-300), 1966.

[83] J. F. Archard. Contact and rubbing of flat surfaces. *Journal of Applied Physics*, page 981, 2004.

[84] J.F Archard. Elastic deformation and the laws of friction. *Proceedings of the Royal Society of London. Series A, Mathematical and Physical Sciences*, 243 (1233):190–205.

[85] Greenwood JA. The area of contact between rough surface and flats. *Trans. ASME J. Lubr. Tech*, 1(81), 1967.

[86] D. Tabor F. R. S. K. N. G. Fuller. The effect of surface roughness on the adhesion of elastic solids. *Proc. R. Soc. Lond. A*, pages 327–342;, 1975.

[87] B. N. J. Persson. The effect of surface roughness on the adhesion of elastic solids. *The Journal of Chemical Physics*, 115(5597), 2001.

[88] Hertz HJ. On contact between elastic bodies. *Reine Angew Math*, 92:156–171, 1881.

[89] W. Hirst J. F. Archard. The wear of metals under unlubricated conditions. *The Royal Society*, 236:397–410, 1956.

[90] Jorge Leiva Mohammed Jai Guy Bayada Roberto Ausas, Patrick Ragot and Gustavo C. Buscaglia. The impact of the cavitation model in the analysis of microtextured lubricated journal bearings. *Jounral of Tribology*, 129:868–875, 2007.

[91] M.M.Khonsari Y.Qiu. Experimental investigation of tribological performance of laser textured stainless steel rings. *Tribolgy International*, 11(5):635–644, 2011.

[92] Y. Qiu and M. M. Khonsari. On the prediction of cavitation in dimples using a mass-conservative algorithm. *Journal of Tribology*, 131(4), 2009.

[93] Yonggang Meng Jinyu Zhang. Direct observation of cavitation phenomenon and hydrodynamic lubrication analysis of textured surfaces. *Tribology letters*, 46(2):147–158, 2012.

[94] H. A. Spikes I. G. Pegg A. V. Olver, M. T. Fowell. 'inlet suction', a load support mechanism in non-convergent, pocketed, hydrodynamic bearings. *Proceedings of the Institution of Mechanical Engineers, Part J: Journal of Engineering Tribology*, 220(2):105–108, 2006.

[95] A. D. Gosman H. A. Spikes M. Fowell, A. V. Olver and I. Pegg. Entrainment and inlet suction: two mechanisms of hydrodynamic lubrication in textured bearings. *Journal of Tribology(ASME)*, 129(2):336–347, 2007.

[96] Stainless steel and corrosion (www.aperam.com), arcelormittal, paris, france, 2010.

[97] [en 10088] uni-en 10088, parts 1 to 5, acciai inossidabili (stainless steels), uni ente nazionale italiano di uni cazione (italian organisation for standardization), milan, 2005-2009.

[98] G. Kamlage A. Ostendorf C. Fallnich F. von Alvensleben H. Welling S. Nolte, C. Momma. Polarization effects in ultrashort-pulses laser drilling. *Appl. Phys. A*, 68:563–567, 1999.

[99] Savile Bradbury. *An Introduction to the Optical Microscope*, chapter The objective and the eyepiece, pages 49–57. Oxford Science Publications, Oxford, United Kingdom, 1989.

[100] M Spencer. *Fundamentals of Light Microscopy*, chapter Aberrations and microscope design, pages 63–69. Cambridge University Press, New York,, 1982.

[101] *Minsky, M. Memoir on inventing the confocal scanning microscope. Scanning 10, 128–139 (1988).*

[102] Walser RM Jee Y, Becker MF. Jee y, becker mf, walser rm. laser-induced damage on single-crystal metal sur- faces. j opt soc am b 1988;5(3):648. *J Opt Soc Am B*, 5(3):648, 1988.

[103] Johnson KL. *Contact mechanics.* Cambridge University Press, 1985.

[104] Pegg IG Reddyhoff T. Vladescu SC, Olver AV. Combined friction and wear reduc- tion in a reciprocating contact through laser surface texturing. *wear*, 358:51, 2016.

[105] Tufail K Gangopadhyay A Reddyhoff T. Vladescu SC, Ciniero A. Optimization of pocket geometry for friction reduction in piston–liner contacts. *Tribol Trans*, 1, 2017.

[106] Olver AV Pegg IG Reddyhoff T. Vladescu SC, Medina S. Lubricant film thickness and friction force measurements in a laser surface textured reciprocating line contact simulating the piston ring–liner pairing. *Tribol Int*, 98:317, 2016.

[107] Hills DA. Sackfield A, Dini D. Contact of a rotating wheel with a flat. *Int J Solid Struct*, 44:3304, 2007.

[108] Kato K. & Adachi K Wang, X. The critical condition for the transition from hl to ml in water-lubricated sic. *Tribology Letters,*, 16(4):253–8, 2004.

[109] Andreas Blatter Martin von Allmen. *Laser-beam interactions with solid materials: Physical principles and applications.* Springer, 1995.

[110] Martin H. Velocity dependence of kinetic friction in the prandtl-tomlinson model. *Phys. Rev. B*, 84(12):125419, 2011.

[111] Toporov YP Derjaguin BV, Muller VM. On the role of molecular forces in contact deformation. *Journal of Colloid and Interface Science*, 67:378, 1975.

[112] *Anton-paar [www. Anton-paar.com].*

[113] Coyne E O'Connor GM Glynn TJ. Mannion PT, Magee J. The effect of damage accumulation behaviour on ablation thresholds and damage morphology

in ultra- fast laser micro-machining of common metals in air. *Appl Surf Sci*, page 233:275, 2004.

[114] Erdemir A Fenske G Etsion I. Kovalchenkoa A, Ajayia O. The effect of laser surface texturing on transitions in lubrication regimes during unidirectional sliding contact. *Tribol Int*, 38(3):219, 2005.